Applications of Coupled Waveguides in Optical Integration and Nonlinear Frequency Conversion

Po Dong

Department of Electrical and Computer Engineering
McGill University
Montréal, Québec, Canada
August 2005

A thesis submitted to the Faculty of Graduate Studies and Research in partial fulfillment of the requirements of the degree of Doctor of Philosophy

Your file Votre référence
ISBN: 978-0-494-25130-0
Our file Notre référence
ISBN: 978-0-494-25130-0

ABSTRACT

Coupled waveguides, such as directional couplers and grating-assisted directional couplers, have many applications in integrated optics, optical communication and nonlinear optics. In this thesis, we investigate two important applications of them in optical integration and nonlinear frequency conversion. The work presented in this thesis is composed of two main parts. In the first part, we present a compact double-grating coupler between silicon-on-insulator (SOI) waveguides. This type of waveguide coupler has potential applications in multi-layer photonic integrated circuits. In the second part, we investigate nonlinear frequency conversion, such as second harmonic generation, in directional couplers.

The double-grating coupler consists of two gratings: one acting as an outcoupler to couple the guided light from a waveguide to its radiation mode, and the other acting as an incoupler to couple the light in the radiation mode to the guided mode of another waveguide. The coupling between these two waveguides is therefore achieved. Since the coupling does not require field overlap between the guided modes of the two waveguides, the separation between the two waveguides can be large. This advantage leads to promising applications in optical integration in multi-layer photonic integrated circuits. A transfer efficiency of 29% is achieved between two SOI waveguides, and further optimization is possible by using blazed-gratings and Bragg reflectors.

In the second part of this thesis, we investigate a new theory for nonlinear frequency conversion in directional couplers. As is well known, when a harmonic oscillator is driven at resonance by an external harmonic force, the largest possible oscillation amplitude is obtained. Coupled mode theory shows that similar phenomena occur when the nonlinear effect takes place in a waveguide directional coupler. We show that by considering the amplitude of the second harmonic signal in the coupled waveguides as an oscillator and the nonlinear polarization as an external harmonic force, a resonant condition can be found, resulting in highly efficient power transfer from pump to signal. Similar resonant effects also occur in other nonlinear frequency conversion effects. The proposed phenomena can also be understood by phase-matching between the supermodes of directional couplers. On one hand, the new theory has fundamental significance for

nonlinear optics, on the other hand, it also demonstrates that waveguide directional couplers can be found in a new application area besides integrated optics and optical communication. We also report the first experimental observation of continuous-wave second-harmonic generation in waveguide directional couplers. We employ a GaAs/AlGaAs system and observe four resonance peaks in a ~15nm spectral range, with a maximal conversion efficiency of $1.6\%W^{-1}cm^{-2}$. This new configuration has the potential to open a new range of applications for nonlinear frequency conversion.

Sommaire

Les guides d'ondes couplés, tels que les coupleurs directionnels et les coupleurs directionnels assistés par réseaux, ont beaucoup d'applications dans l'optique intégrée et dans les systèmes non-linéaires utilisés en communication optique. Les résultats d'études sur deux applications importantes des coupleurs directionnels, l'amélioration de l'intégration optique et la conversion de fréquence, sont présentés dans cette thèse. Elle est donc divisée en deux parties principales. La première traite d'un coupleur compact à double réseaux qui connecte des guides d'ondes fabriqués sur un substrat de silicium sur isolateur (SOI). Ce type de coupleur de guide d'ondes a des applications prometteuses dans les circuits photoniques multicouches. La deuxième partie contient une étude sur la conversion non-linéaire de fréquence, telle que la génération de deuxièmes harmoniques, dans des coupleurs directionnels.

Le coupleur assisté par réseaux se compose de deux réseaux: l'un couple la lumière guidée du guide d'ondes aux modes de rayonnement, et l'autre couple la lumière provenant des modes de rayonnement aux modes guidés du second guide d'ondes. Une connexion entre ces deux guides d'ondes est donc accomplie. Puisque le couplage n'exige aucun chevauchement des champs des deux guides d'ondes, la distance entre les deux guides peut être grande. Ceci permet de créer de nouvelles configurations pour les circuits intégrés photoniques multicouches. Une efficacité de transfert de 29% est obtenue entre deux guides d'ondes SOI, et ce pourcentage peut être amélioré en utilisant des réseaux à angle et des réflecteurs de Bragg.

La deuxième partie de cette thèse explore une nouvelle théorie pour la conversion non-linéaire de fréquence avec des coupleurs directionnels. Comme tous le savent, lorsqu'un oscillateur est opéré à sa fréquence de résonance par une force externe, l'on obtient la plus grande amplitude possible. La théorie des modes couplés prédit qu'un phénomène similaire se produit lorsque qu'un effet non-linéaire est présent dans un coupleur directionnel. Cela est démontré en interprétant l'amplitude du deuxième signal harmonique dans le coupleur comme un oscillateur et l'effet de polarisation non-linéaire comme une force harmonique externe. Ainsi, un état de résonance qui maximise le transfert de puissance de la pompe au signal peut être trouvé. Des effets de résonance

semblables se produisent également avec d'autres effets non-linéaires de conversion de fréquence. La théorie proposée peut également être expliqué par un assortiment de phase entre les supermodes des coupleurs directionnels. Cette nouvelle théorie a une signification fondamentale pour les systèmes optiques non-linéaires et elle démontre également que les coupleurs directionnels peuvent être utiles pour des applications autres que les télécommunications optiques. La première observation expérimentale de génération continue de deuxième harmonique dans des coupleurs directionnels est également présentée. Elle fut accompli avec des guides d'onde en GaAs/AlGaAs et quatre crêtes de résonance dans une gamme spectrale de ~15nm furent observées. L'efficacité maximale de conversion de cette nouvelle configuration est de $1.6\%W^{-1}cm^{-2}$. Cette configuration a le potentiel de permettre une nouvelle gamme d'applications pour la conversion de fréquence non-linéaire.

Acknowledgements

First of all, I wish to sincerely thank my supervisor Prof. Andrew G. Kirk for his helpful guidance and tireless encouragement over the course of my PhD studies. He was there with me during every step over the course of my research. I appreciate his innovative ideas and valuable advice. His conscientious and careful attitude toward the research and his clear and attractive presentation greatly influence me. I am also deeply indebted to him for the great trust he has placed in me and the endless patience he showed with my language errors.

I owe my deepest thanks to all of my research collaborators, without whom, this thesis would not be possible. Particular thanks go to Prof. J. Azana (presently at INRS-EMT, Univ. du Quebec) for his work on fiber Bragg gratings, Dr. A. Jugessur for his work on lithography and etching, Dr. E. Grondin and Prof. V. Aimez at Sherbrooke University for their work on ebeam lithography, J. Upham for his work on optical setup and sample polishing, and S. Bhatnagar and Dr. M. Nannini for their work on wafer bonding.

Many thanks go to all members of the Photonics Systems Group at McGill University, particularly to Prof. D. Plant and Prof. L. Chen for their insights and reviews of my research work, N. Bélanger and Dr. J. Laniel for the helpful discussion on the experiment of second-harmonic generation, N. Bélanger and E. Bisaillon for their excellent work as lab managers, Dr. E. Lugo, C. Alleyne, C. Marinescu, M. Ménard, M. Mony, Y. Zuo and D. Pudo for their demonstration of the use of experimental instruments, C. Rolston for his help with everything, A. Bakhtazad, X. Bing, and W. Tang for helpful discussions on everything, and all the others whose name I may forget to mention here.

I greatly appreciate V. Logiudice, N. Lemaire, D. W. Berry, R. Gagnon at McGill University, and H. Lee at Toronto University for assistance with micro-fabrication.

I would like to thank Peter Bienstman (University of Ghent) for making the CAMFR software available.

Thank you all of my dear friends in Montreal who always made my life at McGill more enjoyable and meaningful.

Finally, I wish to dedicate this work to my parents and wife, for their continuous encouragement and love during my years at McGill.

TABLE OF CONTENTS

LIST OF FIGURES

Publication List

The work reported in this thesis has been published or will be published in the form of the following journal articles and conference papers. The contributions of co-authors have been stated in the Acknowledgements of this thesis.

Journal papers:

[1] P. Dong, J. Azana, and A. G. Kirk, "Synthesis of fiber Bragg grating parameters from reflectivity by means of a simulated annealing algorithm," *Opt. Commun.*, vol. 228, pp. 304-308, Dec. 2003.

[2] P. Dong, and A. G. Kirk, "Nonlinear frequency conversion in waveguide directional couplers," *Phys. Rev. Lett.*, vol. 93 (13), pp. 133901, Sep. 2004.

[3] P. Dong, and A. G. Kirk, "Compact double-grating coupler between vertically stacked silicon-on-insulator waveguides," Accepted by *App. Opt.*, Aug. 2005.

[4] P. Dong, and A. G. Kirk, "On nonlinear frequency conversion in waveguide directional couplers," In submission.

[5] P. Dong, J. Upham, J. Jugessur and A. G. Kirk, "Continuous-wave second-harmonic generation in semiconductor waveguide directional couplers," In submission.

Conference papers:

[6] P. Dong, and A. G. Kirk, "A double-grating coupler for efficient coupling between vertically integrated optical waveguides," Published in the *Symposium of the Conference of Photonics North*, May 2003, Montreal, Canada.

[7] P. Dong, and A. G. Kirk, "Compact grating coupler between vertically stacked silicon-on-insulator waveguides," *Proceeding of SPIE (Optoelectronic integration on silicon)*, vol. 5357, pp 135-142, 2004.

[8] M. Nannini, G. Androz, V. Aimez, P. Dong, A. Kirk, D. Plant, T. Ahoyo, M. Duguay, and J.E. Broquin, "Heterogeneous integration of passive/active photonic components: comparison of two approaches," Published in the *Symposium of the Conference of Eleventh Canadian Semiconductor Technology Conference*, Ottawa, Canada, 18-22 August 2003.

[9] P. Dong, and A. G. Kirk, "Second-order Bragg waveguide grating as a 1D photonic band gap structure in SOI waveguide," *Proceeding of SPIE*, vol. 5577, pp. 589-597, Dec. 2004.

[10] A. G. Kirk, M. Menard, P. Dong, and E Bisaillon, "Integration strategies for micro-optical systems," *Proceeding of SPIE*, vol. 5453, pp. 83-88, Sep. 2004, invited talk.

[11] P. Dong, and A. G. Kirk, "Nonlinear frequency conversion in waveguide directional couplers," *Proceeding of SPIE*, Photonics Asia, Nov. 2004, Beijing, China.

[12] P. Dong, and A. G. Kirk, "Nonlinear optical harmonic oscillator results in efficient frequency conversion," *Conference on Lasers and Electro-Optics (CLEO)*, paper CFL7, May 2005, Baltimove, USA.

Patent:

[13] P. Dong, "Apparatus for efficient optical frequency conversion," US/Canada provisional patent filed on 2004/03/01, PCT with reference number PCT/CA2005/000301 filed on 2005/02/28.

CHAPTER 1 INTRODUCTION

1.1 Background on waveguide couplers

Optical dielectric waveguides are the structures that confine and guide the light in the guided-wave devices and photonic integrated circuits. In order to couple the light between two waveguides, waveguide couplers have to be used. Optical waveguide couplers are devices that transfer the light from one waveguide to another waveguide, or from one mode of a waveguide to another mode of the waveguide. For instance, a directional coupler transfers the light from a waveguide to its neighboring waveguide; a grating outcoupler/incoupler couples the light between a waveguide's radiation modes and guided modes; a fiber Bragg grating (FBG) converts a forward-propagating mode of a fiber to its backward-propagating mode; a tapered waveguide coupler conveys the light in one waveguide to another different waveguide. Many applications for waveguide couplers can be found in the areas of integrated optics, nonlinear optics, fiber optical communication and optical signal processing. Waveguide couplers themselves can be very important parts of a photonic component, for example, in distributed Bragg lasers the grating coupler provides the functions of reflectivity and mode selection; in FBG sensors, FBGs whose transmission and reflection properties are affected by the environment parameters (for example, temperature or stain) perform reflecting the light; optical switches, modulators or splitters can be made from directional couplers [1][2]. In the following subsections, directional couplers and grating couplers which are relevant in this thesis will be individually presented.

1.1.1 Directional coupler

Directional couplers consist basically of two parallel optical waveguides which are sufficiently closely spaced so that the overlapping evanescent tails of the modes guided in the two waveguides is nonzero [1][2]. Because of the interaction between two modes, the light can be transferred from one to the other waveguide. The output power distribution depends on both launch condition and the length of directional couplers. The fraction of the power coupled per unit length is determined by the separation distance of the two

waveguides. In general, a smaller separation distance results in larger modal overlap, and thus the coupling strength becomes larger. Under suitable conditions, a light wave launched into one of the waveguides can be transferred completely to the other waveguide, alternatively any desired beam splitting can be realized. Nevertheless, complete exchange of light power is only possible between two modes that have equal phase velocities, called phase synchronism [2]. This is due to the fact that the phase synchronism maintains phase coherence as the light transfers from one mode to another mode. Two identical waveguides naturally produces phase synchronism, and two dissimilar waveguides normally do not have phase synchronism. Grating structures can be used to compensate for the difference between phase velocities in two dissimilar waveguides, called grating-assisted directional couplers.

Directional couplers have many applications in integrated optics and optical communication systems [3]. They can be used as power dividers, with in principle any arbitrary power splitting ratio achievable by proper design of the length of the directional couplers. They can be also used as input or output couplers, and directionally selective taps on an optical data bus. Directional couplers can also serve as wavelength filters, by using couplers made of two identical waveguides or dissimilar waveguides. Since the coupling strength depends on the wavelength, couplers made of two identical waveguides can be designed to permit complete exchange of power at a certain wavelength. If two dissimilar waveguides are used, the filter can become narrower by achieving phase synchronism only in a narrow wavelength range. While the previously discussed applications are all examples of passive applications, another important application of directional couplers is as an active modulator or switch, in which the coupled power is externally controlled. One example is to use electro-optic materials exhibiting the Kerr effect in one or both waveguides. The refractive index and hence the effective index of the waveguides can be controlled by applying electric fields. The modification of the effective index influences the phase synchronism between modes in two waveguides, permitting a modulation of the coupling efficiency. By this way, a modulator or switch can be realized [4].

In the second half of this thesis, I will present a new application of directional couplers in nonlinear frequency conversion.

1.1.2 Waveguide grating coupler

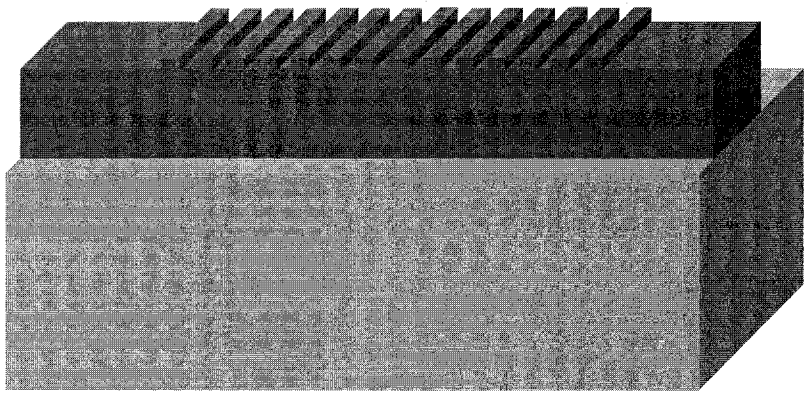

Figure 1.1. A grating fabricated on a waveguide is called waveguide grating. In this diagram, the grating is on a planar channel waveguide. In other cases, gratings may be fabricated in fibers.

A grating fabricated on a waveguide can function to convert one waveguide mode to another mode. This kind of waveguide grating coupler has many forms, such as grating incoupler/outcouplers which couple the light between radiation modes and guided modes, distributed Bragg waveguides and FBGs which convert the forward guided mode to the backward guided mode, and grating-assisted directional couplers. Because of the periodic nature, the gratings perturb the waveguide modes in the grating region and cause them to have a set of space harmonics with z-direction propagation constants given by [3]

$$\beta_v = \beta_1 + \frac{2\pi v}{\Lambda} \tag{1.1}$$

where β_1 is the effective refractive index for, say mode 1 of the waveguide, $v = 0, \pm 1, \pm 2, ...$, and Λ is the period of the grating. In the above equation, we assume that the grating is so weak that the change of the effective refractive index is negligible. If this condition cannot be satisfied, careful attention should be paid to the effective refractive index in the grating region. If another waveguide mode, say mode 2, has an effective index which satisfies the following phase matching condition:

$$\beta_v = \beta_2, \tag{1.2}$$

the energy carried in mode 1 can be transferred to that of mode 2 because of the phase synchronism.

Grating incouplers convert the light of radiation modes which propagate at a specific angle θ and thus a z-component wave number $kn\sin\theta$ (k is the wave number and n is the refractive index of the cladding layer) to a guided mode. From Eq. (1.2), the phase matching condition now is:

$$\beta_2 = kn\sin\theta + \frac{2\pi v}{\Lambda} \tag{1.3}$$

where β_2 is the effective refractive index for the guided mode. By this way, the grating coupler can be used to selectively transfer energy from an optical beam (radiation modes) to a particular waveguide guided mode by proper design of the grating period and the incident angle. By reciprocity, the grating can also be used as outcoupler where guided modes are coupled out at specific angles. Hence, grating incouplers/outcouplers can realize the coupling of optical energy between waveguide systems and free space or fiber systems. The coupling efficiency can be greater than 95% if blazed gratings are used [5]-[7].

Fiber Bragg gratings and distributed Bragg waveguides act so as to reflect a forward guided mode to its backward counterpart, namely, $\beta_2 = -\beta_1$. From Eq. (1.2), we readily obtain the relationship between the effective index and the grating period:

$$\beta_1 = \frac{\pi}{\Lambda} \tag{1.4}$$

where -1 order diffraction has been used. Distributed Bragg waveguides have been intensively used in distributed feedback lasers. These lasers have a wavelength stability that is far superior to those of ordinary Fabry-Perot lasers because a single oscillating mode can be present at the Bragg wavelength determined by the above equation [1]. FBGs have found many applications in optical communication systems and fiber sensors, such as fiber lasers and amplifiers, tunable filters, add/drop multiplexers and comb and superstructure devices, strain or temperature sensors [8].

Another kind of important grating is the so-called second-order grating, in which the -2 order diffraction reflects a forward guided mode to its backward counterpart. Similar to Eq. (1.4), we find that

$$\beta_1 = \frac{2\pi}{\Lambda} \tag{1.5}$$

From the phase-matching of Eq. (1.3), it is readily known that the -1 diffraction couples the light out of the waveguide at 90-degree (namely, $\theta = 0$), producing a surface-normal propagating field. Such second-order gratings have found many applications for integrated optics, including grating incouplers and outcouplers, codirectional and contradirectional waveguide couplers, fiber Bragg gratings, distributed feedback (DFB) or distributed Bragg reflector (DBR) laser structures [9]-[11] .

1.2 Vertical integration of waveguides

The area of photonic integrated circuits (PICs) has been undergoing rapid development and will have huge potential in the future. Optical fiber systems have become a major information-transmission system in both terrestrial and undersea installations due to both their high transmission capacity and the demands of high data-rate of today's network [12]. While the transmission media are mainly fiber systems, the transmitter, receiver, amplifier and filtering systems are mainly based on PICs. There are numerous passive and active optical devices based on PICs which perform complex networking functions, such as optical switching, routing, optical amplifying, light sources, optical detecting, wavelength-division multiplexing, optical signal restoration, optical modulation and demodulation. At the same time, some researchers claim that the performance of future high performance integrated electrical circuits may be limited by interconnect capacity, both on-chip and off-chip. As a result the potential of faster clock speeds and greater device densities may not be fully realized. Optical interconnects constructed by hybrid PICs and electrical circuits (free-space transmission may be involved) represent a radical alternative to electronic interconnects. Optical signals can be transmitted at higher data rates with lower cross-talk, and one key advantage of optical transmission is that it does not have any of the limitations of distance-dependant capacitive and inductive degradation which electrical interconnections suffer from. This means that both remote memory and local cache memory can be accessed with the same ease. Many different researchers have been investigating this issue in recent years and some progress has been made [13][14]. Both areas require advances in integrated optics to enable compact

integrated optical circuits and optically interconnected ICs based on hybrid photonic and electronic integrated chips.

Nevertheless, large-scale integration of photonics components is extremely difficult compared with the development of electrical circuits. Although the concept of PICs has been proposed for more than four decades, the highest large-scale PICs reported up to now have only the level of integration about 50 components per chip [15]. Even such PICs still remain in the research laboratory rather than industry. This number is far below the integration level of electrical ICs, which can be multiple million components per chip. This situation is mainly due to the fact that two significant challenges still remain in integrated optics. The typical length scale of optical components is several orders of magnitude larger than that of their electronic counterparts. Therefore one of the biggest challenges of photonic circuits is to miniaturise these devices. Another challenge is to combine different types of waveguide optimized for different requirements, for example, SiO_2 waveguides for routing and InP waveguide for amplification. In PICs, waveguides are usually the construction blocks for optical components. Waveguide couplers connecting different optical components in PICs therefore play very important roles in the optical integration. Nevertheless, waveguide couplers face much more challenges, compared with electrical connections, due to the following facts. Firstly, unlike electrical currents, the phase of a light wave (which is an electromagnetic wave) plays a critical role in the propagation of the wave. For example, the phase of a light wave is represented by kz, where k is the wave number defined by $k = \frac{2\pi}{\lambda}$ and z is the propagation distance. Since the wavelength of a light wave is so small (~1 μm), even a very short propagation distance will significantly change the phase. From the wave number, one can deduce the phase velocity in a uniform material or in a waveguide structure. For different modes of a waveguide, or for the modes of different waveguides, the phase velocities may differ, which results in many difficulties to transfer one mode to another mode. Grating structures or tapered structures [16] may be required to compensate for the wave number difference. Secondly, the beam profiles for different waveguide modes may be quite different, for example, a guided mode has very different cross-section profile from that of a radiation mode in a waveguide, and a small-core waveguide may have much smaller

beam diameter than that of a large-core waveguide. Usually the coupling efficiency between two waveguide modes depends on the cross-sectional profile overlap between these two modes. As a general rule, larger beam-profile difference between two modes results in lower coupling efficiency between them. A 90° bending for waveguides is therefore not allowed since huge losses may occur due to the fact that the wave number has changed (in this case, it is better to consider the wave number as a vector) and the field overlap between the mode before bending and the mode after bending is small. In summary, waveguide couplers play very important roles in the applications of PICs, designing and fabricating waveguide couplers connecting different photonic components have more challenges than electrical connections.

The vertical integration of stacked waveguides for photonic circuits onto a single substrate is a promising configuration to enable the dense monolithic or hybrid-lithic integration of three-dimensional photonics devices. In addition, the stacked configuration is important to the flexible layout of photonic circuits. This is analogous to electric integrated circuits which have a multilayered structure (up to several tens of layers) for more dense integration. While there have been a number of reports of stacked waveguides consisting of semiconductors, polymers, or dielectric materials [17]-[24], very few multilayered practical PIC devices have been reported. Efficient coupling of the light between vertical integrated waveguides is a key issue and the biggest challenge. In particular, a small-size, highly efficient coupler is required for dense integration of photonic circuits. Present research on coupling between vertically integrated waveguides consists of two main different methods. The first type is a directional coupler (including grating-assisted directional coupler) or tapered structure where adiabatic coupling between guided modes is realized [16]-[23]. A particularly promising example is asymmetric twin-waveguide (ATG) technology with taper couplers [25][26]. The power is transferred from an active layer to a passive layer by vertical directional couplers. However, this requires a very small waveguide separation between two layers. The second type utilizes gratings to transfer guided power in one waveguide to the other through radiation modes [27]-[29]. In this coupling configuration, one grating realizes outcoupling from the first waveguide into radiation modes, another grating incouples the

radiated light into the guided mode of the second waveguide. To our knowledge, only a few reports investigated such coupling configuration mainly due to the fact that the high radiation loss to substrates makes the coupling efficiency low. However, this coupling scheme has the advantage of applicability to a planar multi-layer structure and no requirement on the minimum distance between two waveguides (i.e., the overlap between two guided modes is not required). To date the potential of this kind of coupler is still not fully exploited. In the first part of this thesis, we will theoretically investigate a similar compact double-grating coupler structure which realizes coupling between two stacked high-index-difference SOI waveguides by radiation modes.

1.3 Nonlinear frequency conversion

Nonlinear optical effects for frequency conversion generate coherent light at frequencies where lasers are not convenient, and have become a widely used technique that finds applications in fields as diverse as high-density optical recording, printing, high-resolution laser pattern generation, laser fusion, industrial and medical spectroscopic systems, precision metrology, and optical signal processing [30]. Nonlinear-optical frequency conversion originates in the nonlinear response of the material polarization to an applied optical field. The nonlinear response can be classically viewed as the response of an electron driven by an electromagnetic field in an anharmonic potential well which results from the inter-atomic electric field in the medium [1]. Since the first demonstration of frequency doubling by P. Franken in 1961 [31], nonlinear frequency conversion has become an efficient means to generate radiation in various spectral regions by the effects of sum frequency, difference frequency, third harmonic generation and four-wave mixing. For instance, second-harmonic generation (SHG) has been extensively used to generate green light from the powerful YAG laser which emits 1-μm radiation; whereas difference-frequency generation has been successfully used for tunable laser sources such as optical parameter oscillators [32]. Efficient conversion requires the use of materials which possess a large nonlinear susceptibility. Among the best known of these are nonlinear crystals such as KDP, $LiNbO_3$, KTP ($KTiOPO_4$), AgGaSe, organic nonlinear materials, GaAs/AlGaAs, and semiconductor quantum wells [30]. While traditional crystals such as KDP or LiNbO3 have been commercialized for several

decades, III-V semiconductors such as GaAs are particularly attractive because of their high values of the nonlinear susceptibility. However, there is another particularly important requirement for efficient conversion, that is phase-matching between pump waves and generated waves. Exampled by the process of SHG, the pump wave and the second-harmonic normally have different phase velocities in the nonlinear medium due to material dispersion. This produces a phase difference between the second-harmonic generated at different location and this phase difference accumulates along the length of the medium. After a distance, called "coherence length", the phase difference reaches π and the converting from the second harmonic to the fundamental pump starts. Therefore, the effective length of conversion is limited by the coherent length. Phase-matching conditions are therefore necessary to efficiently increase the interaction length. In phase-matched situation, the velocities of the fundamental wave and second harmonic are equal, and this condition expresses, quantum-mechanically, the photon momentum conservation [32]. Phase-matching can be obtained by birefringence exhibited by some crystals as KDP or $LiNbO_3$ [30] and structured isotropic nonlinear materials [33]. In birefringent materials, the phase velocity of a wave depends on the polarization of the wave, and therefore, careful chosen of the polarization of the fundamental wave and second harmonic can realize phase-matching condition. However, isotropic materials, such as GaAs, are non-birefringent and phase-matching is impossible. Quasi-phase matching provides another useful technique by introducing a periodic change in the sign of the medium's nonlinear susceptibility which periodically compensates for the phase difference accumulated during a coherence length [34]-[36]. This phase-matching scheme obtained much success in recent years due to mature poling techniques and crystal growth techniques. In a waveguide structure, the phase velocities of waves can be controlled by the choice of the dimensions and refractive indices of the core layers and cladding layers. By choosing different guided modes for the second harmonic and the fundamental wave, modal-phase matching can be realized [37], whereas, phase matching between guided modes for the fundamental wave and radiation modes for the second harmonic results in Cerenkov phase matching [38]. By incorporating the above phase-matched means, SHG has been reported in quasi-phase matched GaAs films [39][40] and modal-phase-matched GaAs/AlGaAs waveguides [41][42]. In the second part of this thesis, we will investigate

nonlinear frequency conversion in directional couplers, rather than bulk materials and single waveguides.

1.4 Outline of this thesis

In this section, a brief description of my PhD research is presented, followed by original contributions and thesis organization.

1.4.1 Brief description of research

In the first part of this thesis, we investigate a double-grating coupler for vertically stacked waveguides with the main advantage of compactness. This coupling structure utilizes radiation modes, instead of guided modes, as a bridge mode between two waveguides. In this study, deep and short second-order gratings are employed with the main advantage of compactness. Fig. 1.2 shows the proposed coupling configuration. Two guiding-core layers are stacked on silicon substrates with an optical separation layer and a grating coupler is integrated on each waveguide. The physics behind this structure is straightforward: an incident guided wave propagating in the lower waveguide is coupled into radiation modes by the grating coupler GC1. The radiation modes are then coupled into the upper waveguide by the grating coupler GC2. In our design, we use deep and short second-order gratings where the first-order diffraction couples the light out of the waveguide into a surface-normal (or near normal) propagating field. From the reciprocity principle, a propagating field normal to such a waveguide grating can also be coupled into a guided wave. The compactness of this coupler is realized by the deep gratings which have strong interaction between guided modes and radiation modes.

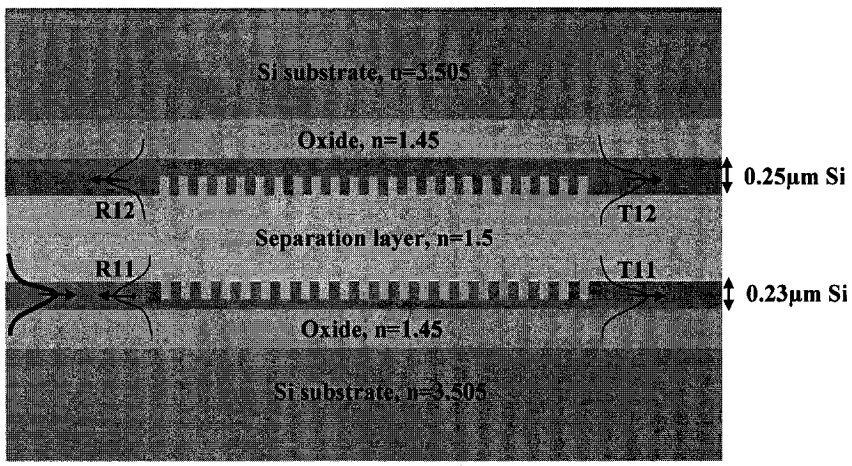

Figure1.2. Cross-sectional diagram of coupling between two vertically integrated silicon waveguides.

In the second part of this thesis, we investigate a new theory for nonlinear frequency conversion in directional couplers. As is well known, when a harmonic oscillator is driven at resonance by an external harmonic force, the largest possible oscillation amplitude is obtained. The coupled mode theory shows that similar phenomena occur when the nonlinear effect takes place in a waveguide directional coupler. In doing so, we have found a new technique for efficient second harmonic generation (SHG). We show that by considering the amplitude of the second harmonic signal in the coupled waveguides as an oscillator and the nonlinear polarization as an external harmonic force, a resonant condition can be found which results in highly efficient power transfer from pump to signal. Similar resonant effects also occur in other nonlinear frequency conversion effects. The proposed nonlinear-optical harmonic oscillator provides an important alternative method to obtain efficient nonlinear frequency conversion. On one hand, the new theory has fundamental significance for nonlinear optics, on the other hand, it also demonstrates that waveguide directional couplers can be found in a new application area besides integrated optics and optical communication.

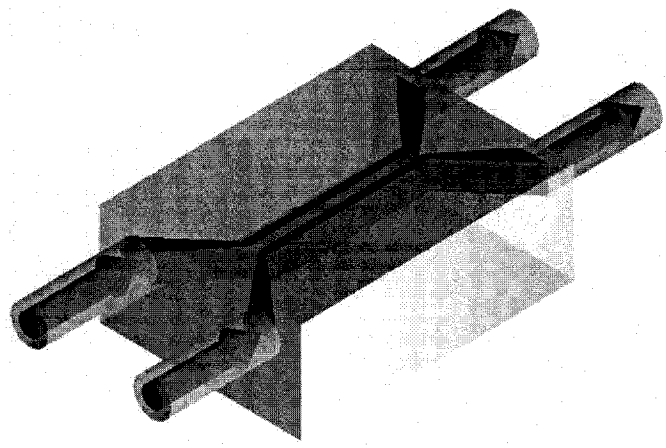

Figure 1.3. A possible future device based on the proposed theory. Pump wave(s) are incident from the fiber to the tapered waveguides. After the new waves are efficiently generated in the directional coupler, they are collected by two other tapered waveguides and subsequent fibers. This structure solves the coupling problem between the outside world and the directional coupler. It is to be noted that the incident fibers could be replaced directly by semiconductor lasers. By this way, an integrated device acting as a blue-green light source could be fabricated which employs second or third harmonic generation.

1.4.2 Original Contributions

The content of this thesis is leading to the following original contributions to the field:

- First systematic study of deeply etched second-order Bragg gratings in silicon-on-insulation waveguides (Chapter 3).
- First systematic analysis of a compact (~12μm), dielectric double-grating waveguide coupler for vertically integrated waveguides (Chapter 4).
- First use of the eigenmode expansion method to analyze the double-grating coupler structure. This method is faster than the finite-difference time-domain method, and is sufficiently accurate for optimization and design purposes (Chapter 4).

- First use of coupled-mode theory to study nonlinear frequency conversion in waveguide directional couplers (Chapter 5 and Chapter 6).
- First theoretical study and proposal of a resonance phenomenon for nonlinear frequency conversion in directional couplers (Chapter 5 and Chapter 6).
- First experimental demonstration of second-harmonic generation in semiconductor waveguide directional couplers (Chapter 7).

1.4.3 Thesis organization

This thesis is organized as follows. Chapter 1 provides the overview of different types of waveguide couplers and their applications, the background of integration of photonic devices and waveguide coupler's roles in this area, the simple description of nonlinear frequency conversion and their applications, and the outline of this thesis.

Chapter 2 presents some basic theories to deal with waveguide couplers. These theories include coupled mode theory which is suited to simulate directional couplers, the finite-difference time-domain method and the eigenmode expansion method which are two strict electromagnetic theories and suited to model finite-size photonic devices. In the following chapters, all simulations are based on these methods.

Chapter 3 focuses on the theoretical study of the modal reflection, transmission and radiation properties of deeply etched second-order Bragg waveguide gratings in silicon-on-insulator (SOI) slab waveguides. This study is initially aimed to serve the following investigation of double-grating couplers in vertically integrated SOI waveguides. We find that high reflection can be obtained with a very short grating structure. The out-of-plane radiation efficiency can be controlled by the grating depth and groove width. This structure has potential for use in microcavity lasers, compact outcouplers and incouplers, and surface-emitting lasers. Two application examples will be predicted, one involves a double-grating coupler to realize efficient coupling between vertically integrated waveguides over short distances which will be the main content of Chapter 4, and the other is a photonic-bandgap surface-emitting microcavity.

Chapter 4 presents our detailed study on double-grating couplers between vertically integrated SOI waveguides. Simulations suggest that a coupling efficiency of 29% is

achievable in coupling the light from one waveguide to another with 12.9μm long binary gratings. We find that the coupling efficiency is enhanced by Fabry-Perot resonance between two gratings. The coupling efficiency can be increased by using blazed gratings. We use the eigenmode expansion method to design and optimize binary grating couplers and the results are verified by using the finite-difference time-domain method.

Chapter 5 provides our theory of second-harmonic generation (SHG) in directional couplers. The coupled-mode equations to describe the behavior of SHG and directional couplers will be presented and the solutions under non-depletion assumption will be discussed. Under some resonance conditions, we find that the generation can be as efficient as conventional perfect phase matching. In this chapter, we also demonstrate that the resonance phenomena can be explained by phase matching between the supermodes of directional couplers.

Chapter 6 focuses on the theory of other nonlinear effects for frequency conversion in directional couplers. These effects include sum-frequency, difference-frequency and third-harmonic generations.

Chapter 7 presents our experimental study of SHG in GaAs/AlGaAs directional couplers. We report the first observation of continuous-wave second-harmonic generation in GaAs/AlGaAs waveguide directional couplers. Four resonance peaks are found in a ~15nm spectral range, and η=~1.6%$W^{-1}cm^{-2}$ is obtained experimentally.

Chapter 8 gives some conclusions of this thesis and some possible future research directions following the present studies.

References

[1] A. Yariv, *Optical Electronics in Modern Communications*, (Oxford University Press, 1997).

[2] K. Okamoto, *Fundamentals of Optical Waveguide*, (Academic Press, 2000).

[3] T. Tamir, *Topics in applied physics, volume 7: integrated optics*, (Springer-Verlag Berlin Heidelberg New York, 1979).

[4] R. G. Hunsperger, *Integrated optics* (Springer-Verlag Berlin Heidelberg New York, 2002).

[5] M. Shams, D. Botez, and S. Wang, "Preferential chemical etching of blazed gratings in (110)-oriented GaAs," *Opt. Lett.*, vol. 4, pp. 96-99, 1979.

[6] A. Gruss, K. T. Tam, and T. Tamir, "Blazed dielectric gratings with high beam-coupling efficiencies," *Appl. Phys. Lett.*, vol. 36, pp. 523-525, 1980.

[7] K. Rokushima, and J. Yamakita, "Analysis of anisotropic dielectric gratings," *J. Opt. Soc. Am.*, vol. 73, pp. 901-908, 1983.

[8] A. Othonos, and K. Kalli, *Fiber bragg gratings: fundamentals and applications in telecommunications and sensing*, (Artech house, INC, 1999).

[9] W. Streifer, D. R. Scifres, and R. Burnham, "Analysis of grating-coupled radiation in GaAs:GaAlAs lasers and waveguides," *IEEE J. Quantum Electron.*, vol. QE-12, pp. 422-428, July 1976.

[10] A. Hardy, D. F. Welch, and W. Streifer, "Analysis of second-order gratings," *IEEE J. Quantum Electron.*, vol. QE-25, pp. 2096-2105, Oct. 1989.

[11] G. W. Taylor and C. Kwan, "Determination of diffraction efficiency for a second-order corrugated waveguide," *IEEE J. Quantum Electron.*, vol. 33, pp. 176-186, Feb. 1997.

[12] G. Keiser, *Optical fiber communications,* (McGraw-Hill Higher Education, 2000).

[13] C. Tocci and H. J. Caulfield, Eds,. *Optical Interconnection, Foundations and Applications,* (Reading, MA: Artech House, 1994).

[14] *IEEE J. Selected Topics Quantum Electron*, vol. 2, No.1, 1996.

[15] R. Nagarajan, et. al, "Large-scale photonic integrated circuits," *IEEE J. Selected Topics Quantum Electron,* vol. 11, pp. 50-65, 2005.

[16] I. Moerman, P. P. Van Daele, and P. M. Demeester, "A review on fabrication technologies for the monolithic integration of tapers with III-V semiconductor devices," *IEEE J. Selected Topics Quantum Electron*, vol. 3, pp. 1308-1320, 1997.

[17] R. A. Soref, E. Cortesi, F. Namavar, and L. Friedman, "Vertically integrated silicon-on-insulator waveguides", *IEEE Photon. Technol. Lett.*, vol. 3, pp. 22-25, Jan 1991.

[18] S. Asakawa, Y. Kokubun, M. Ohyama, and T. Baba, "Three-dimensional optical interconnects by stacked ARROW waveguides," *Electron. Lett.*, vol, 29, no. 16, pp. 1485-1486, 1993.

[19] W. Sotoyama, S. Tatsuura, K. Motoyoshi, and T. Yoshimura, "Directional-coupled optical switch between stacked waveguide layers using electro-optic polymer," *Jpn, J. Appl. Phys.*, vol. 31, no. 8B, pp. L1180-L1181, 1992.

[20] C. Wu, C. Rolland, F. Shepherd, C. Larocque, N. Puetz, K. D. Chik, and J. M. XU, "InGaAsP/InP vertical directional coupler filter with optimally designed wavelength tunability," *IEEE Photon. Technol. Lett.*, vol. 4, pp. 457-459, Apr. 1992.

[21] Z. M. Chuang and L. A. Coldren, "Enhanced wavelength tuning in grating-assisted codirectional coupler filter," *IEEE Photon. Technol. Lett.*, vol. 5, pp. 1219-1221, Oct. 1993.

[22] M. Horita, T. Yamazaki, S. Tanaka, and Y. Matsushima, "Polarization insensitive and tunable optical add and drop multiplexer utilizing vertically stacked buried semiconductor waveguides," *Electron. Lett.*, vol. 35, no. 20, pp. 1733-1734, 1999.

[23] S. M. Garner, V. Chuyanov, S.-S. Lee, A. Chen, W. H. Steier, and L. R. Dalton, "Vertically integrated waveguide polarization splitters using polymers," *IEEE Photon. Technol. Lett.*, vol. 11, pp. 842-844, Jul. 1999.

[24] S. Ura, R. Nishida, T. Suhara, and H. Nishihara, "Wavelength-selective coupling between vertically integrated thin-film waveguides via supermode by a pair of grating couplers", *IEEE Photon. Technol. Lett.*, vol. 13, pp. 678-680, July 2001.

[25] F. Xia, V. M. Menon, and S. R. Forrest, "Photonic integration using asymmetric twin-waveguide (ATG) technology: part I---concepts and theory," *IEEE J. Selected Topics Quantum Electron,* vol. 11, pp. 17-29, 2005.

[26] V. M. Menon, F. Xia, and S. R. Forrest, "Photonic integration using asymmetric twin-waveguide (ATG) technology: part II---devices," *IEEE J. Selected Topics Quantum Electron,* vol. 11, pp. 30-42, 2005.

[27] Q. Xing, S. Ura, T. Suhara, and H. Nishihara, "Contra-directional coupling between stacked waveguides using grating couplers," *Opt. Commun.*, vol. 144, pp.180-182, 1997.

[28] S. Ura, R. Nishida, T. Suhara, and H. Nishihara, "Wavelength-selective coupling among three vertically integrated optical waveguides by grating couplers", *IEEE Photon. Technol. Lett.*, vol. 13, pp. 133-135, Feb. 2001.

[29] T. Liang and R. W. Ziolkowski, "Grating assisted waveguide-to-waveguide couplers," *IEEE Photon. Technol. Lett.*, vol. 10, pp. 693-695, May 1998.

[30] R. W. Boyd, *Nonlinear optics* (Academic Press Inc., 2003).

[31] P. A. Franken, A. E. Hill, C. W. Peters, and G. Weinreich, "Generation of optical harmonics," *Phys. Rev. Lett.*, vol. 7, pp. 118-139, 1961.

[32] M. M. Fejer, "Nonlinear optical frequency conversion," *Phys. Today*, vol. 47, pp. 25-31, 1994.

[33] A. Fiore, V. Berger, E. Rosencher, P. Bravetti, and J. Nagle, "Phase matching using an isotropic nonlinear optical material," *Nature*, vol. 391, pp. 463-465, 1998.

[34] J. A. Armstrong, N. Bloembergen, J. Ducuing, and P. S. Pershan, "Interactions between light waves in a nonlinear dielectric," *Phys. Rev.*, vol. 127, pp. 1918-1939 1962.

[35] V. Berger, "Nonlinear photonic crystals," *Phys. Rev. Lett.*, vol. 81, pp. 4136-4139, 1998.

[36] M. M. Fejer, G. A. Magel, D. H. Jundt, and R. L. Byer, "Quasi-phase-matched second harmonic generation – tuning and tolerance," *IEEE J. Quantum Electron.*, vol. 28, pp. 2631-2654, 1992.

[37] G. L. J. A. Rikken, C. J. E. Seppen, E. G. J. Staring, and A. H. J. Venhuizen, "Efficient modal dispersion phase-matched frequency-doubling in poled polymer waveguides," *Appl. Phys. Lett.*, vol. 62, pp. 2483-2485, 1993.

[38] P. K. Tien, R. Ulrich, and R. J. Martin, "Optical second harmonic generation in form of coherent Cerenkov radiation from a thin-film waveguide," *Appl. Phys. Lett.*, vol. 17, pp. 447-449, 1970.

[39] S. J. B. Yoo, *et al.* "Wavelength conversion by difference frequency generation in AlGaAs waveguides with periodic domain inversion achieved by wafer bonding," *Appl. Phys. Lett.*, vol. 68, pp. 2609-2611, 1996.

[40] T. Skauli, "Measurement of the nonlinear coefficient of orientation-patterned GaAs and demonstration of highly efficient second-harmonic generation," *Opt. Lett.*, vol. 27, pp. 628-630, 2002.

[41] A. Chowdhury, and L. McCaughan, "Continuously phase-matched M-waveguides for second-order nonlinear upconversion," *IEEE Photonics Technol. Lett.*, vol. 12, pp. 486-488, 2000.

[42] S. Ducci, *et al.* "Continuous-wave second harmonic generation in modal phase matched semiconductor waveguides," *Appl. Phys. Lett.*, vol. 84, pp. 2974-2976, 2004.

CHAPTER 2 THEORETICAL BACKGROUND

In this chapter, some important theories used in this thesis will be outlined. Coupled mode theory, which is a powerful technique to deal with directional couplers and Bragg grating waveguides, will be derived based on a perturbation theory. The finite-difference time-domain (FDTD) and eigenmode expansion method (EEM) are two strict electromagnetic theories, and are suited to model small-size devices. Some basic derivations of these two methods are given in this chapter.

2.1 Waveguide modes

Optical waveguides are made of dielectric materials, and normally consist of a core region where the light is confined and a cladding region. The refractive index of the core is higher than that of the cladding and the light confinement is realized by total internal reflection. Taking into consideration that waveguides are made of dielectric materials, the charge density and current density in Maxwell's equations are both zero. This results in the following equations for source-free and time dependent fields:

$$\begin{aligned} \nabla \times \vec{E} &= -\mu_0 \frac{\partial \vec{H}}{\partial t} \\ \nabla \times \vec{H} &= \varepsilon_0 n^2 \frac{\partial \vec{E}}{\partial t} \end{aligned} \tag{2.1}$$

where $\vec{E}$ and $\vec{H}$ are the time dependent vectors of the electric and magnetic fields, ε_0 and μ_0 are the permittivity and permeability in vacuum, $n^2 = \varepsilon(r)$ is the dielectric constant. We assume fields with periodic time dependence in the forms:

$$\begin{aligned} \vec{E}(\vec{r},t) &= \vec{E}(\vec{r})\exp(j\omega t) \\ \vec{H}(\vec{r},t) &= \vec{H}(\vec{r})\exp(j\omega t) \end{aligned} \tag{2.2}$$

where $\vec{E}$ and $\vec{H}$ are complex amplitudes and ω is the angular frequency. Substitution of Eq. (2.2) into Eq. (2.1) results in equations for the complex amplitudes

$$\begin{aligned} \nabla \times \vec{E} &= -j\omega\mu_0 \vec{H} \\ \nabla \times \vec{H} &= j\omega\varepsilon_0 n^2 \vec{E} \end{aligned} \tag{2.3}$$

A simple derivation from the above equations results in the following wave equation:

$$\nabla^2\vec{E}(\vec{r})+k_0^2 n(\vec{r})^2\vec{E}(\vec{r})=0 \tag{2.4}$$

where $k_0^2 \equiv \omega^2\mu_0\varepsilon_0 = (2\pi/\lambda)^2$. The solutions are subject to the continuity of the tangential components of $\vec{E}$ and $\vec{H}$ at dielectric interfaces. Since waveguides are z-invariant structures, a modal field of the waveguides takes the following form:

$$\vec{E}(\vec{r}) = \vec{E}(x,y)\exp(-i\beta z) \tag{2.5}$$

β is called effective refractive index of the waveguide mode and must be determined later on. Substituting Eq. (2.5) into Eq. (2.4), we obtain [1]

$$\left(\frac{\partial^2}{\partial x^2}+\frac{\partial^2}{\partial y^2}\right)\vec{E}(x,y)+\left[k_0^2 n^2(x,y)-\beta^2\right]\vec{E}(x,y)=0 \tag{2.6}$$

Eq. (2.6) is the wave equation that the waveguide modes must obey. Two kinds of solution may occur corresponding to bounded and unbounded states. When β is larger than $n_{cl}^m k_0$ (n_{cl}^m is the maximal index of the surrounding cladding materials) and smaller than $n_{co}k_0$ (n_{co} is the index of the core region), the waveguide mode is well confined and called a guided mode. Otherwise, the energy of waveguide modes spreads out through the medium surrounding the core region, which are called radiation modes. The guided modes normally have discrete values of propagation constants, while the radiation modes belong to a continuum [2]. In some cases, one also finds evanescent modes with pure imaginary propagation constants $\beta = -i\alpha$ and leaky modes with $\beta = \beta_r - i\alpha$. Both these two modes are lossy and decay as $\exp(-\alpha z)$.

One particularly important property of waveguide modes is that all modes of a dielectric waveguide are orthogonal to each other. It is the basis of coupled mode theory and EEM. A complete and elegant derivation can be found in Ref. [3]. Here, we present the final result for the orthogonality of the modes:

$$\begin{aligned}
&\frac{1}{2}\int_{-\infty}^{+\infty}\int_{-\infty}^{+\infty} dxdy\vec{E}_{t1}\times\vec{H}_{t2}^{*} = 0, \beta_1 \neq \beta_2 \\
&\frac{1}{2}\int_{-\infty}^{+\infty}\int_{-\infty}^{+\infty} dxdy\vec{E}_{t1}\times\vec{H}_{t2}^{*} \neq 0, \beta_1 = \beta_2
\end{aligned} \tag{2.7}$$

The subscript t represents the transverse components of the fields. If $\beta_1 = \beta_2$, the integral of $\frac{1}{2}\int_{-\infty}^{+\infty}\int_{-\infty}^{+\infty} dxdy\vec{E}_{t1} \times \vec{H}_{t2}^{*}$ is just the optical power P carried by the eigenmode in the waveguide (this power is propagating along z-direction). The orthogonality of the waveguide modes allows any arbitrary field distribution to be expressed as a superposition of waveguide modes [3]:

$$\begin{aligned} \vec{E} &= \sum_i a_i \vec{E}_i + \int_v dva(v)\vec{E}_v \\ \vec{H} &= \sum_i a_i \vec{H}_i + \int_v dva(v)\vec{H}_v \end{aligned} \tag{2.8}$$

where $\vec{E}_i$ and $\vec{E}_v$ are the guided modes and radiation modes of waveguides, respectively; a_i and a_v are coefficients which can be determined by the orthogonality relations of waveguide modes Eq. (2.7). Here, the summation extends over the discrete set of guided modes and the integration extends over the continuous spectrum of radiation modes. The mode expansion equation showed above is the fundamental basis of coupled mode theory and EEM in the following sections.

2.2 Coupled mode theory

Because of the imperfections of waveguides (there are always the index inhomogeneities or slight changes of the core and cladding sizes), coupling between the different modes of the waveguides always occur. In other cases, mode coupling is expected, for example, corrugated waveguides and FBGs use grating structure to couple forward guided modes to backward guided modes; waveguide grating outcouplers transfer guided modes to radiations modes. Therefore, coupled mode theory which studies such modal coupling has fundamental importance for the design and operation of waveguide components. As shown in the previous section, there are infinite modes for a waveguide, therefore there should be infinite coupled equations in coupled mode theory. For a complete description of such coupled mode theory, one may refer to the reference [4]. In this section, we will focus on coupled mode theory which only deals with coupling among several guided modes. A coupled mode theory only considering two guided modes is already very useful in the study of directional couplers, Bragg waveguide gratings,

FBGs, grating-assisted directional couplers, and optical ring resonators [2]. The derivations in this section mainly followed those in Ref. [1]. In the next section, EEM, which is intrinsically a coupled mode theory considering many modes, will be presented with the purpose to model arbitrary field propagation rather than modal coupling.

For a perfect waveguide, the waveguide modes satisfy Eq. (2.6). For a waveguide which can realize modal coupling, there must be some imperfections (gratings, index inhomogeneities, and so on) from perfect waveguides. We regard these imperfections as perturbations to the perfect waveguides. The total field in the "perturbed" waveguide can be expanded as a superposition of the guided modes of the perfect waveguides. Similar to Eq. (2.8), we have

$$\vec{E}(\vec{r},t)=\frac{1}{2}\sum_{m}A_m(z)\vec{E}_m(x,y)e^{i(\omega t-\beta_m z)}+c.c \tag{2.9}$$

where m indicates the mth discrete eigenmode of Eq. (2.6), $\vec{E}_m(x,y)$ is the modal field. and β_m is its eigenvalue, namely, the effective refractive index. $A_m(z)$ is called the slowly-varying amplitude of the mth mode. If we can solve this amplitude, the motion of the electric field can be fully understood since the waveguide modes have been determined by Eq. (2.6). The purpose now is to obtain the coupled equations for $A_m(z)$.

In Eq. (2.9), the electric field is time dependent, we therefore must go back to Eq. (2.1), from which the following wave equation can be obtained without the assumption of Eq. (2.2) [1]

$$\nabla^2\vec{E}(\vec{r},t)=\mu\varepsilon_0\frac{\partial^2\vec{E}(\vec{r},t)}{\partial t^2}+\mu\frac{\partial^2}{\partial t^2}\vec{P}(\vec{r},t) \tag{2.10}$$

The total polarization can be expressed as

$$\vec{P}(\vec{r},t)=\vec{P}_0(\vec{r},t)+\vec{P}_{pert}(\vec{r},t)=[\varepsilon(\vec{r})-\varepsilon_0]\vec{E}(\vec{r},t)+\vec{P}_{pert}(\vec{r},t) \tag{2.11}$$

Without the presence of perturbation polarization $\vec{P}_{pert}(\vec{r},t)$, one just obtains the wave equation (Eq. (2.6)) for waveguide structure with dielectric constant $\varepsilon(\vec{r})$. The perturbation polarization represents any deviation of the polarization from that of the unperturbed waveguide [1]. Substituting Eq. (2.11) into Eq. (2.10), we obtain

$$\nabla^2\vec{E}(\vec{r},t)-\mu\varepsilon(\vec{r})\frac{\partial^2\vec{E}(\vec{r},t)}{\partial t^2}=\mu\frac{\partial^2\vec{P}_{pert}(\vec{r},t)}{\partial t^2} \tag{2.12}$$

Substitution of Eq. (2.9) into Eq. (2.12) results in

$$\begin{aligned}&e^{i\omega t}\sum_m\left[\frac{A_m(z)}{2}\left(\left(\frac{\partial^2}{\partial x^2}+\frac{\partial^2}{\partial y^2}\right)\vec{E}_m(x,y)+\left[k_0^2n^2(x,y)-\beta_m^2\right]\vec{E}_m(x,y)\right)e^{-i\beta_m z}\right.\\&\left.+\frac{1}{2}\left(-2i\beta_m\frac{dA_m(z)}{dz}+\frac{d^2A_m(z)}{dz^2}\right)\vec{E}_m(x,y)e^{-i\beta_m z}\right]+c.c=\mu\frac{\partial^2\vec{P}_{pert}(\vec{r},t)}{\partial t^2}\end{aligned} \tag{2.13}$$

From Eq. (2.6), we readily find that the sum of the first three terms produces zero. In most of cases, the following assumption is satisfied:

$$\left|\frac{d^2A_m(z)}{dz^2}\right|<<\beta_m\left|\frac{dA_m(z)}{dz}\right| \tag{2.14}$$

which is called slowly-varying approximation for the amplitudes. Eq. (2.13) is reduced to

$$\sum_m-i\beta_m\frac{dA_m(z)}{dz}\vec{E}_m(x,y)e^{i(\omega t-\beta_m z)}+c.c=\mu\frac{\partial^2\vec{P}_{pert}(\vec{r},t)}{\partial t^2} \tag{2.15}$$

The above equation is the coupled mode equation used to treat a large variety of mode interactions. By using the orthogonolity property of the modes, one can reduce this equation further. For different physical examples, such as directional couplers and Bragg gratings, the perturbation polarizations will be different, but all lead to a set of coupled first-order differential equations for the amplitudes A_m. Detailed examples can be found in Refs. [1]-[2], and in Chapter 6 we will present the detailed derivation for second harmonic generation in directional couplers in which we demonstrate the use of Eq. (2.15).

2.3 Eigenmode expansion method

We have found that the coupled mode theory in the previous section is a perturbation theory with some approximations: (1) The electric field within the whole structure is expanded as the superposition of ONE set of waveguide modes, which we can call the ideal modes of the unperturbed waveguides. This condition is only true when the perturbed waveguide does not differ much from the unperturbed waveguide. (2) To effectively use the coupled mode theory, one always reduces the number of interactive

modes to a few. Certainly, this is only true when the interaction among all the other modes is negligible. If we intentionally get rid of the above two approximations, we can develop a strict electromagnetic theory, so-called eigenmode expansion method (EEM). Fig. 2.1 illustrates the basic idea of EEM. The investigated structure can be regarded as a stack consisting of N z-invariant layers, and each layer can be regarded as an independent waveguide and has its own waveguide modes. Therefore, the fields in each layer can be expanded as a superposition of the waveguide modes of the local layer. The propagation of the field in each layer can be expressed by Eq. (2.9), but m here may extend to radiation modes. At interfaces, however, reflection and transmission will occur, and they can be calculated by mode matching, namely, the continuity of the tangential components of the total field at the interfaces. After we know the reflectivity and transmission at each interface and the propagation in each layer, the propagation through the whole structure can be calculated by basic matrix multiplications. In Sec. 2.1, we have presented the waveguide modes, and we only need to focus on the mode matching at interface and the propagation through the whole stack.

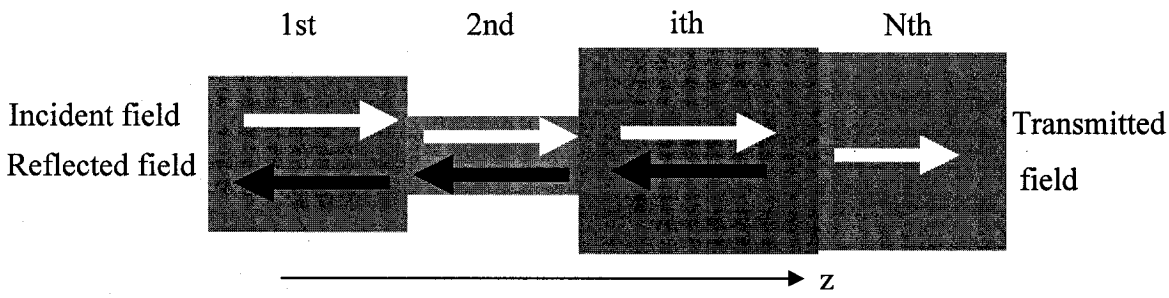

Figure 2.1. Basic description of the EEM method.

2.3.1 Mode matching at interface

The method presented in this section is mainly followed that in Ref. [6]. As shown in Fig. 2.2, we consider the interface between waveguide I and II. The incident field is a particular waveguide mode of waveguide I, say mode p. From mode matching, we find

$$\begin{aligned} \vec{E}^{I}_{p,t} + \sum_{j} R_{j,p} \vec{E}^{I}_{j,t} &= \sum_{j} T_{j,p} \vec{E}^{II}_{j,t} \\ \vec{H}^{I}_{p,t} - \sum_{j} R_{j,p} \vec{H}^{I}_{j,t} &= \sum_{j} T_{j,p} \vec{H}^{II}_{j,t} \end{aligned} \tag{2.16}$$

Here, the superscript represents waveguide I or II; the first index in the subscript, j, is the mode number and the second index represents the transverse component. The left-hand sides are the transverse-component of the fields in waveguide I at the interface and the right-hand sides is that in waveguide II. Therefore, the above equations come from the continuity of the tangential components of the total field at the interface. The minus sign in reflected H field results from the symmetries for the backward-propagating modes (we refer to Ref. [3] for detailed derivation). For a given structure, the waveguide modes are known, therefore, we need to calculate the unknown expansion coefficients $R_{j,p}$ and $T_{j,p}$ which are reflection and transmission coefficients to mode j if the input mode is mode p. It is to be noted that the modes in waveguide I and II are different, but the total number of modes for I and II is normally the same. Hence, the mode j and p in $R_{j,p}$ are in the same set of modes of waveguide I and those in $T_{j,p}$ are in different sets of modes. From the above equations, we obtain

$$\begin{aligned}\left\langle \vec{E}^{I}_{p,t}, \vec{H}^{I}_{i,t} \right\rangle + \sum_j R_{j,p} \left\langle \vec{E}^{I}_{j,t}, \vec{H}^{I}_{i,t} \right\rangle &= \sum_j T_{j,p} \left\langle \vec{E}^{II}_{j,t}, \vec{H}^{I}_{i,t} \right\rangle \\ \left\langle \vec{E}^{I}_{i,t}, \vec{H}^{I}_{p,t} \right\rangle - \sum_j R_{j,p} \left\langle \vec{E}^{I}_{i,t}, \vec{H}^{I}_{j,t} \right\rangle &= \sum_j T_{j,p} \left\langle \vec{E}^{I}_{i,t}, \vec{H}^{II}_{j,t} \right\rangle\end{aligned} \tag{2.17}$$

where the scalar product is defined as

$$\left\langle \vec{E}_{m,t}, \vec{H}_{n,t} \right\rangle = \iint_S \left(\vec{E}_{m,t} \times \vec{H}^{*}_{n,t} \right) \cdot \vec{u}_z dS \tag{2.18}$$

From the orthogonality relation Eq. (2.7), Eq. (2.17) is reduced to

$$\begin{aligned}\delta_{ip} \left\langle \vec{E}^{I}_{p,t}, \vec{H}^{I}_{p,t} \right\rangle + R_{i,p} \left\langle \vec{E}^{I}_{i,t}, \vec{H}^{I}_{i,t} \right\rangle &= \sum_j T_{j,p} \left\langle \vec{E}^{II}_{j,t}, \vec{H}^{I}_{i,t} \right\rangle \\ \delta_{ip} \left\langle \vec{E}^{I}_{p,t}, \vec{H}^{I}_{p,t} \right\rangle - R_{i,p} \left\langle \vec{E}^{I}_{i,t}, \vec{H}^{I}_{i,t} \right\rangle &= \sum_j T_{j,p} \left\langle \vec{E}^{I}_{i,t}, \vec{H}^{II}_{j,t} \right\rangle\end{aligned} \tag{2.19}$$

By adding and subtracting these equations, we get

$$\begin{aligned}\sum_j \left[\left\langle \vec{E}^{I}_{i,t}, \vec{H}^{II}_{j,t} \right\rangle + \left\langle \vec{E}^{II}_{j,t}, \vec{H}^{I}_{i,t} \right\rangle \right] T_{j,p} &= 2\delta_{ip} \left\langle \vec{E}^{I}_{p,t}, \vec{H}^{I}_{p,t} \right\rangle \\ R_{i,p} &= \frac{1}{2\left\langle \vec{E}^{I}_{i,t}, \vec{H}^{I}_{i,t} \right\rangle} \sum_j \left[\left\langle \vec{E}^{II}_{j,t}, \vec{H}^{I}_{i,t} \right\rangle - \left\langle \vec{E}^{I}_{i,t}, \vec{H}^{II}_{j,t} \right\rangle \right] T_{j,p}\end{aligned} \tag{2.20}$$

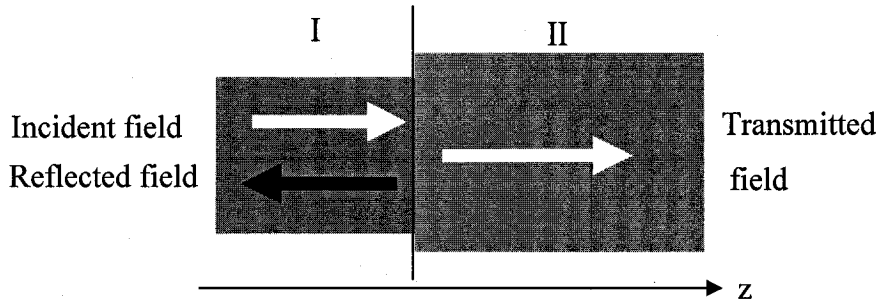

Figure 2.2. Interface between two layers.

Therefore, we can calculate the transmission and reflection matrices by solving an $N \times N$ linear system, where N is the number of total modes used in the expansion.

2.3.2 Scattering at a layered stack

After we calculate the reflection and transmission at each interface and the propagation within each layer, the task left is to calculate the reflection and transmission matrices of an entire stack, as shown in Fig. 2.3. There are two important methods to do this, the T-scheme (based on transfer matrices) and the S-scheme (based on scattering matrices) [6]. In this section, we will only present the T-scheme.

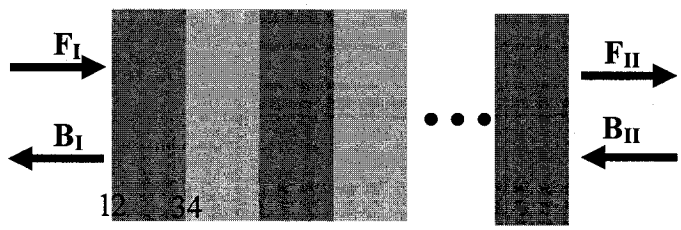

Figure 2.3. Scattering through a layered stack.

As we have seen in the previous section, there will be forward modes and backwards modes in each layer of a stack. Suppose those modes on the far side of a stack to those on the near side of the stack is related by the transfer matrices, we have

$$\begin{bmatrix} \mathbf{F}_{II} \\ \mathbf{B}_{II} \end{bmatrix} = \mathbf{T} \cdot \begin{bmatrix} \mathbf{F}_I \\ \mathbf{B}_I \end{bmatrix} \tag{2.21}$$

The transfer matrix $\mathbf{T}$ can be determined by the reflection and transmission matrices at all interfaces and the propagation matrices through all layers. To do so, we define the positions 1, 2, 3, 4…., as shown in Fig. 2.3. At interface, such as from 1 to 2, the transfer matrix is $\mathbf{I}_{12}$, and through layers, such as from 2 to 3, the transfer matrix is $\mathbf{P}_{23}$. We start from

$$\begin{aligned} \mathbf{F}_2 &= \mathbf{T}_{12} \cdot \mathbf{F}_1 + \mathbf{R}_{21} \cdot \mathbf{B}_2 \\ \mathbf{B}_1 &= \mathbf{R}_{12} \cdot \mathbf{F}_1 + \mathbf{T}_{21} \cdot \mathbf{B}_2 \end{aligned} \tag{2.22}$$

Rearranging the above equations can result in

$$\begin{bmatrix} \mathbf{F}_2 \\ \mathbf{B}_2 \end{bmatrix} = \begin{bmatrix} \mathbf{T}_{12} - \mathbf{R}_{21} \cdot \mathbf{T}_{21}^{-1} \cdot \mathbf{R}_{12} & \mathbf{R}_{21} \cdot \mathbf{T}_{21}^{-1} \\ -\mathbf{T}_{21}^{-1} \cdot \mathbf{R}_{12} & \mathbf{T}_{21}^{-1} \end{bmatrix} \cdot \begin{bmatrix} \mathbf{F}_1 \\ \mathbf{B}_1 \end{bmatrix} = \mathbf{I}_{12} \cdot \begin{bmatrix} \mathbf{F}_1 \\ \mathbf{B}_1 \end{bmatrix} \tag{2.23}$$

As the field propagates through the z-invariant layer from 2 to 3, it is easy to find

$$\begin{bmatrix} \mathbf{F}_3 \\ \mathbf{B}_3 \end{bmatrix} = \mathbf{P}_{23} \cdot \begin{bmatrix} \mathbf{F}_2 \\ \mathbf{B}_2 \end{bmatrix} = \begin{bmatrix} \mathrm{diag}(e^{-j\beta_i d_{23}}) & 0 \\ 0 & \mathrm{diag}(e^{j\beta_i d_{23}}) \end{bmatrix} \cdot \begin{bmatrix} \mathbf{F}_2 \\ \mathbf{B}_2 \end{bmatrix} \tag{2.24}$$

where β_i is the effective index in the layer from 2 to 3, and d_{23} is the thickness of that layer. The above equation can be readily found from Eq. (2.9). After calculating the $\mathbf{I}$ and $\mathbf{P}$ for the whole interfaces and layers from Eq. (2.23) and Eq. (2.24), we can find the transfer matrix for the whole stack is

$$\mathbf{T} = \mathbf{I}_{n-1,n} \cdot \mathbf{P}_{n-2,n-1} \cdot \ldots \cdot \mathbf{I}_{34} \cdot \mathbf{P}_{23} \cdot \mathbf{I}_{12} \tag{2.25}$$

By this way, we can calculate the strict field propagation in a whole structure. This is the so-called eigenmode expansion method.

2.4 Finite-difference time-domain analysis

Using Eq. (2.2) in Eq. (2.1) results in Eq. (2.3) which is the wave equation in frequency domain. Rather than doing that, the FDTD method is based on a direct simulation of the time-dependent Maxwell's curl equations, namely, Eq. (2.1). This method has become a powerful engineering tool for applications from radar-guided missiles, high-speed computer circuits, microwave devices to integrated and diffractive optical devices [7]. For optical devices, it has the ability to model the light propagation, scattering, diffraction, reflection and polarization effects. It can also simulate anisotropy

and dispersive materials. However, the method only allows for modeling very small-size devices, normally sub-micron for optical devices, since it is very time consuming. In this section, we will use a 2D TE example to outline the basic procedures of FDTD.

We assume that a 2D photonic device is laid out in the x-z plane, and the propagation is along z. The y-direction is assumed to be infinite. For the TE case in waveguides, only E_y, H_x, and H_z among the six field components of the electric and magnetic fields are nonzero [2]. Decomposition of Eq. (2.1) therefore leads to

$$\begin{aligned}
\frac{\partial E_y}{\partial t} &= \frac{1}{\varepsilon_0 n^2}\left(\frac{\partial H_x}{\partial z} - \frac{\partial H_z}{\partial x}\right), \\
\frac{\partial H_x}{\partial t} &= \frac{1}{\mu_0}\frac{\partial E_y}{\partial z}, \\
\frac{\partial H_z}{\partial t} &= -\frac{1}{\mu_0}\frac{\partial E_y}{\partial x}.
\end{aligned} \tag{2.26}$$

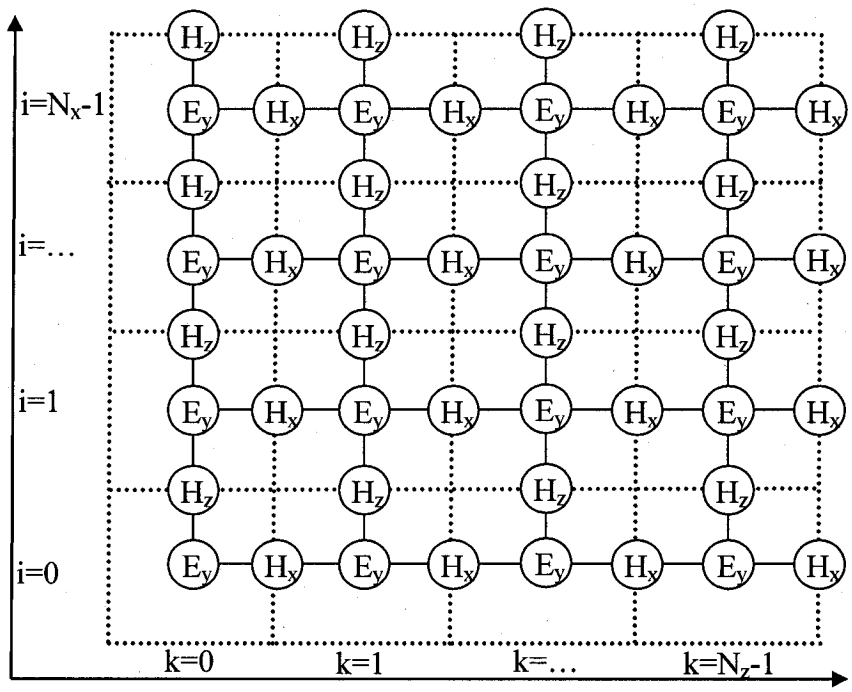

Figure 2.4. Discretization of the computational domain of the TE fields and the Yee algorithm.

The computation domain of the studied structure is discretized corresponding to the 2D mesh shown in Fig. 2.4. Each field component is represented by a 2D matrix, namely, $E_y(i,k)$, $H_x(i,k)$ and $H_z(i,k)$, where the indices i and k represent the number of space steps in the x and z direction, respectively. As illustrated in figure 2.4, the Yee algorithm [8] centers the E_y component so that every E_y is surrounded by four circulating $\vec{H}$ components, and every $\vec{H}$ component is surrounded by two E_y. Using central difference approximations for the numerical derivatives in space and time, Eq. (2.26) becomes

$$\frac{E_y^n(i,k)-E_y^{n-1}(i,k)}{\Delta t}=\frac{1}{\varepsilon_0 n^2(i,k)}\left(\frac{H_x^{n-\frac{1}{2}}\left(i,k+\frac{1}{2}\right)-H_x^{n-\frac{1}{2}}\left(i,k-\frac{1}{2}\right)}{\Delta z}-\frac{H_z^{n-\frac{1}{2}}\left(i+\frac{1}{2},k\right)-H_z^{n-\frac{1}{2}}\left(i-\frac{1}{2},k\right)}{\Delta x}\right)$$

$$\frac{H_x^{n+\frac{1}{2}}\left(i,k+\frac{1}{2}\right)-H_x^{n-\frac{1}{2}}\left(i,k+\frac{1}{2}\right)}{\Delta t}=\frac{1}{\mu_0}\frac{E_y^n(i,k+1)-E_y^n(i,k)}{\Delta z}$$

$$\frac{H_z^{n+\frac{1}{2}}\left(i+\frac{1}{2},k\right)-H_z^{n-\frac{1}{2}}\left(i+\frac{1}{2},k\right)}{\Delta t}=-\frac{1}{\mu_0}\frac{E_y^n(i+1,k)-E_y^n(i,k)}{\Delta x} \tag{2.27}$$

The superscript n labels the time step. By rearranging the above equations, one can calculate the fields at particular time and space if the initial conditions are given. One particularly important issue is the mesh size in space and the sampling in time. Typically, 10 to 20 steps per wavelength are needed, and the time step should follow the Courant limit [7]

$$\Delta t \le 1/\left(c\sqrt{1/(\Delta x)^2+1/(\Delta z)^2}\right) \tag{2.28}$$

2.5 Conclusions

In this chapter, we start from the Maxwell's equations and derive the equation to describe waveguide modes. The coupled-mode theory which is powerful to deal with directional couplers and grating structures is presented by a perturbation theory. We then discuss two strict electromagnetic theories which are suitable to simulate finite-size

photonic devices. All these three theoretical methods will be adopted to model or optimize the photonics structures in this thesis.

References

[1] Yariv, *Optical Electronics in Modern Communications*, (Oxford University Press, 1997).

[2] K. Okamoto, *Fundamentals of Optical Waveguide*, (Academic Press, 2000).

[3] T. Tamir, *Topics in applied physics, volume 7: integrated optics*, (Springer-Verlag Berlin Heidelberg New York, 1979).

[4] D. Marcuse, *Theory of dielectric optical waveguides*, (Academic Press, 1991).

[5] R. G. Hunsperger, *Integrated optics,* (Springer-Verlag Berlin Heidelberg New York, 2002).

[6] P. Bienstman, *Rigorous and efficient modeling of wavelength scale photonic components*, (PhD thesis, University Gent, 2001).

[7] A. Taflove, and S. C. Hagness, *Computational electrodynamics: the finite-difference time-domain method*, (Artech House, Boston, London, 2000).

[8] K. S. Yee, "Numerical solution of initial boundary value problems involving Maxwell's equations in isotropic media," *IEEE Trans. Antennas and Propagation*, vol. 14, pp. 302-307, 1996.

CHAPTER 3 SECOND-ORDER BRAGG WAVEGUIDE GRATING AS A 1D PHOTONIC BAND GAP STRUCTURE IN SOI WAVEGUIDE

In this chapter, the study of modal reflection, transmission and radiation properties of deeply etched second-order Bragg waveguide gratings in silicon-on-insulator (SOI) slab waveguide is presented. The eigenmode expansion method has been used to model this structure. High reflection can be obtained with a very short grating structure. The out-of-plane radiation efficiency can be controlled by the grating depth and groove width. This structure has potential for use in microcavity lasers, compact outcouplers and incouplers and surface-emitting lasers. We propose two application examples: one involves a double-grating coupler to realize efficient coupling between vertically integrated SOI waveguides over short distances, and the other is a photonic-bandgap microcavity.

3.1 Introduction

Photonic crystals (PC) [1]-[4] and photonic band gap structures are very promising building blocks for photonic components for a variety of applications. The PC components can be submicron scale which is comparable to that of electronic components. However, a three-dimensional PC working in the optical domain is still difficult to fabricate. Instead, two-dimensional PCs formed in a dielectric slab waveguide structure have attracted much interest in recent years [4]-[5]. The light is guided or confined by the PC structure in the horizontal plane and is confined by a classical dielectric waveguide in the vertical direction. One-dimensional PCs, which are essentially gratings or arrays of holes, are even simpler. It has been shown that such 1D PCs in classical dielectric waveguides can realize novel micro-optoelectronic devices [6]-[8], including light-emission devices, filters, outcouplers and incouplers. However, the full potential for this microstructure still needs to be explored; for example, while first-order and third-order deep gratings in semiconductor waveguides have been experimentally demonstrated, the analogous second-order deep grating has not been demonstrated. On

the other hand, the relatively weak second-order gratings [9]-[11] have found many applications in integrated optics. These include grating incouplers and outcouplers, codirectional and contradirectional waveguide couplers, fiber Bragg gratings, distributed feedback (DFB) or distributed Bragg reflector (DBR) laser structures. For the first- and third-order Bragg gratings, the diffracted components usually propagate in the plane of the guide, while the second-order grating can produce the radiation modes in the surface normal direction. Therefore, the second-order gratings have been used as the output coupling device for DBR lasers to produce surface-emitting devices. Another important application of the second-order grating is to realize coupling the light between a fiber and a passive waveguide [12], between a passive waveguide and an active component such as a laser, detector or modulator, and between two passive waveguides which will be the main content of the next chapter.

In this chapter, we study the modal reflection, transmission and radiation properties of deeply etched second-order Bragg waveguide gratings in a silicon-on-insulator (SOI) slab waveguide. Due to the high index contrast between silicon and silica, SOI is a promising material to make compact waveguides, and hence high-density photonic integrated circuits. Furthermore, SOI photonic devices can be mass produced using standard lithography and etching processes in silicon industry. In addition, SOI photonic circuits can be easily integrated with electrical circuits which are also fabricated on SOI wafers. All these advantages boosted the research in silicon photonics in recent years (for a good review, see Refs. [13]-[14] and references wherein). We apply the eigenmode expansion method to simulate this structure. It is shown that similar band gap behavior to the first-order grating can be found in the second-order deep grating structures. High reflectivity, high transmission and high our-of-plane radiation can be obtained depending on the grating parameters. The out-of-plane radiation efficiency can be controlled by the grating depth and groove width. This structure has potential for use in micro-cavity lasers, compact outcouplers and incouplers, and surface-emitting lasers. We propose an application example which involves a double-grating coupler to realize efficient coupling between vertically integrated SOI waveguides over short distances. In addition, a photonic-bandgap microcavity is demonstrated by using the second-order deeply etched gratings.

In Sec. 3.2, the simulation model and theoretical method are discussed. Sec. 3.3 presents the main simulation results of the second-order grating. The effects of the grating parameters on the reflectivity, transmission, and total loss will be discussed. In Sec. 3.4, we give two application examples, one is the double-grating coupler in stacked SOI waveguides, and the other is the photonic-bandgap microcavity. Finally, we draw some conclusions in Sec. 3.5.

3.2 Simulation model and theoretical method

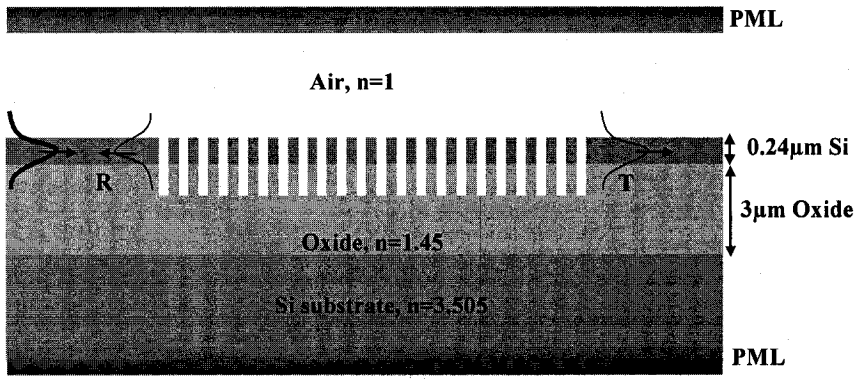

Figure 3.1. Cross-section of the waveguide layout and the deeply etched second-order grating modeled in this chapter (PML: perfectly matched layer).

Fig. 3.1 shows the waveguide and second-order grating modeled in this chapter. Here, the guiding layer of silicon has a thickness of 0.24μm, resulting in single-mode operation at wavelengths around 1.55μm. The oxide layer has a thickness of 3μm and the refractive index 1.45. The substrate silicon and the guiding layer silicon have the same refractive index 3.505, and the refractive index of the air superstrate is taken as 1. The grating is formed by etching out the guiding layer and some of the oxide layer. The duty cycle δ is defined as the ratio between the widths of the "groove" and the "tooth". The grating depth is defined as the groove etching depth, which varies from 0.08μm to 0.5μm. When the grating depth is larger than 0.24μm, the groove is etched through the guiding layer into the oxide. The parameters of the grating (grating period, duty cycle, and grating depth) are chosen so that the resonance of the second-order Bragg reflection is close to the

wavelength 1.55μm. The number of grating period is kept at 20, and the total length of the grating is in the region from 10μm to 15μm.

Since the grating is short and deep, a weak-grating analysis based on a perturbation approach would not be suitable. Furthermore, the leaky loss of the waveguide exists due to the high index of the substrate, and the grating radiation loss also occurs. Therefore, a rigorous electromagnetic analysis must therefore be used. The eigenmode expansion method (EEM) is a suitable approach since the whole structure can be divided into pieces each invariant in the z-direction when the grating grooves are rectangular. We use the CAMFR modeling framework [12][15][16] as the simulation platform of EEM. As discussed in Chapter 2, EEM starts out by slicing up the structure into layers whose index profile does not change in a given direction. The local eigenmodes of each layer are then found and a natural optical field profile propagating in this layer can be expanded in terms of these eigenmodes. The propagation through different layers can be determined by calculating the scattering matrix using mode matching at the interface. The CAMFR simulation tool is able to deal with both slab waveguides and circular symmetric structures. The boundary condition is based on the complex coordinate formulation of perfectly matched layers. The root-tracking method is used to find the local eigenmodes of each layer and the numerically stable S-matrix scheme is used to calculate the scattering matrices of the entire finite structure. This simulation tool has been successful used to simulated complex photonics structures, for example photonic crystal waveguides and VCSELs [12][15][16]. From the calculation of CAMFR, we verify that the 0.24μm core thickness results in single-mode operation and the effective refractive index is 2.925 for the TE mode at wavelength 1.55μm for the studied waveguide structure.

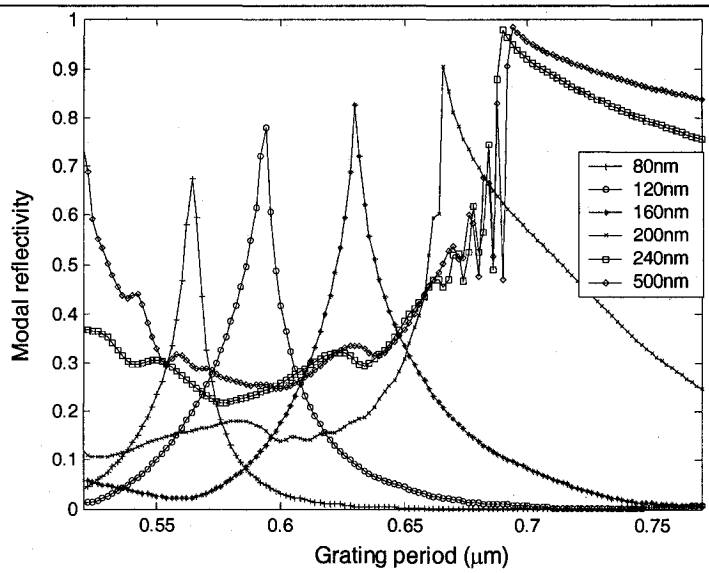

Figure 3.2. The modal reflectivity as a function of grating period for different grating depths. The wavelength is 1.55μm and the duty cycle is 0.5 for all curves.

3.3 Results and discussions

In this section, simulation results will be presented and discussed. The second-order grating is so called due to the fact that the second-order diffraction reflects the light back into contro-propagating mode. From the phase-matching condition, it is readily known that the first-order diffraction couples the light out of the waveguide at 90-degree, producing a surface-normal propagating field. Therefore, the second-order grating produces components in forward, backward and surface normal directions. From Eq. (1.5), the period of the grating Λ is equal to the wavelength in vacuum divided by the effective index in the grating region, namely,

$$\Lambda = \lambda / n_{eff}^{grating} \tag{3.1}$$

The effective index in the grating region $n_{eff}^{grating}$ can be approximated by:

$$n_{eff}^{grating} = n_{eff}^{groove} \times \delta + n_{eff}^{tooth} \times (1-\delta) \tag{3.2}$$

where n_{eff}^{groove} and n_{eff}^{tooth} are the effective indices in the groove and tooth regions respectively. However, the precise grating period for an expected resonance wavelength has to be calculated numerically. Fig. 3.2 shows the modal reflection as a function of

grating period for different grating depths. The duty cycle is kept at 0.5. The reflection curves show peaks when the resonance condition and 90-degree outcoupling are satisfied. The resonance periods increase as the grating depths become larger due to the fact that the effective index of the groove regions decreases with the increasing grating depths. Furthermore, the peak reflection increases and approaches to 100% with the increasing depths. The maximal reflection can be as high as 98% with the grating depth of 0.5μm. Oscillation behavior is found in the short-period edge when the grating depth is larger than the thickness of guiding layer (0.24μm). This oscillation may be caused by Fabry-Perot interference in a grating of finite length. When the grating depths become larger, the reflection by two grating ends increases. Therefore, with a larger grating depth, interference effects become more obvious.

Fig. 3.3 shows the spectral dependence of the modal reflectivity R, modal transmission T and total loss L which is defined as L=1-T-R. The loss includes the grating radiation loss, the diffractive spreading loss between the interfaces of grooves and teeth, and the leaky loss due to the high index of silicon substrate. In this figure, the grating periods used are those obtained from the resonance periods in Fig. 3.2. The grating depths are chosen as 0.12μm, 0.24μm and 0.5μm for Fig. 3.3(a), (b) and (c), respectively. It is shown that with these grating depths, the modal transmission is small in the spectral region from 0.95μm to 1.75μm. Since the transmission is low, the loss spectra are complementary with the reflection spectra. This is different from the first-order Bragg gratings, where the transmission and reflectivity spectra are usually complementary. The oscillations in the long wavelength side of the band gap are due to the Fabry-Perot interferences. This oscillation behavior is also exhibited in the first-order grating [8]. The short wavelength side of the band gap is not as sharp as the long wavelength side. However, some oscillation behavior can also be found in the short wavelength side with the grating depths 0.24μm and 0.5μm.

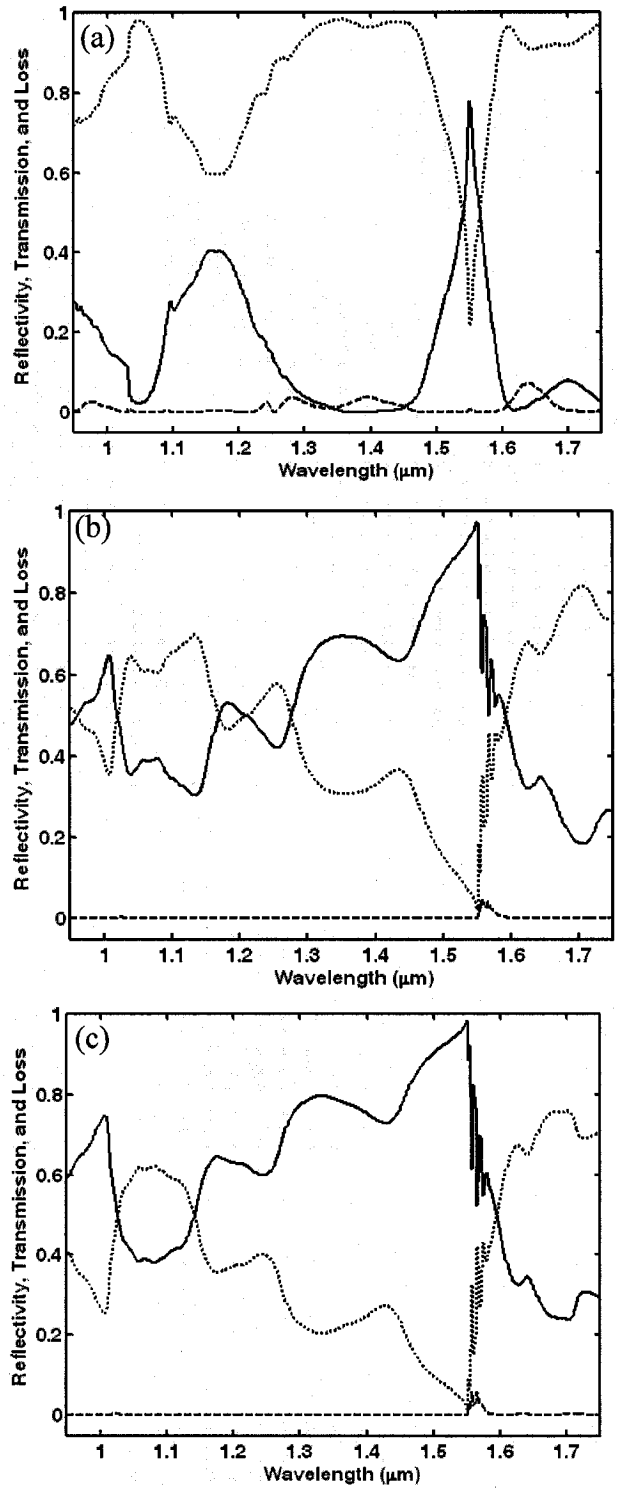

Figure 3.3. The spectral dependence of the modal reflectivity R (solid lines), modal transmission T (dashed lines) and total loss L (dotted lines). (a) The grating depth and the grating period are 120nm and 0.594μm,

respectively. (b) The grating depth and the grating period are 240nm and 0.69μm, respectively. (c) The grating depth and the grating period are 500nm and 0.694μm, respectively. The duty cycle is kept as 0.5 for all curves.

The duty cycle dramatically impacts the resonance periods and diffractive spreading loss which is due to the loss from the diffractive spreading of a beam profile in the groove regions. It has been shown that deep gratings with comparatively wide teeth and narrow grooves exhibit relatively low diffractive spreading losses inside the band gap in the first-order and third-order grating structures [7][8]. This is understandable since narrow grooves result in low diffractive spreading of a beam profile in the groove regions. In Fig. 3.4, the reflectivity as a function of grating period is shown for different duty cycles with the condition that the grating depth is kept at 0.5μm. The resonance period becomes shorter as the duty cycle becomes smaller. This phenomenon can be easily explained by Eq. (3.2). When the duty cycle is 0.1, the oscillation behavior is obvious at both period edges of the reflectivity band, while it is only obvious at the short period edge when duty cycles are 0.3 and 0.5. Furthermore, the reflectivity peak drops when the duty cycle changes from 0.1 to 0.5. This confirms that the diffractive spreading loss increases when the duty cycle is larger. However, this drop is very small (around 2%), which demonstrates that the diffractive spreading loss has only a small fraction in the total loss. It is the radiation loss which dominates the total loss.

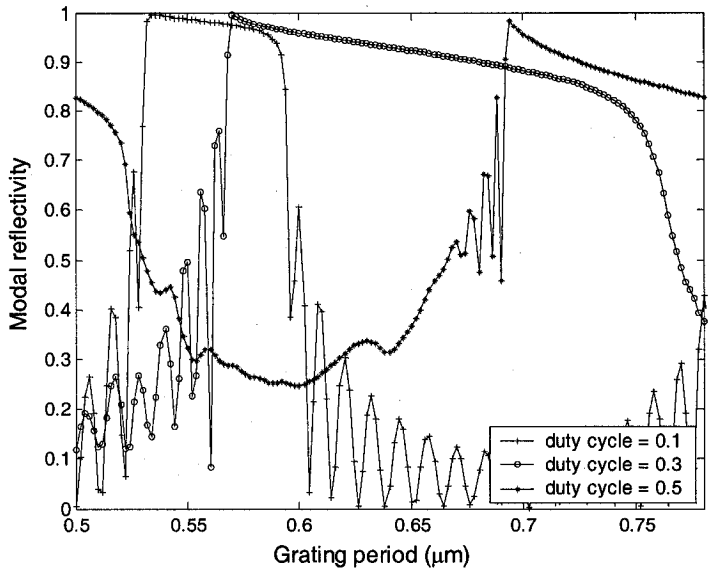

Figure 3.4. The modal reflectivity as a function of grating period for different duty cycles. The wavelength is 1.55μm and the grating depth is 0.5μm.

The graphs in Fig. 3.5 represent the spectral dependence of the modal reflectivity, modal transmission, and total loss for different duty cycles. The duty cycles are taken as 0.1, 0.3, and 0.5. When it is larger than 0.5, the spectral properties are similar to those of 0.5, therefore we do not show any results for the duty cycle larger than 0.5. Fig. 3.5(a) demonstrates that the width of the band gap increases for the larger duty cycles. As the duty cycle is taken as 0.3 and 0.5, the short-wavelength edge is not obvious but has a slow oscillation behavior. The transmission spectra in Fig. 3.5(b) verify that with smaller duty cycle, the transmission is higher. This is due to two factors: (1) as the grooves become narrower, the diffractive spreading loss becomes smaller; and (2) the radiation efficiency of the grating is usually maximal when the duty cycle is close to or equals to 0.5 [11], which makes the transmission larger when the duty cycle is 0.1. The curves in Fig. 3.5 also show that when the duty cycle is 0.1, the transmission T and the reflectivity R curves are complementary, whereas when the duty cycle is larger than 0.3, the loss L and the reflectivity R are complementary.

With all the above simulation results, we may draw some conclusions for the second-order deeply etched gratings. It is seen that the behavior of the second-order deeply grating can be quite similar to those of the first-order grating, but the period is 2 times that of the first-order grating. The maximal reflectivity can approach 100% even though the duty cycle is 0.5. The duty cycle has very dramatic impact on the behavior of the grating. When it is small, the properties of the grating are more similar to the first-order gratings. The total loss can be reduced by reducing the duty cycle. On the other hand, the radiation efficiency can be increased by choosing larger duty cycle in the applications of outcoupler and surface-emitting devices.

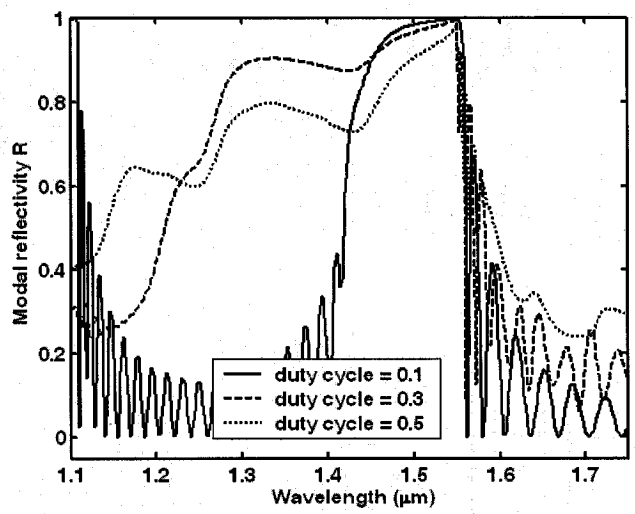

(a)

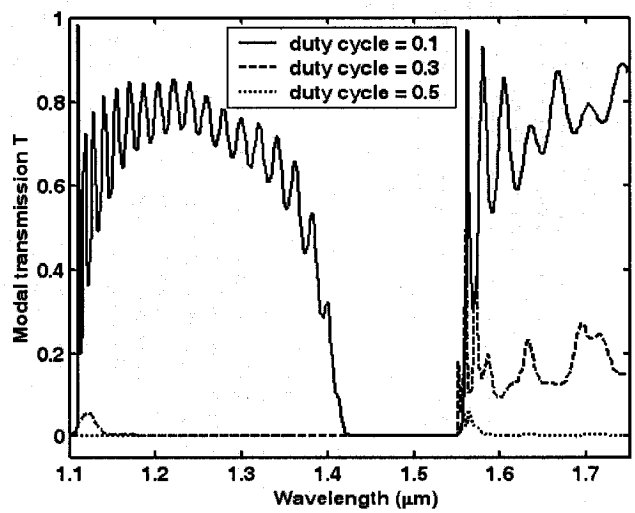

(b)

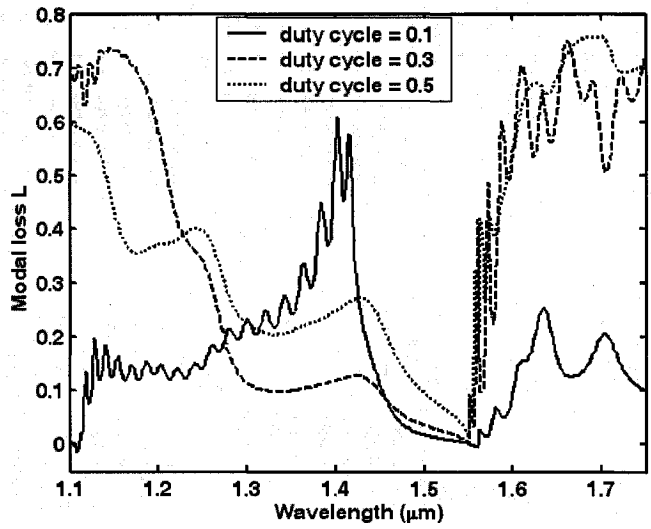

Figure 3.5. The spectral dependence of the modal reflectivity R (a), modal transmission T (b) and total loss L (c). To keep the resonance frequencies as 1.55μm for all duty cycles, the grating periods are 0.534μm for solid lines, 0.57μm for dashed lines, and 0.694μm for dotted lines. The grating depth is 500nm for all curves.

3.4 Application examples

In this thesis, we present two possible application examples by using the second-order deeply etched grating structure in SOI waveguides. The first example involves the double-grating coupler between the vertically stacked SOI waveguides, which will be the subject of next Chapter. The second example is similar to the report on photonic-bandgap microcavity in Ref. [6], but here we show a microcavity formed by the second-order gratings.

Fig. 3.6 demonstrates a possible photonic-bandgap microcavity. The gratings are the second-order deep gratings similar to the previous section. A defect is introduced in the middle of the second-order grating. The defect length is defined by the distance between those two dislocated grooves, as shown in Fig. 3.6. This is a similar microcavity structure as studied in Ref. [6] except that we use second-order grating structure. The physics behind this microcavity is anologous to a defect or impurity state in a semiconductor that

forms a level within the semicondutor band gap. A defect in PBG material leads to a defect state which can perform as a resonator or filter.

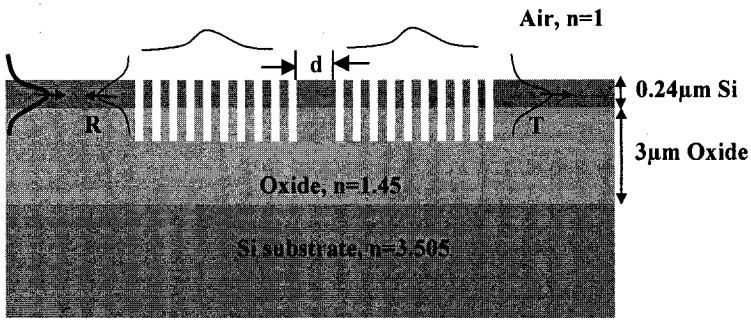

Figure 3.6. Cross-sectional diagram of a photonic-bandgap microcavity by using second-order deep gratings.

A resonance in transmission can occur in the band gap due to the presence of the defect. The resonance wavelength depends on the length of the defect: when the defect length increases, the resonance wavelength shifts to longer values. This conclusion is consistent to that reported in Ref. [6] and can be understood by considering the cavity as a Fabry-Perot resonator. Another phenomenon is also possible: if the grating parameters are chosen properly, the total loss can also be very large at the transmission resonance. This is due to the fact that at the transmission resonance, the light can penetrate to the defect regions, whereas the light is reflected back very quickly at the non-resonance regions. In some situations, the total loss can be even larger than the transmission at resonance. It is to be noted that the total loss includes mainly the radiation loss and the diffractive spreading loss, but the radiation loss may dominate the total loss. In the applications of laser and outcoupler, the radiation loss is very useful. To our knowledge, this kind of microcavity with large radiation efficiency has not been reported in the past. It may be very useful in the surface-emitting devices and 90-degree out-of-plane couplers and filters.

3.5 Conclusions

In this chapter, we have studied the second-order deeply etching grating in SOI waveguide. It is shown that band-gap behavior exists, similar to the first-order grating.

The effects of the grating parameters on the spectra are discussed in detail. The main advantages of this kind of grating are twofold: (1) the period is two times that of the first-order grating, which can relax some fabrication difficulties; and (2) the out-coupling of the second-order grating can be very useful in compact incouplers and outcouplers, and surface-emitting devices. Based on the studied grating structures, we propose two application examples. The first implements the gratings as compact incouplers and outcouplers, and realizes the coupling between two passive waveguides. The second application involves a bandgap microcavity which can find applications in microlasers, filters and signal routers.

References

[1] E. Yablonovitch, "Photonic band-gap structures," *J. Opt. Soc. Am. B,* vol. 10, pp. 283-295, 1993.

[2] J. D. Joannopoulos, R. D. Meade, and J. N. Winn, *Photonic Crystals*, (Princeton, New York, 1995).

[3] C. M. Soukoulis, *Photonic Band Gap Materials*, (Kluwer, Dordrecht, 1996).

[4] T. Kraus, R. De La Rue, and S. Band, "Two-dimensional photonic bandgap structures operating at near-infrared wavelengths," *Nature*, vol. 383, pp. 699-702, 1996.

[5] S. Fan, J. N. Winn, A. Devenyi, J. C. Chen, R. D. Meade, and J. D. Joannopoulos, "Guided and defect modes in periodic dielectric waveguides," *J. Opt. Soc. Am. B,* vol. 12, pp. 1267-1272, 1995.

[6] J. S. Foresi, P. R. Villeneuve, J. Ferrera, E. R. Thoen, G. Steinmeyer, S. Fan, J. D. Joannopoulos, L. C. Kimerling, Henry I. Smith, and E. P. Ippen, "Photonic-bandgap microcavities in optical waveguides," *Nature*, vol. 390, pp. 143-145, Nov. 1997.

[7] T. F. Krauss and R. M. De La Rue, "Optical characterization of waveguide based photonic microstructures," *Appl. Phys. Lett.,* vol. 68, pp. 1613-1616, Mar. 1996.

[8] J. Ctyroky, S. Helfert, R. Pregla, P. Bienstman, R. Baets, R. Deridder, R. Stoffer, G. Klaasse, J. Petracek, P. Lalanne, J. –P. Hugonin and R. M. Delarue, "Bragg waveguide grating as a 1D photonic band gap structure: COST 268 modelling task," *Opt. and Quantum Electron.*, vol. 34, pp. 455-470, 2002.

[9] W. Streifer, D. R. Scifres, and R. Burnham, "Analysis of grating-coupled radiation in GaAs:GaAlAs lasers and waveguides," *IEEE J. Quantum Electron.*, vol. QE-12, pp. 422-428, July 1976.

[10] A. Hardy, D. F. Welch, and W. Streifer, "Analysis of second-order gratings," *IEEE J. Quantum Electron.*, vol. QE-25, pp. 2096-2105, Oct. 1989.

[11] G. W. Taylor and C. Kwan, "Determination of diffraction efficiency for a second-order corrugated waveguide," *IEEE J. Quantum Electron.*, vol. 33, pp. 176-186, Feb. 1997.

[12] D. Taillaert, W. Bogaerts, P. Bienstman, T. F. Krauss, P. V. Daele, I. Moerman, S. V.erstuyft, K. D. Mesel and R. Baets, "An out-of-plane grating coupler for efficient butt-coupling between compact planar waveguides and single-mode fibers," *IEEE J. Quantum Electron.*, vol. 38, pp. 949-955, July 2002.

[13] G. T. Reed, and A. P. Knights, *Silicon photonics*, (John Wiley & Sons Inc., 2004).

[14] B. Jalali, S. Yegnanarayanan, T. Yoon, T. Yoshimoto, I. Rendina, and F. Coppinger, "Advances in silicon-on-insulator optoelectronics," *IEEE J. Selected Topics Quantum Electron,* vol. 4, pp. 938-947, 1998.

[15] P. Bienstman and R. Baets, "Optical modeling of photonic crystals and VCSEL's using eigenmode expansion and perfectly matched layers," *Opt. Quantum Electron.*, vol. 33, pp. 327-341, Apr. 2001.

[16] P. Bienstman, *Rigorous and efficient modeling of wavelength scale photonic components*, (PhD thesis, University Gent, 2001).

CHAPTER 4 COMPACT DOUBLE-GRATING COUPLER BETWEEN VERTICALLY STACKED SILICON-ON-INSULATOR WAVEGUIDES

In this chapter, we analyze a compact double-grating coupler which provides coupling through radiation modes between two vertically stacked silicon-on-insulator waveguides. The grating is sufficiently strong to be considered as a one-dimensional photonic bandgap structure which facilitates a very short coupling length. Simulations suggest that a coupling efficiency of 29% is achievable in coupling the light from one waveguide to another with 12.9μm long binary gratings. We find that the coupling efficiency is enhanced by Fabry-Perot resonance between two gratings. The coupling efficiency can be increased by using a blazed grating. We use the eigenmode expansion method to design and optimize the binary grating coupler and the results are verified by using the finite-difference time-domain method.

4.1 Introduction

As we have discussed in Chapter 1, one promising approach for optical integration is that of vertical integration whereby active and passive waveguides are stacked on a single substrate, resulting in a 3-D photonic circuit. The stacked configuration is also important in assisting in a flexible layout of photonic circuits. There have been a number of reports of stacked waveguides consisting of semiconductors, polymers, or dielectric materials [1]-[6]. The use of high-index-difference waveguides is another important method to increase the density of optical circuits due to their small size, high confinement and small bending radius [7]. Very compact waveguides can be fabricated in silicon-on-insulator (SOI) wafers due to large index difference between silicon and silicon oxide. One example of a promising single-mode ridge SOI waveguide is given in reference [7]. An important advantage of SOI waveguides is their ease of integration with electronic circuits based on silicon wafers. In particular, a small-size, highly efficient coupler for vertical integration is required for dense integration of photonic circuits. As discussed in

Chapter 1, a double-grating coupler utilizing gratings to transfer guided power in one waveguide to the other through radiation modes is very promising in these applications [8]-[10]. To our knowledge, only a few reports [8]-[10] investigated such coupling configuration mainly due to the fact that the high radiation loss to substrates makes the coupling efficiency low. However, this coupling scheme has the advantage of applicability to a planar multi-layer structure and no requirement on the minimum distance between two waveguides (i.e., the overlap between guided modes is not required). To date the potential of this kind of coupler is still not fully exploited. This is in part due to the challenge in accurate and efficient simulation of this configuration. In Refs. [8]-[9], a modified coupled-mode theory was employed. A coupling coefficient between the two guided modes in the coupled waveguides was introduced to describe the outcoupling and incoupling processes as one single coupling process. Detailed insight into the coupling mechanisms cannot be obtained since this theory does not deal with the direct interaction between the guided modes and the radiation modes. In Ref. [10], the finite-difference time-domain (FDTD) method was applied to a conducting grating structure. However, this method suffers from slow computation and is only applicable to very short grating structures. Meanwhile, theoretical methods which treat outcoupling and incoupling independently will be less accurate since each grating will couple out and couple in simultaneously. Therefore, it is necessary to find an appropriate and accurate model which considers the double-grating structure as a single compound system and which can handle relatively long grating structures. Moreover, as two gratings have different periods, the whole structure may not exhibit periodicity, which makes Bloch theory inapplicable.

In this chapter, we analyze a compact double-grating coupler structure which realizes coupling between two stacked high-index-difference SOI waveguides. Although we restrict the current study to two passive waveguides, the extension to the coupling of a passive waveguide and an active waveguide is possible. The grating structure is similar to those structures proposed in Refs. [8]-[10]. However, here the waveguides are high-index-difference waveguides and the gratings are strong dielectric gratings. More importantly, the number of periods is small (approximately 20) and thus a very compact coupler structure is realized. Initially, this structure appears to be similar to those in Refs.

[8]-[10]. However, detailed analysis finds that Fabry-Perot resonance of radiation modes between two gratings is the main reason for high coupling efficiency. Moreover, we will show that the eigenmode expansion method (EEM) is well-suited to simulate and design this kind of structure. This strict electromagnetic method not only considers the two-grating structure as a single compound system, but also is capable of handling relatively long grating structures. The short computation time permits optimization of the double-grating coupler. Therefore, we not only propose a new kind of compact coupler to realize coupling between two high-index-difference waveguides with large separation by using strong dielectric gratings, but also demonstrate a suitable analytical technique for the optimization of these complex structures.

The outline of this chapter is as follows: In Section 4.2 we describe the proposed grating coupler and discuss modeling technique. In Section 4.3, we apply EEM to design the grating coupler and we demonstrate the dependence of the coupling efficiency on the grating parameters. The coupling mechanism will be also discussed. Section 4.4 contains numerical results from the method of FDTD on the final design from Section 4.3. Possible applications are discussed in Section 4.5 and final conclusions are also drawn.

4.2 Simulation model

Fig. 4.1 shows the waveguides and double-grating structure modeled in this chapter. Here, two guiding layers of silicon have thicknesses of 0.23μm and 0.25μm, respectively. These thicknesses result in single-mode operation at wavelength 1.55μm. Different thicknesses are chosen to confirm that this kind of coupler can be used to interface dissimilar waveguides. The separation layer between the guiding layers has a refractive index of 1.5, which is selected as a typical index for a chemical bonding material. The thickness of this separating layer, namely the separation between two guiding layers, is 5μm, which is about 5 times the wavelength and large enough to ensure zero field-overlap between two guiding modes. The thicknesses of the silicon oxide layers between the silicon guiding layers and the silicon substrates are initially chosen to be 1μm and the refractive index is 1.45. The optimum value of oxide thickness will be determined later on. The effective refractive indices are 2.930 and 2.986 for the TE modes in the lower and the upper guiding layers respectively. The whole structure can be experimentally realized

by flipping over one of two SOI waveguides and bonding these two waveguides together face to face.

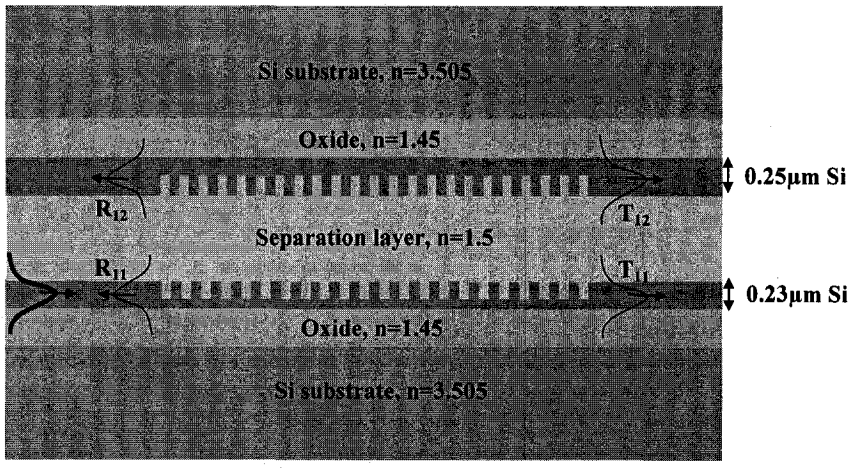

Figure 4.1. Cross-sectional diagram of the double-grating coupler and SOI waveguides modeled here.

Since both gratings are short and deep, a weak-grating analysis based on a perturbation approach may not be suitable. Furthermore, since the coupling is realized through radiation modes, it is very important to consider the two gratings as an integrated system. A rigorous electromagnetic analysis must therefore be used. The method of FDTD is a powerful tool to simulate finite sized photonic structures. However, it is computationally demanding which makes it unsuitable to determine the optimum values of the grating periods, the grating depths and the thicknesses of oxide layers. EEM is a more suitable alternative approach since the whole structure can be divided into sections, each invariant in the z-direction. Again, we use the CAMFR modeling framework [11]-[13] as the simulation platform of EEM and employ FDTD to confirm the results once the final design has been obtained.

Fig. 4.2 shows the way in which the double-grating structure is sliced for analysis via CAMFR. This slicing process can be used on double-grating structures with different grating periods, duty cycles and grating depths, but does require rectangular grating grooves. The slicing begins from the first grating edge (it does not matter if the grating edge belongs to the upper grating or lower grating). A new slice is produced once a new

grating edge is met. The thickness of the slice is calculated from the former edge to the new edge. This is straightforward process but as the periods for the two gratings are different, numeric precision must be increased since the thickness of some slices may be quite small. Under the condition that the grating grooves are rectangular, only four possible index profiles of the slab waveguide occur for the slices and they are shown in Figs. 4.2(b)-(d). The eigenmodes of these four structures are thus found and the scattering matrix can be computed based on these eigenmodes. At last, the propagation of an incident TE mode can be calculated. The guiding modes in the upper and lower silicon guiding layers become two guiding modes of the slab compound waveguide having the index profile of Fig. 4.2(b). It is to be noted that now we regard the system as one compound waveguide rather than two waveguides. Because the distance between the two silicon guiding layers is large, the guiding modes of the compound waveguide represent accurately the modes of two silicon subwaveguides. To calculate the reflection and transmission from the lower guiding layer to the upper guiding layer, one just needs to calculate the scattering matrix through the whole structure. The matrix elements provide all the necessary information to obtain the reflection and transmission coefficients.

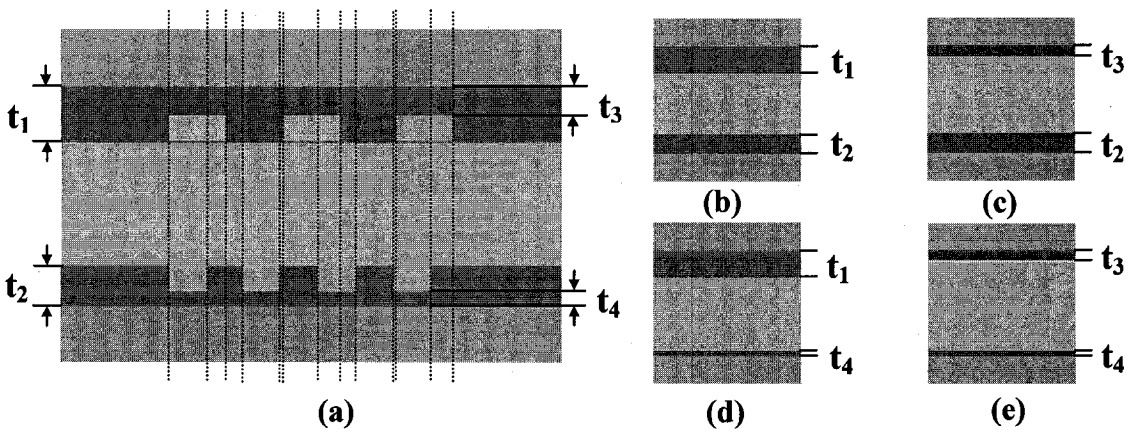

Figure 4.2. (a) Slicing up the double-grating structure into sections which are invariant in the z-direction (direction of propagation). (b)-(d) Possible slab compound waveguide structures in the calculation. In (b)-(d), t_i is the thickness of silicon guiding layer.

In order to test the validity of the proposed slicing technique, we simulated the double-grating structure shown in Fig. 4.1 with different grating periods but setting one grating

depth to be zero. Since only one grating is present in this case, we can also use the previously validated slicing technique for periodic structures [11]-[13] in CAMFR. Simulation results from both techniques agree very well. We thus conclude that our proposed slicing technique can be employed to simulate the double-grating structure.

4.3 Design of waveguide coupler from EEM

In this section, we present the optimization of the grating coupler. We define T_{12} to represent the forward transmission from the lower guiding layer to the upper guiding layer and we optimize this coupling efficiency. Further, as shown in Fig. 4.1, we define the reflectivity from the lower guiding layer to the upper guiding layer as R_{12}, the reflectivity within the lower guiding layer as R_{11}, the transmission within the lower guiding layer as T_{11}, and the total radiation loss as $1-R_{11}-R_{12}-T_{11}-T_{12}$. The total radiation loss consists of the radiated light that is coupled upwards and downwards into substrates and scattered at the interfaces. The basic procedure to design such a waveguide coupler is as follows: we first fix a value of the grating depth, and then vary the values of the grating periods to obtain the optimal value for the grating periods. We then change the value of grating depth and follow the same above procedure to find the optimal grating periods corresponding to the new grating depth. By this way, we obtain the optimal value of grating depth and corresponding optimal grating periods. The optimum values of other parameters, such as oxide thicknesses and separation thickness can then be obtained.

We first consider the effect of grating depth on the optimal coupling efficiency and optimal periods of two gratings. It is expected that with different grating depths, the optimal periods which result in the largest coupling efficiency of T_{12} are different since the effective refractive indices within the grating regions vary with the grating depth. This leads to a more complicated procedure to obtain the optimal design of such a double-grating coupler. In order to reduce some of the complexity we keep the two grating depths the same in our simulation model. This is reasonable due to the fact that two guiding layers have similar thicknesses. Fig. 4.3 shows the optimum grating period as a function of grating depth assuming a grating duty cycle of 0.5 and with equal grating lengths (20 periods of the lower grating). The resultant coupling efficiency T_{12} is shown in Fig. 4.4 together with R_{12}, R_{11}, T_{11} and the total radiation loss. Fig. 4.3 demonstrates that as the

grating depth increases, both optimal grating periods become larger. This is to be expected since the effective refractive indices in the grating regions become smaller with increasing the grating depth. It is to be noted that these optimal grating periods result in an outcoupling and incoupling direction that is slightly off 90-degrees. This will be addressed in more detail later. Fig. 4.4 demonstrates that the optimum coupling efficiency first increases with the larger grating depth, then decreases. The maximum coupling efficiency T_{12} occurs for a grating depth of 0.13μm. The transmission T_{11} is high in the very shallow grating region since in this region the incident wave enters the grating and exponentially decays with a constant which is proportional to the square of the grating height [14]. As the grating depth increases, the transmission T_{11} decreases and the total radiation loss increases significantly. The optimal grating periods are 0.645μm and 0.62μm for the lower grating and the upper grating respectively. The grating length is 12.9μm for both gratings. The curves in these two figures are not perfectly smooth because different sets of parameters (grating depths, grating periods and grating length) are used for each point in these curves.

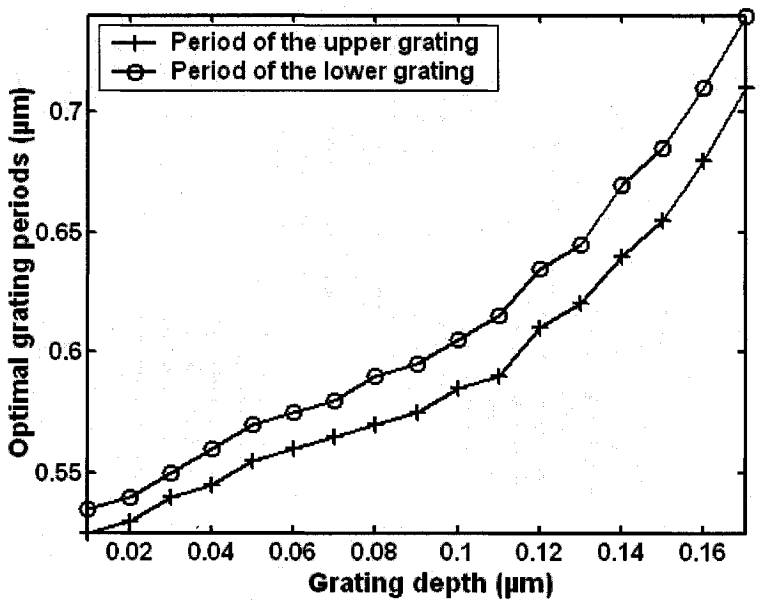

Figure 4.3. Optimum grating periods for transmission of T_{12} versus the grating depth. Both thicknesses of the oxide layers are fixed at 1μm and both duty cycles of the gratings are 0.5.

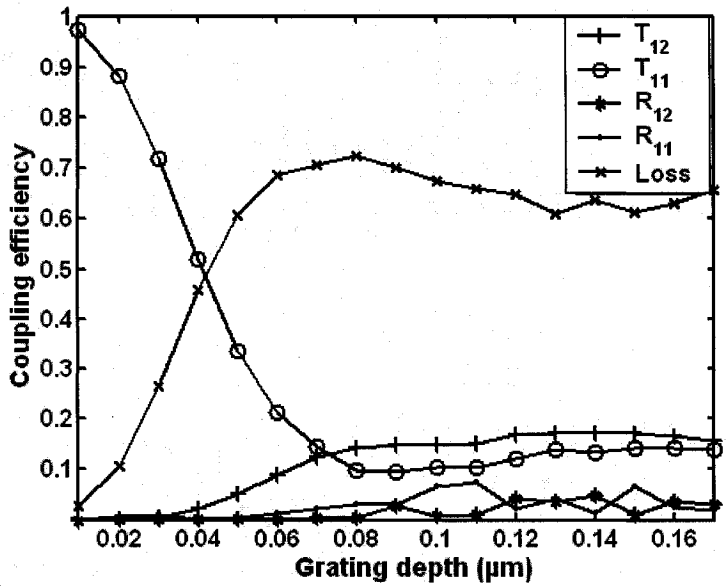

Figure 4.4. Coupling efficiency versus the grating depth, assuming optimal grating periods.

The oxide thickness has an impact on the power ratio between the upwards and downwards radiated light. When the appropriate thickness is chosen, the reflected light from the interface of the oxide and silicon substrate will add constructively to the radiated light in the separation region. This can increase the coupling efficiency T_{12}. We find that the optimal oxide thicknesses closest to 1μm are 1.25μm and 1.21μm for the lower oxide layer and the upper oxide layer, respectively. We obtain a maximum value of T_{12} of 25% with these thicknesses of oxide layers. The small difference in thickness between the two oxide layers (1.25μm and 1.21μm) is caused by the difference of the two grating periods. In Figs. 4.5 and 4.6, we show the dependence of the coupling efficiency on the thicknesses of oxide layers. Periodic behavior is seen and the period is approximately half a wavelength in the oxide layer. This value of the period confirms that this behavior is induced by interference between the direct radiation wave and the reflection at the oxide/substrate interface.

With the above optimized parameters, we study the coupling efficiency in a spectral range from 1.52μm to 1.68μm. The thicknesses for both oxide layers are kept at 1.25μm and 1.21μm, and the separation layer is still 5μm thick. Material dispersion is neglected.

In Fig. 4.7, the spectra for transmission, reflectivity and loss are given with the above optimized parameters. In order to easily analyze the spectra, in Fig. 4.8 we present the

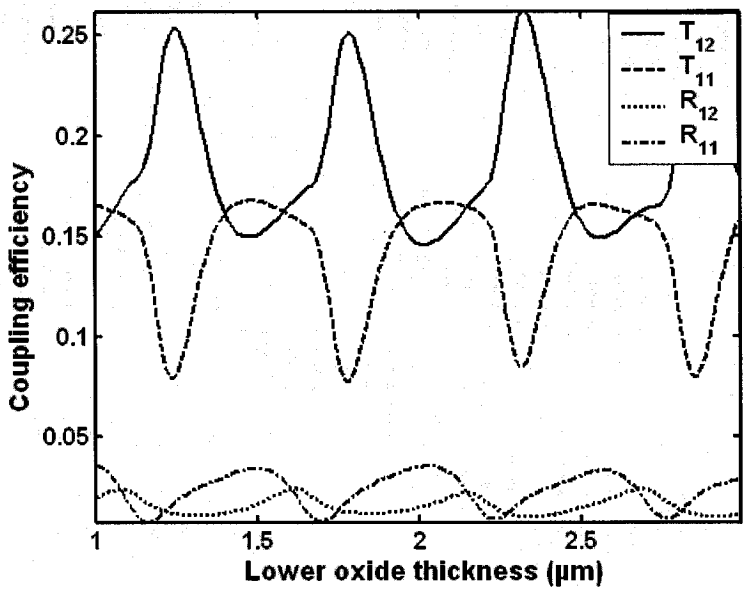

Figure 4.5. Coupling efficiency versus the thickness of the lower oxide layer. The thickness of the upper oxide is 1.21μm.

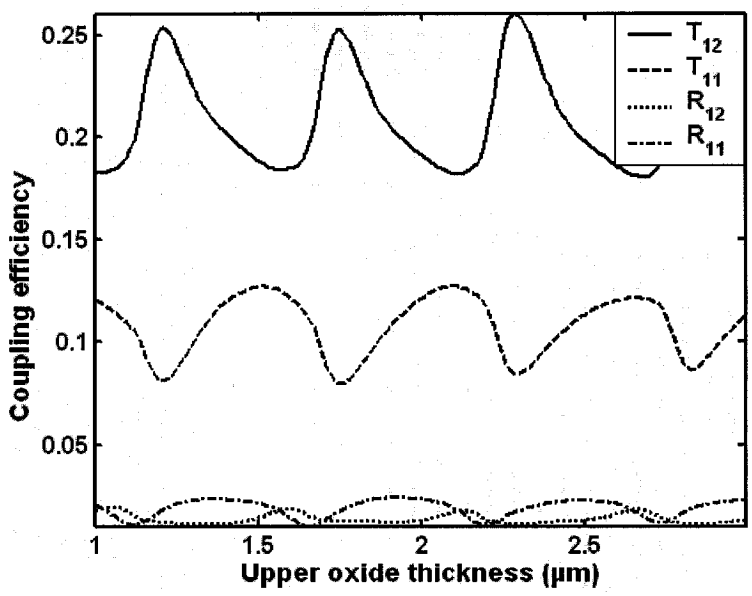

Figure 4.6. Coupling efficiency versus the thickness of the upper oxide layer. The thickness of the lower oxide is 1.25μm.

spectra for R_{11}, T_{11} and loss for a system without the upper grating but with all other parameters as in Fig. 4.7. We first analyze the reflectivity R_{11} in Fig. 4.8. It is seen that the reflection spectrum is that of a second-order Bragg reflector with the central wavelength at around 1.63μm. It is somewhat surprising that even a second-order grating with a duty cycle of 0.5 displays a reflectivity of 55% with low loss. The high reflectivity may result from two reasons. Because of the high index difference, high reflectivity occurs at the grating teeth interface, especially in the deep grating structure. Further, the coupling between the radiation field with the backwards guiding mode may induce high reflectivity [15][16]. When the transmission of T_{11} is considered, the whole spectrum is similar to the spectrum obtained in Ref. [8], where the deep first-order Bragg grating was investigated by several groups using different but strict electromagnetic theories. It is thus expected that the second band gap gives similar behavior to the first band gap if we consider the deep second-order grating as a 1D photonic crystal structure. Furthermore, the spectra we obtained are also similar to the spectra obtained in Ref. [12], in which a second-order grating is used for butt-coupling between a planar waveguide and a single-mode fiber. Now we compare the spectra in Fig. 4.8 with those in Fig. 4.7. It is seen that R_{11} and T_{11} spectra are identical above the wavelength of 1.58μm. This is due to the fact that in this wavelength region, the period of the upper grating is not matched to the radiation modes outcoupled by the lower grating. Therefore, there is no guided power coupled into the upper guiding layer. Thus, the presence of the upper grating will not affect the transmission T_{11} and the reflectivity R_{11}. The main difference occurs at around 1.55μm wavelength. Around this wavelength, T_{11} becomes larger than the case without the upper grating. At the same time, the coupling efficiency T_{12} increases. The reflectivity R_{11} is not greatly influenced by the presence of the upper grating.

We can now further investigate the coupling mechanisms at the wavelength of 1.55μm. Since the resonance wavelength of the lower grating is not 1.55μm, the period of the lower grating is not a perfect second-order grating for 1.55μm, but with a positive detuning $\Delta = 2\pi n_{eff}/\lambda - 2\pi/\Lambda$ where Λ represents the period of the lower grating and n_{eff} is the effective index within the grating region in the lower guiding layer. It is thus expected that in the beginning of the lower grating, the radiation is coupled into both the

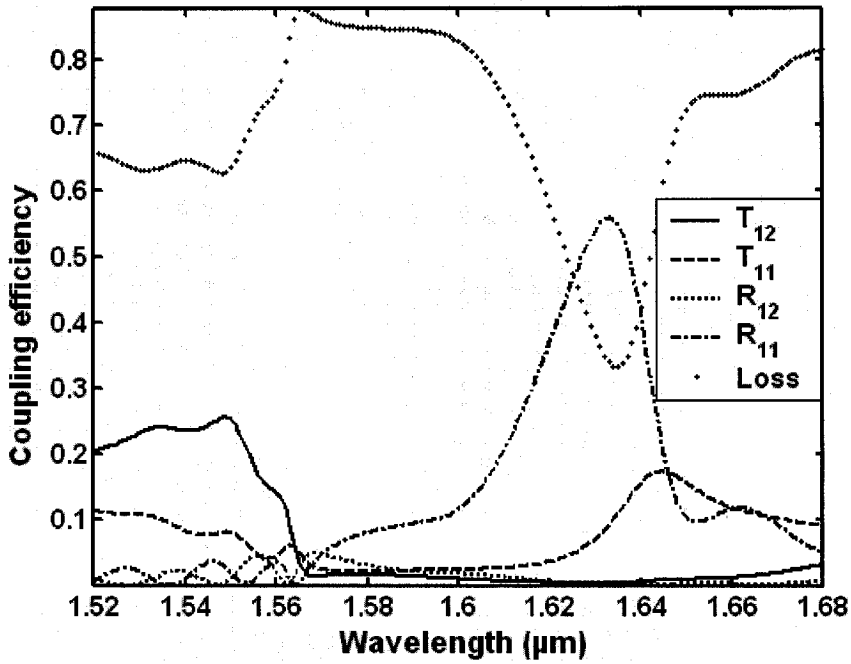

Figure 4.7. The spectral dependence of the coupling efficiency with the optimized parameters.

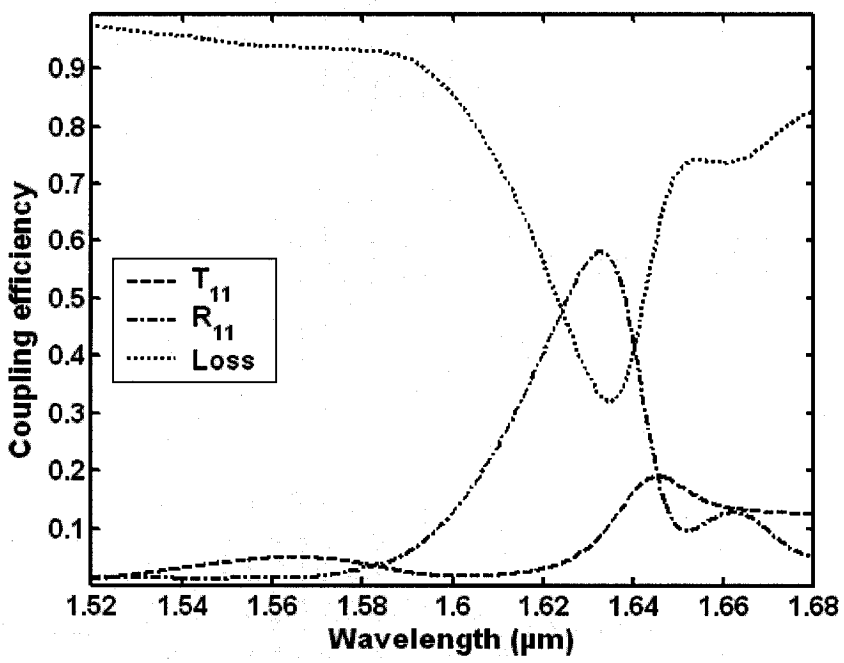

Figure 4.8. The spectral dependence of the coupling efficiency with the optimized parameters but without the upper grating.

separation region and the substrate region with an angle not equal to 90 degrees. The radiation angle from the first grating into the separation layer is $\theta = \cos^{-1}(\Delta/(2\pi/\lambda_s))$ where λ_s is the wavelength in the separation layer. Here, the angle is measured from the waveguide direction. Meanwhile the period of the upper grating satisfies the matching condition that it resonantly couples the radiation field with the angle θ into the forward guided mode in the upper guiding layer. The radiated light in the separation region is then coupled into the upper guiding layer and will propagate through the upper grating region. Some of the guided light in the upper guiding layer will subsequently radiate back out towards the separation region and will then return to the lower grating region, where it can be coupled back into the lower guiding layer by the lower grating. This multiple coupling suggests that a vertical Fabry-Perot (FP) resonance between the two grating regions will occur when the grating period is suitable. The FP resonance condition is $d = d_{0+}\frac{m\lambda_s}{2}$ where d is the thickness of the separation layer, m is a positive integer, d_0 is a constant because of the phase shift at the grating interface. The FP resonance enhances the coupling efficiency of both T_{11} and T_{12} in our structure. To the best of our knowledge, this effect has not been reported for previous grating couplers. Fig. 4.9 shows the coupling efficiency versus the separation distance simulated by EEM where the resonance effect is clearly observed. The spacing between two maxima of T_{11} or T_{12} is exactly $\lambda_s/2$.

The above simulation assumes that the two gratings start from the same axial position, however in reality there may be an offset between them. One interesting finding is that the optimal offset is actually not 0μm (as simulated above) but is 4μm and the coupling efficiency of T_{12} with this offset is about 29%. This is due to the effect that with this offset, the upper grating starts before the lower grating, and that the offset portion of the upper grating acts as a reflector, reducing the reflection R_{12}. Similarly, the transmission T_{11} is also reduced because the upper grating ends before the lower grating. Simulations also shows that there is about 10μm tolerance for the offset beyond which the coupling efficiency drops by 50%. Design of this coupler therefore requires a careful consideration of the dislocation between two gratings.

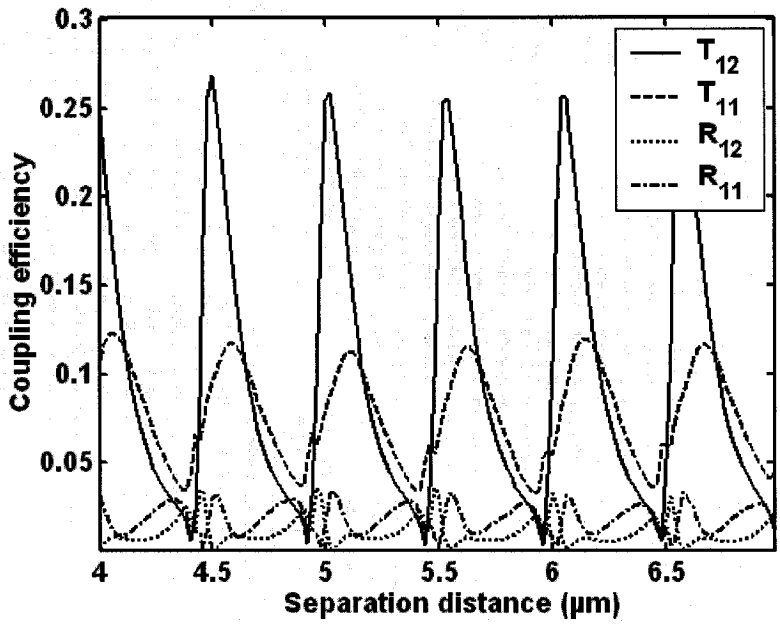

Figure 4.9. Coupling efficiency versus the thickness of the separation layer. The other parameters used are the same as for Fig. 4.7.

We can now summarize the conditions necessary to maximize the coupling efficiency T_{12}: (1) The periods of the lower grating and the upper grating should be matched so that the radiated light outcoupled from the lower grating can be coupled into the forward guided mode of the upper guiding layer and vice versa; (2) The thickness of the separation layers should satisfy the resonance condition of the FP cavity formed by two gratings; (3) The thickness of the oxide layer should be suitably selected so that constructive interference occurs between the reflection of the oxide/substrate interface and the direct radiation field by the gratings; (4) The axial offset between the two gratings should be optimized so that the reflection R_{12} and the transmission T_{11} can be reduced.

4.4 Simulation using FDTD

The results obtained by EEM have been verified by 2-D FDTD simulation. The perfectly matched layer is used as boundary condition and 0.005μm×0.01μm mesh size is adopted in the calculation model. Continuous-wave excitation is applied and we measure the transmission and reflectance at the both ends of the guiding layers. We obtained good

agreement between the two methods; this demonstrates that the EEM method provides an accurate and fast simulation method for this complex double-grating structure. The field

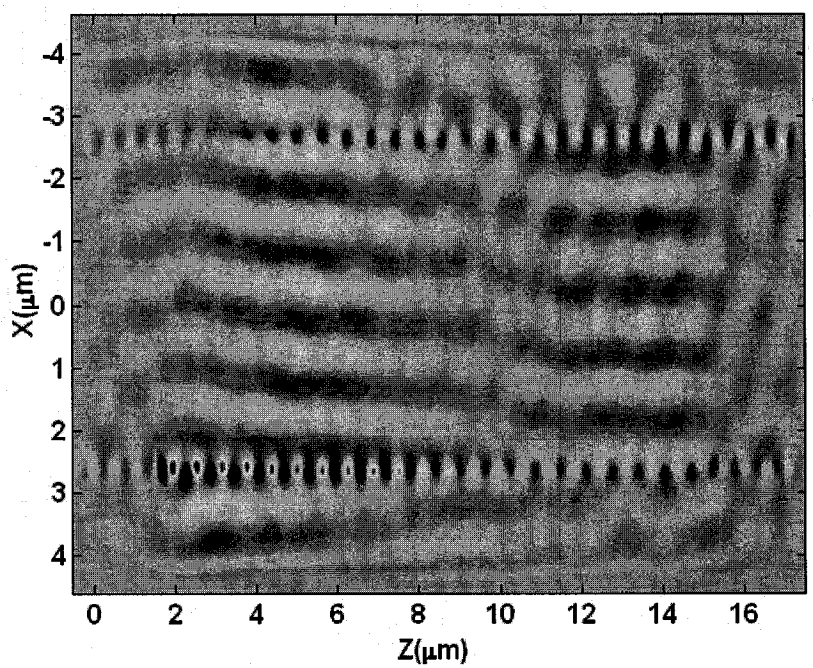

Figure 4.10. Field distribution of the double-grating coupler, calculated by FDTD. The parameters used are the same as for Fig. 4.7. In this figure, X=0μm is the midpoint between the two silicon guiding layers. The light is incident at Z=1.5μm from left to right in the lower silicon guiding layer. Both gratings start from Z=2μm and both grating lengths are 12.9μm.

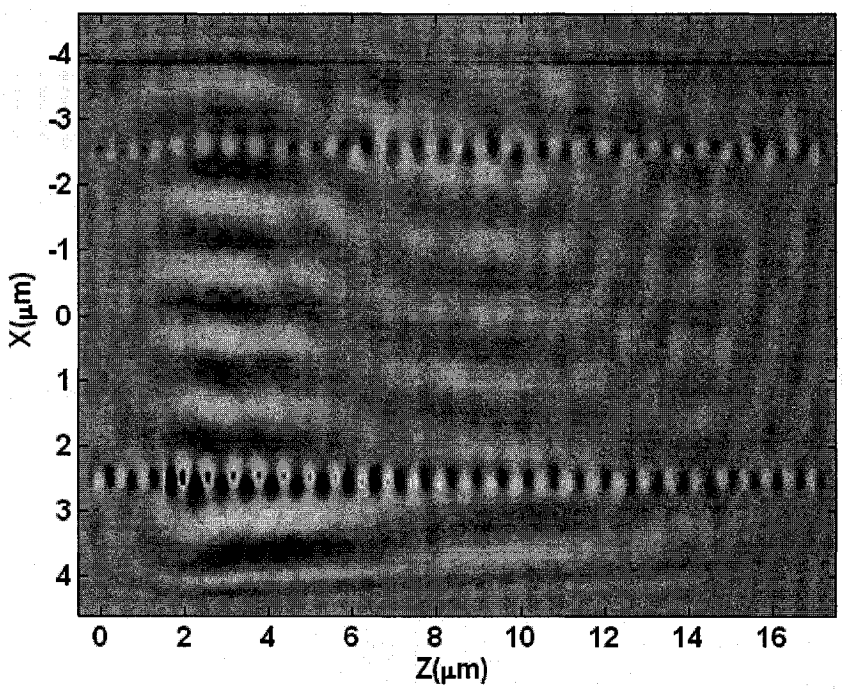

Figure 4.11. Field distribution of the double-grating coupler calculated by FDTD under the condition that the separation thickness is 4.8μm. The other parameters used are the same as for Fig. 4.10.

distribution is shown in Fig. 4.10 with the optimized parameters in Sec. 4.3 (assuming that there is no axial offset of the gratings). It is seen that in the near end of the lower grating, the radiation mode is coupled into both the separation region and the substrate region at an angle just off 90°. FP resonance is established towards the far end the grating regions, enhancing the coupling efficiency T_{12}. The values of T_{12} and T_{11} obtained by FDTD are 21% and 7%, while those obtained by EEM are 25% and 8%. The difference between two methods may come from the difficulty in determining the mode intensity in the FDTD simulation. In Fig. 4.11, we show the field distribution under the condition that the separation thickness is 4.8μm. The computed values for T_{12} and T_{11} are 3% and 5% respectively, which are very close to those obtained by EEM (4% and 5%). With this separation thickness, the FP resonance condition cannot be satisfied. In the near end of the lower grating, the radiation modes are outcoupled by the lower grating and are incoupled into the upper guiding layer. However, the guided power in the upper guiding

layer will be outcoupled back into radiation modes during propagation. Because FP resonance cannot be established, these radiation modes cannot be coupled into guided modes again, in neither lower guiding layer nor upper guiding layer. Therefore, both the coupling efficiencies of T_{12} and T_{11} decrease, compared with those in Fig. 4.10. The above observations not only agree well with the simulation results obtained in Sec. 4.3, but also verify the coupling mechanism deduced in Sec. 4.3. However, the computation time is much longer compared with EEM, which makes FDTD less suitable for the optimization of these waveguide grating couplers. For comparison, the typical time to calculate the structure by CAMFR is less than 2 minutes in a Pentium IV 1.5 GHz with 256 MB of memory, but about 5 hours for FDTD simulation.

4.5 Discussion and conclusions

The highest coupling efficiency of T_{12} was found to be 29% with 20 grating periods, which is relatively low compared with direct adiabatic coupling between guided modes. However, there are some ways to improve this efficiency. One of these is to fabricate a first-order Bragg grating after the lower grating, which serves to reduce the transmission of T_{11}. If another first-order Bragg grating is fabricated before the upper grating, the reflection R_{12} is reduced. Another way is to reduce the radiation loss in the substrates. Many methods have been proposed to increase the directionality of radiation [14]-[16]. This can be realized, for example, by adding a photonic band gap layer, or even a metallic mirror below the guiding layer. Another effective way to reduce the loss in the substrate is to optimize the groove shape. For instance, we can use a blazed grating to enhance radiation efficiency to the separation region. However, this structure is difficult to simulate and to fabricate. We have used 2-D FDTD to simulate a blazed-grating structure with parallelogram grooves (the grating depth and grating period are the same as those in Sec. 4.3) and achieved 40% coupling efficiency of T_{12} with a 10μm long grating structure. Since this structure was not completely optimized, even greater efficiencies may be possible.

As discussed in the first section, the first application of such double-grating coupler is to transfer energy between two waveguides whose direct coupling between guided modes is hard to realize. The coupling between vertical integration of waveguides on a substrate

is attractive in constructing high-density three-dimensional integrated photonic circuits. The coupler studied in this chapter is very compact with a typical length about 10μm, which allows dense interconnects. Another important advantage is that the two waveguides can be dissimilar, making this technique suitable for heterogeneous integration between different material systems. Future work will consider the application of this method to the vertical integration of high-index active semiconductor waveguides to the passive low-index waveguides. Besides, the analysis on various tolerances has to be done for any practical applications. The tolerance for grating periods may be in the range of about 20nm, based on the bandwidth of the coupling efficiency. The tolerance for waveguide separation is about 100nm, suggested by the result from Fig. 4.9. For practical applications, the coupling efficiency should be improved further by incorporating more complex grating structures or reflectors. The requirement of the coupling efficiency may vary for different applications. The increase of the coupling efficiency is also important to reduce the unwanted scattering light which may induces crosstalk between different photonic components.

The simulations that we performed here did not take any lateral diffraction into account. This will obviously become more significant as the vertical separation of the gratings increases and will lead to additional losses. Future work will need to perform a full 3-D simulation. Furthermore we have only investigated optimization for TE polarized light here. Due to the strong gratings that are used, this device will exhibit strong polarization dependence which may be a disadvantage in some applications. To experimentally demonstrate the present structure, it will be necessary to align the upper and lower waveguides very precisely before bonding and it will be challenging to achieve the strict thickness requirement of the separation layer. However these tolerances are achievable using either wafer bonding or flip chip bonding techniques. Furthermore the present design is not restricted to SOI waveguides, but can also be applied to waveguides fabricated in other high-index-contract materials. For example, it is possible to fabricate silicon nitride waveguides by multilayer deposition, which would allow gratings in two layers to be aligned lithographically during fabrication.

In summary, we have analyzed a compact double-grating structure which could be used for the vertical integration of planar waveguides. Deep and short quasi-second-order

gratings are used for outcoupling and incoupling between guided modes and radiation modes. A rigorous analytical method, based on EEM, has been employed to analyze and optimize this structure. In order to analyze the double-grating structure in EEM it was necessary to develop a novel slicing technique. This is the first reported application of EEM to double-grating structures and we found it to be well suited to the optimization of these structures. FDTD was then used to verify the final design. Simulation results from both methods agree well. The highest coupling efficiency was found to be 29% with 12.9μm long gratings and this efficiency can be improved by incorporating reflectors or using blazed gratings. A coupling efficiency of 40% was obtained with blazed gratings. Detailed analysis indicates that vertical FP resonance between two gratings enhances the coupling efficiency, which makes the control of the distance between the two waveguides critical if high efficiency is to be obtained.

References

[1] M. Raburn, B. Liu, K. Rauscher, Y. Okuno, N. Dagli, and J. E. Bowers, "3-D photonic circuit technology," *IEEE J. Selected Topics Quantum Electron,* vol. 8, pp. 935-942, 2002.

[2] W. Sotoyama, S. Tatsuura, K. Motoyoshi, and T. Yoshimura, "Directional-coupled optical switch between stacked waveguide layers using electro-optic polymer," *Jpn, J. Appl. Phys.*, vol. 31, no. 8B, pp. L1180-L1181, 1992.

[3] C. Wu, C. Rolland, F. Shepherd, C. Larocque, N. Puetz, K. D. Chik, and J. M. XU, "InGaAsP/InP vertical directional coupler filter with optimally designed wavelength tunability," *IEEE Photon. Technol. Lett.*, vol. 4, pp. 457-459, Apr. 1992.

[4] Z. M. Chuang and L. A. Coldren, "Enhanced wavelength tuning in grating-assisted codirectional coupler filter," *IEEE Photon. Technol. Lett.*, vol. 5, pp. 1219-1221, Oct. 1993.

[5] M. Horita, T. Yamazaki, S. Tanaka, and Y. Matsushima, "Polarization insensitive and tunable optical add and drop multiplexer utilizing vertically stacked buried semiconductor waveguides," *Electron. Lett.*, vol. 35, no. 20, pp. 1733-1734, 1999.

[6] S. M. Garner, V. Chuyanov, S.-S. Lee, A. Chen, W. H. Steier, and L. R. Dalton, "Vertically integrated waveguide polarization splitters using polymers," *IEEE Photon. Technol. Lett.*, vol. 11, pp. 842-844, Jul. 1999.

[7] B. Jalali, S. Yegnanarayanan, T. Yoon, T. Yoshimoto, I. Rendina, and F. Coppinger, "Advances in silicon-on-insulator optoelectronics," *IEEE J. Selected Topics Quantum Electron,* vol. 4, pp. 938-947, 1998.

[8] Q. Xing, S. Ura, T. Suhara, and H. Nishihara, "Contra-directional coupling between stacked waveguides using grating couplers," *Opt. Commun.*, vol. 144, pp.180-182, 1997.

[9] S. Ura, R. Nishida, T. Suhara, and H. Nishihara, "Wavelength-selective coupling among three vertically integrated optical waveguides by grating couplers," *IEEE Photon. Technol. Lett.*, vol. 13, pp. 133-135, Feb. 2001.

[10] T. Liang and R. W. Ziolkowski, "Grating assisted waveguide-to-waveguide couplers," *IEEE Photon. Technol. Lett.*, vol. 10, pp. 693-695, May 1998.

[11] P. Bienstman and R. Baets, "Optical modeling of photonic crystals and VCSEL's using eigenmode expansion and perfectly matched layers," *Opt. Quantum Electron.*, vol. 33, pp. 327-341, Apr. 2001.

[12] J. Ctyroky, S. Helfert, R. Pregla, P. Bienstman, R. Baets, R. Deridder, R. Stoffer, G. Klaasse, J. Petracek, P. Lalanne, J. –P. Hugonin and R. M. Delarue, "Bragg waveguide grating as a 1D photonic band gap structure: COST 268 modelling task," *Opt. and Quantum Electron.*, vol. 34, pp. 455-470, 2002.

[13] D. Taillaert, W. Bogaerts, P. Bienstman, T. F. Krauss, P. V. Daele, I. Moerman, S. V.erstuyft, K. D. Mesel and R. Baets, "An out-of-plane grating coupler for efficient butt-coupling between compact planar waveguides and single-mode fibers," *IEEE J. Quantum Electron.*, vol. 38, pp. 949-955, July 2002.

[14] S. Miyanaga and T. Asakura, "Intensity profile of outgoing beams from uniform and linearly tapered grating couplers," *Appl. Opt.*, vol. 20, pp. 688-695, Feb. 1981.

[15] W. Streifer, D. R. Scifres, and R. Burnham, "Analysis of grating-coupled radiation in GaAs:GaAlAs lasers and waveguides," *IEEE J. Quantum Electron.*, vol. QE-12, pp. 422-428, July 1976.

[16] A. Hardy, D. F. Welch, and W. Streifer, "Analysis of second-order gratings," *IEEE J. Quantum Electron.*, vol. QE-25, pp. 2096-2105, Oct. 1989.

CHAPTER 5 SECOND HARMONIC GENERATION IN WAVEGUIDE DIRECTIONAL COUPLERS

In this chapter, we present the systematic coupled mode theory of second-harmonic generation in directional coupler structures. We find an interesting resonance phenomenon which is equivalent to a phase-matched effect. An analogous driven harmonic oscillator model explains the origin of the resonance effect, and resonance conditions can be directly predicted by this model. Pump depletion will be included in our calculation and we demonstrate a phenomenon in which the optical power is exchanged between the fundamental wave and the second harmonic wave under the resonance condition. We also investigate the effects of waveguide loss on the resonance condition and the conversion efficiency.

5.1 Introduction

Nonlinear optical frequency conversion has many applications, including high-density optical recording, printing, high-resolution laser pattern generation, industrial and medical spectroscopic systems and optical signal processing. Efficient frequency conversion only occurs when the phase-matching condition between generated wave and pump wave(s) is obtained. This condition is required in order to ensure that the nonlinearly induced frequency components sum constructively. A range of phase-matching techniques exist. These include using the natural birefringence of certain crystals [1] (which can achieve perfect phase-matching) and quasi-phase-matching (QPM) which requires the spatially periodic modulation of nonlinear optical coefficients (or refractive indices sometimes) and which has achieved great success in recent years [2]-[4]. Other phase-matching methods have been achieved in waveguide structures where modal dispersion phase matching [5][6], anomalous-dispersion phase matching [7] and Cerenkov phase matching [8][9] have been demonstrated.

When two optical waveguides are close together, because of the interaction of the guided modes of each waveguide, optical power can be coupled between two waveguides.

This structure is called a directional coupler, which has been intensively used in the area of integrated optics. Coupled-mode theory, which has been successfully developed to describe the directional coupler, shows that a spatial periodic modulation of light intensity occurs while the light is propagating in such structure.

In this chapter, we study second harmonic generation in waveguide directional couplers. If the phase matching condition is not satisfied, the power of the generated wave will oscillate with the interaction length due to the destructive interference between the waves generated at different positions. However, the directional coupler also periodically modulates the generated radiation at the same time. As a result, the conversion efficiency of nonlinear effects can be enhanced greatly under some resonant conditions. We will apply this theory to second-harmonic generation, but similar resonant conditions also exist for other nonlinear optical effects. Theoretical conversion efficiency can be 100% for SHG, similar to the perfect phase-matching condition. The proposed configuration has not only fundamental theoretical significance for nonlinear optics but also major technical advantages including very small beam size, large spatial overlap of fundamental and harmonic fields, long interaction lengths with low loss, high conversion efficiency of nonlinear effects, and simplicity of fabrication without any spatially periodic poling.

5.2 Second-harmonic generation in directional couplers

Assuming that the nonlinear effect and the coupling between two waveguides do not affect significantly the waveguide modes, and all the interacting modes are TE modes, the mode fields can be expressed by $\vec{E}_i^{\omega_j} = \vec{e}_y F_i^{\omega_j}(x)\exp(-i\beta_i^{\omega_j} z + i\omega_j t)$, where $\beta_i^{\omega_j}$ is the corresponding propagation constant and the subscript i=1,2 represents the ith waveguide and j=1,2 denotes the fundamental wave and the harmonic generation respectively. Similar to Eq. (2.9), the electric field in a directional coupler can be defined as

$$\vec{E} = \frac{1}{2}\left(A_\omega(z)\vec{E}_1^{\omega} + A_{2\omega}(z)\vec{E}_1^{2\omega} + B_\omega(z)\vec{E}_2^{\omega} + B_{2\omega}(z)\vec{E}_2^{2\omega}\right) + c.c \qquad (5.1)$$

where $A_{\omega_j}(z)$ and $B_{\omega_j}(z)$ are the slowly varying amplitudes in waveguides 1 and 2, respectively. The coupled-amplitude equations governing the motions of the amplitudes are found under the slowly-varying-amplitude approximation (see Appendix A):

$$\begin{cases} \dfrac{dA_\omega}{dz} = -\alpha_1^\omega A_\omega - i\kappa_\omega B_\omega \exp(-i\Delta\beta_\omega z) - i\eta_1^\omega A_{2\omega} A_\omega^* \exp(-i\Delta k_1 z) \\ \dfrac{dB_\omega}{dz} = -\alpha_2^\omega B_\omega - i\kappa_\omega A_\omega \exp(i\Delta\beta_\omega z) - i\eta_2^\omega B_{2\omega} B_\omega^* \exp(-i\Delta k_2 z) \\ \dfrac{dA_{2\omega}}{dz} = -\alpha_1^{2\omega} A_{2\omega} - i\kappa_{2\omega} B_{2\omega} \exp(-i\Delta\beta_{2\omega} z) - i\eta_1^{2\omega} A_\omega^2 \exp(i\Delta k_1 z) \\ \dfrac{dB_{2\omega}}{dz} = -\alpha_2^{2\omega} B_{2\omega} - i\kappa_{2\omega} A_{2\omega} \exp(i\Delta\beta_{2\omega} z) - i\eta_2^{2\omega} B_\omega^2 \exp(i\Delta k_2 z) \end{cases} \tag{5.2}$$

Similar coupled equations have previously been obtained for all-optical switching devices based on large nonlinear phase shifts from second harmonic generation (for an example, see Ref. [10]). One can also derive the above equations by following the same method as that reported in Refs. [11][12]. Here, κ_ω and $\kappa_{2\omega}$ are the mode-coupling coefficients of the directional coupler for the fundamental and the second harmonic waves, respectively. $\eta_i^{\omega_j}$ includes the product of the nonlinear optical coefficient and the overlap integral of the fundamental and the second harmonic waves. $\Delta\beta_{\omega_j}$ denotes the phase mismatch between two guided modes in different waveguides at the same frequency, while Δk_i denotes the phase mismatch between the fundamental and the second harmonic waves in the same waveguide. A real waveguide system has waveguide attenuation, mainly resulting from scattering loss and absorption loss. The loss terms have been phenomenologically added in the above equations and $\alpha_i^{\omega_j}$ is the attenuation coefficient of the field amplitude at the frequency ω_j in the *i*th waveguide. It is easy to understand the above coupled equations: the second terms in the right-hand sides describe the coupling effect of the directional coupler and the third terms in the right-hand sides result from the nonlinear effects. If one of them is absent, the equations simplify to those of a conventional directional coupler or SHG in a single waveguide.

Usually the two waveguides in the directional coupler are identical, so that

$$\begin{cases} \Delta\beta_\omega = \Delta\beta_{2\omega} = 0 \\ \Delta k_1 = \Delta k_2 = \Delta k = \beta_{2\omega} - 2\beta_\omega \\ \eta_1^{\omega_j} = \eta_2^{\omega_j} = \eta^{\omega_j} \\ \alpha_1^{\omega_j} = \alpha_2^{\omega_j} = \alpha^{\omega_j} \end{cases} \tag{5.3}$$

Eqs. (5.2) are the starting equations for our study of SHG in the directional coupler. However, analytical solutions are not straightforward since the coupled equations are not even linear differential equations. We first consider some cases in which the loss terms are zero and the input fundamental field is incident only in the first waveguide and there is no second harmonic input. To obtain analytical solutions, we have to use a non-depletion assumption under which the power conversion from the pump to the second harmonic wave is extremely low. Under this assumption, the first two equations in Eqs. (5.2) become:

$$\begin{cases} \dfrac{dA_\omega}{dz} = -i\kappa_\omega B_\omega \\ \dfrac{dB_\omega}{dz} = -i\kappa_\omega A_\omega \end{cases} \tag{5.4}$$

whose solution is

$$\begin{cases} A_\omega = A_0 \cos(\kappa_\omega z) \\ B_\omega = -iA_0 \sin(\kappa_\omega z) \end{cases} \tag{5.5}$$

under the condition that the light is only coupled into the first waveguide at $z = 0$, namely, $A_\omega(0) = A_0$ and $B_\omega(0) = 0$ [12][13]. The validity of this solution associated with the non-depletion assumption will be discussed later on. Substituting Eqs. (5.5) into the last two equations in Eqs. (5.2), we can obtain the coupled equations for the amplitudes $A_{2\omega}$ and $B_{2\omega}$ under the non-depletion assumption.

5.2.1 Case of $\kappa_{2\omega} = \kappa_\omega = 0$

We first consider the case in which the coupling between two waveguides for the second harmonic wave and the fundamental wave are both zero, namely, $\kappa_{2\omega} = \kappa_\omega = 0$. It is expected that under these conditions, the fundamental and the second harmonic waves only propagate in the first waveguide and thus this SHG phenomenon is exactly the same as that in a single waveguide, as has been well studied before. With a nonzero phase mismatch, the efficiency of SHG oscillates with propagation distance due to destructive interference between the second harmonic waves generated at different

locations. Under the phase-matching condition $\Delta k = 0$, the SHG amplitude in the first waveguide with the non-depletion assumption is:

$$A_{2\omega} = -i\eta^{2\omega} A_0^2 z \tag{5.6}$$

5.2.2 Case of $\kappa_{2\omega} = 0$ and $\kappa_{\omega} \neq 0$

We next study the case in which $\kappa_{2\omega} = 0$ but $\kappa_{\omega} \neq 0$, namely, the coupling between the two waveguides for the fundamental wave exists but that for the second harmonic wave is zero. This case is actually realizable in experiments. For the same-order waveguide modes of the fundamental wave and the second harmonic wave, the coupling coefficient κ_{ω} is usually larger than $\kappa_{2\omega}$ because a longer wavelength results in a larger field overlap between two modes in two waveguides [13]. Therefore, for a reasonably short waveguide length, $\kappa_{2\omega}$ can be approximated by zero but not κ_{ω}. Furthermore, if the waveguide modes with different orders are used for the fundamental and the second harmonic waves, we may be able to find such a situation that $\kappa_{2\omega} = 0$ but $\kappa_{\omega} \neq 0$. Again, we assume that the fundamental wave is incident in the first waveguide and no light at the second-harmonic frequency is incident at any waveguides. In this situation, the coupling equations for SHG with the non-depletion assumption are:

$$\begin{cases} \dfrac{dA_{2\omega}}{dz} = -i\eta_1^{2\omega} A_0^2 \cos^2(\kappa_{\omega} z)\exp(i\Delta kz) = -\dfrac{i\eta_1^{2\omega} A_0^2}{4}\left(\exp(i2\kappa_{\omega} z) + 2 + \exp(-i2\kappa_{\omega} z)\right)\exp(i\Delta kz) \\ \dfrac{dB_{2\omega}}{dz} = i\eta_2^{2\omega} A_0^2 \sin^2(\kappa_{\omega} z)\exp(i\Delta kz) = -\dfrac{i\eta_1^{2\omega} A_0^2}{4}\left(\exp(i2\kappa_{\omega} z) - 2 + \exp(-i2\kappa_{\omega} z)\right)\exp(i\Delta kz) \end{cases} \tag{5.7}$$

Since there is no coupling between the two waveguides for the second harmonic wave, the above equations are decoupled and thus analytical solutions can be easily obtained. The solutions are

$$\begin{cases} A_{2\omega} = -\dfrac{\eta^{2\omega} A_0^2}{4}\left(\dfrac{\exp(i(2\kappa_{\omega} + \Delta k)z)}{2\kappa_{\omega} + \Delta k} + \dfrac{2\exp(i\Delta kz)}{\Delta k} + \dfrac{\exp(i(-2\kappa_{\omega} + \Delta k)z)}{-2\kappa_{\omega} + \Delta k} - \dfrac{4\left(\Delta k^2 - 2\kappa_{\omega}^2\right)}{\Delta k(2\kappa_{\omega} + \Delta k)(-2\kappa_{\omega} + \Delta k)}\right) \\ B_{2\omega} = -\dfrac{\eta^{2\omega} A_0^2}{4}\left(\dfrac{\exp(i(2\kappa_{\omega} + \Delta k)z)}{2\kappa_{\omega} + \Delta k} - \dfrac{2\exp(i\Delta kz)}{\Delta k} + \dfrac{\exp(i(-2\kappa_{\omega} + \Delta k)z)}{-2\kappa_{\omega} + \Delta k} - \dfrac{8\kappa_{\omega}^2}{\Delta k(2\kappa_{\omega} + \Delta k)(-2\kappa_{\omega} + \Delta k)}\right) \end{cases} \tag{5.8}$$

for

$$\Delta k \neq 0, \pm 2\kappa_\omega \tag{5.9}$$

and

$$\begin{cases} A_{2\omega} = -\dfrac{\eta^{2\omega} A_0^2}{4}\left(2iz + \dfrac{\exp(i(2\kappa_\omega)z)}{2\kappa_\omega} - \dfrac{\exp(i(-2\kappa_\omega)z)}{2\kappa_\omega}\right) \\ B_{2\omega} = -\dfrac{\eta^{2\omega} A_0^2}{4}\left(-2iz + \dfrac{\exp(i(2\kappa_\omega)z)}{2\kappa_\omega} - \dfrac{\exp(i(-2\kappa_\omega)z)}{2\kappa_\omega}\right) \end{cases} \text{for } \Delta k = 0 \tag{5.10}$$

and

$$\begin{cases} A_{2\omega} = -\dfrac{\eta^{2\omega} A_0^2}{4}\left(iz + \dfrac{\exp(i2\Delta kz)}{2\Delta k} + \dfrac{2\exp(i\Delta kz)}{\Delta k} - \dfrac{5}{2\Delta k}\right) \\ B_{2\omega} = -\dfrac{\eta^{2\omega} A_0^2}{4}\left(iz + \dfrac{\exp(i2\Delta kz)}{2\Delta k} - \dfrac{2\exp(i\Delta kz)}{\Delta k} + \dfrac{3}{2\Delta k}\right) \end{cases} \text{for } \Delta k = \pm 2\kappa_\omega \tag{5.11}$$

In Eq. (5.8), the first three terms in the bracket in the right-hand side all oscillate with the interaction length. Therefore, the conversion efficiency of SHG will also oscillate with the interaction length, which results in a low conversion efficiency. In Eqs. (5.10-5.11), however, the first term in the bracket is proportional to z, which is the same as the solution for the perfect matching condition in a single waveguide structure, as shown by Eq. (5.6). This indicates that a high conversion can be obtained under the condition that $\Delta k = 0, \pm 2\kappa_\omega$. Eq. (5.10) shows that the conversion efficiency can be high with the condition $\Delta k = 0$ even with the presence of the coupling of the fundamental wave. In Eq. (5.11), $\Delta k = \pm 2\kappa_\omega$ gives rise to a quasi-phase matching condition, which actually has been proposed in Ref. [14] several years ago. This QPM results from the periodic intensity modulation of the fundamental wave which produces a phase term, compensating the phase mismatch Δk. From Eq. (5.7), we find that the cosine and sine terms for the amplitude of the fundamental wave produce the exponential terms such as $\exp(\pm i2\kappa_\omega z)$ which cancel $\exp(i\Delta kz)$ under the condition that $\Delta k = \pm 2\kappa_\omega$, resulting in this intensity-modulation induced QPM.

As in the above derivations, a non-depletion assumption has been used to obtain the analytical solutions. This assumption results in Eqs. (5.5) by neglecting the terms consisting of the amplitude of the second harmonic in the first two equations in Eqs. (5.2).

However, one must carefully consider the validity of Eqs. (5.5) since we have seen that the amplitude of the fundamental wave also goes to zero at particular positions and thus neglecting those near-zero terms including the SHG amplitudes may not be accurate. Figs. 5.1-5.3 depict the normalized power of the fundamental and the second harmonic waves versus the interaction length under the conditions that $\kappa_\omega = 0, \Delta k/10, \Delta k/2$, respectively. The curves in these figures are numerically obtained directly from Eqs. (5.2). Obviously, the curves in Fig. 5.2(a-b) and Fig. 5.3(a-b) verify that the directional coupler modulates the intensity of the fundamental wave following the description of Eqs. (5.5). This confirms the accuracy of the use of Eqs. (5.5) under the non-depletion assumption. In Figs. 5.1-5.2, no quasi-phase matching condition is satisfied and therefore, the power of SHG oscillates with the interaction length. In Fig. 5.3, the quasi-phase matching condition $\Delta k = 2\kappa_\omega$ is satisfied, and the power of the second harmonic wave grows with the interaction length. We also show the case that $\Delta k = 0$, but $\kappa_\omega \neq 0$ in Fig. 5.4, as described by Eq. (5.10). In fact, the curves for the second harmonic wave in Fig. 5.3(c) and Fig.5.4(c) are quite similar to those for QPM with periodic nonlinear constants [4]. All the curves in Figs. 5.1-5.4 are consistent with the analytical solutions shown by Eqs. (5.8-5.11).

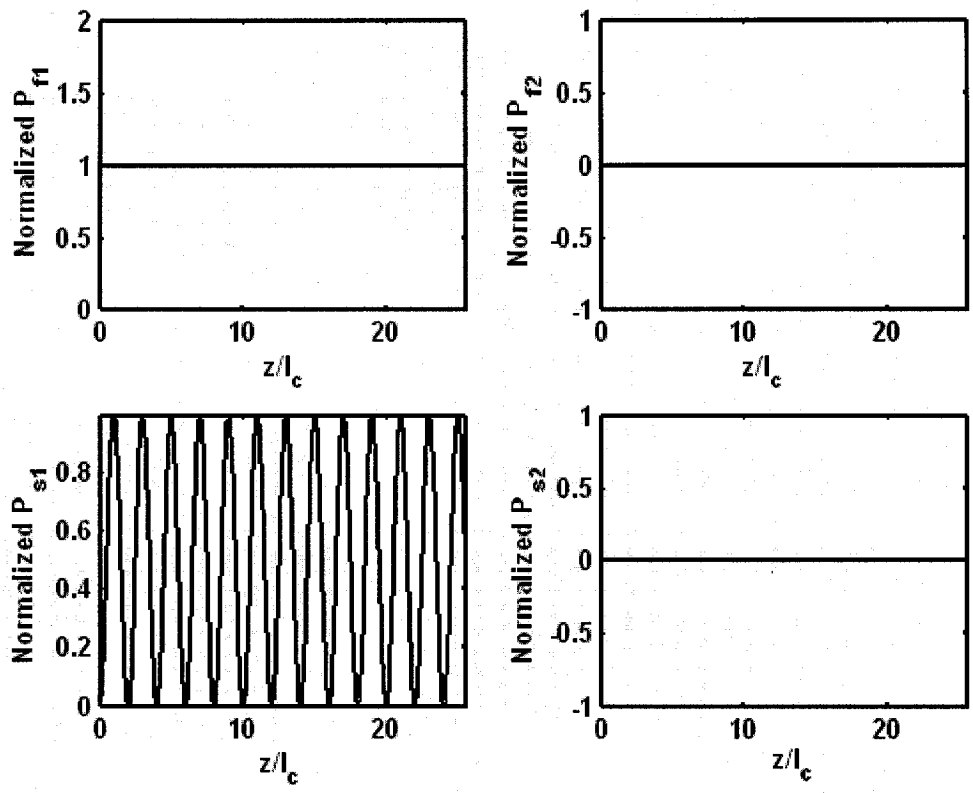

Figure 5.1. Normalized power for the fundamental wave and the second harmonic wave versus the interaction length. P_{f1} and P_{f2} are the normalized power for the fundamental wave in the first waveguide and the second waveguide, respectively. They are normalized to the peak value of P_{f1}. P_{s1} and P_{s2} are the power for the second harmonic wave in the first waveguide and the second waveguide, respectively. They are normalized to the peak value of P_{s1}. In this figure, we use the conditions that $\Delta k \neq 0$ and $\kappa_\omega = \kappa_{2\omega} = 0$. The coherence length is defined as $l_c = \frac{\pi}{\Delta k}$.

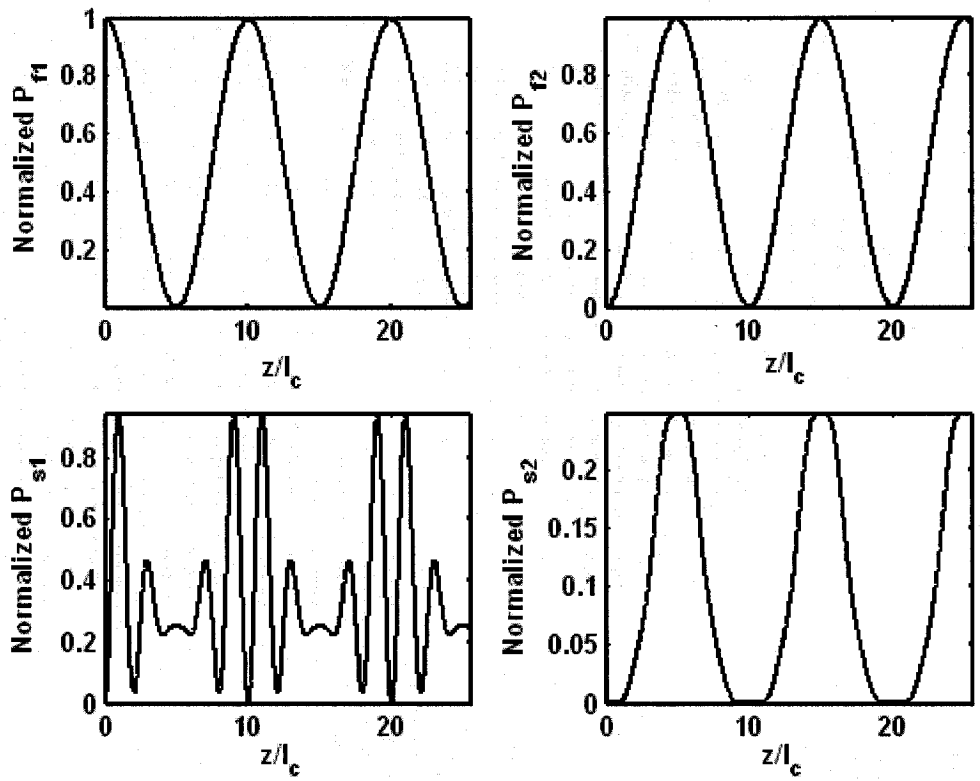

Figure 5.2. Normalized power for the fundamental wave and the second harmonic wave versus the interaction length. Here, the second harmonic power is normalized to the peak SHG power obtained in Fig. 5.1. In this figure, we use the conditions that $\Delta k \neq 0$, $\kappa_{2\omega} = 0$ and $\kappa_{\omega} = \Delta k / 10$.

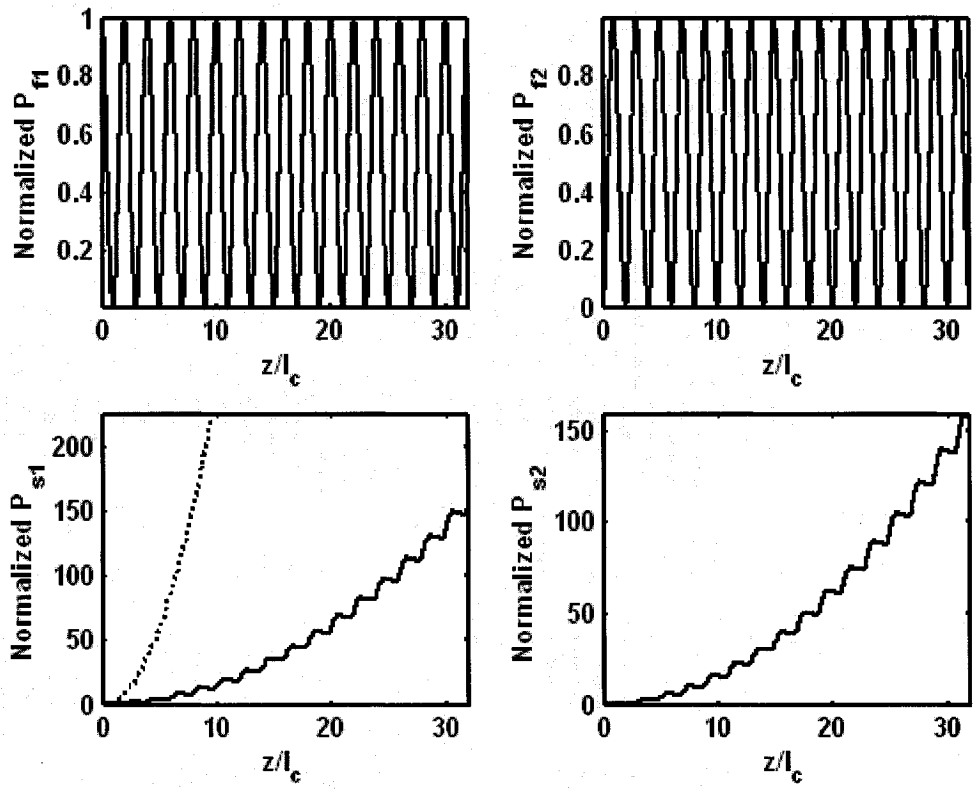

Figure 5.3. Normalized power for the fundamental wave and second harmonic wave versus the interaction length. Here, the second harmonic power is normalized to the peak SHG power obtained in Fig. 5.1. In this figure, we use the conditions that $\Delta k \neq 0$, $\kappa_{2\omega} = 0$ and $\kappa_{\omega} = \Delta k / 2$. The dotted curve shows the reference line for the perfect-matching case under equivalent conditions.

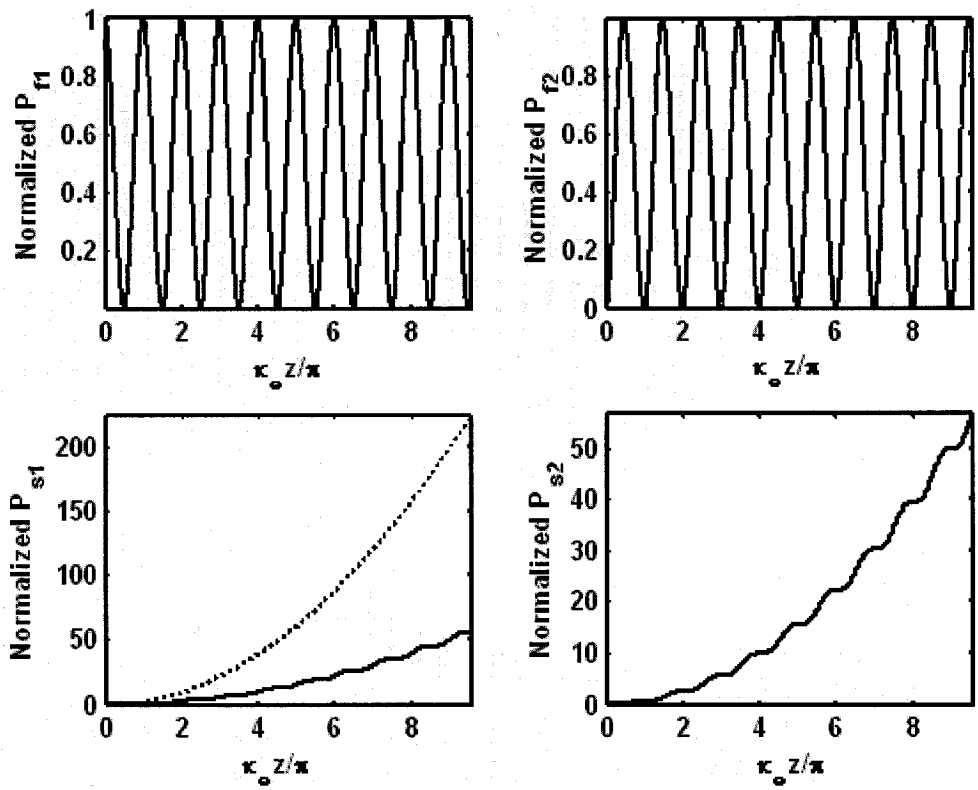

Figure 5.4. Normalized power for the fundamental wave and the second harmonic wave versus the interaction length. Here, the SHG power is normalized to the peak SHG power obtained in Fig. 5.1. In this figure, we use the conditions that $\Delta k = 0$, $\kappa_{2\omega} = 0$ and $\kappa_{\omega} \neq 0$. The dotted curve shows the reference line for the perfect-matching case under equivalent conditions.

We can use the numerical simulation to study the pump depletion when the interaction length is sufficiently long. Fig. 5.5 shows the conversion efficiency of SHG for a longer interaction length with the conditions that $\Delta k = 0$ and $\kappa_{\omega} \neq 0$. Power depletion occurs and the total conversion efficiency to the second harmonic wave finally reaches 100%, similar to the situation for perfect matching or quasi-phase matching in single waveguides or bulk nonlinear crystals [1]. Furthermore, the power does normally convert back to the fundamental wave again. Fig. 5.6 demonstrates the development of conversion efficiency

for the case that $\Delta k = 2\kappa_\omega$. It is to be noted that SHG with pump depletion under this intensity-modulation induced QPM has not been previously investigated (to the best of our knowledge), even in Ref. [14]. Surprisingly, the conversion efficiency shows very interesting features. The maximum conversion efficiency is only close to 50%, but not 100% as in any quasi-phase matching cases studied before [4][15]. Furthermore, the light power can transfer back to the fundamental wave after the second harmonic power obtains its maximum values. We observe a periodic exchange of the power between the fundamental wave and the second harmonic wave under this QPM condition. So far we know, this phenomenon has not been described before in any quasi-phase matched system. We first explain why the maximal conversion efficiency is 100% under the condition that $\Delta k = 0$ but 50% under the condition that $\Delta k = 2\kappa_\omega$. From Eq. (5.7), the coefficient before the exponential term $\exp(i(-2\kappa_\omega + \Delta k)z)$ is only half of that for the term $\exp(i\Delta kz)$. This implies that the conversion efficiency for the quasi-phase matching condition $\Delta k = 2\kappa_\omega$ can be only half of that for the case that $\Delta k = 0$. By comparing the z-proportional terms in Eq. (5.10) and Eq. (5.11), we can also reach the above conclusion. This conclusion can be applied to the pump-depletion situation and thus a factor of 2 between two maximum conversion efficiencies occurs. In addition, from the solution in Eq. (5.10), one can easily verify that both $|A_{2\omega}|^2$ and $|B_{2\omega}|^2$ increases monotonically with the propagation distance z for the case that $\Delta k = 0$. It is thus expected that in the pump-depletion region, the total conversion efficiency also increases monotonically with the propagation distance z and finally 100% conversion efficiency is obtainable and the power will be not converted back to the fundamental wave. In contrast, the solution in Eq. (5.11) indicates that $|A_{2\omega}|^2$ and $|B_{2\omega}|^2$ cannot increase monotonically with the propagation distance z for the case that $\Delta k = 2\kappa_\omega$. From the inset of Fig. 5.6, we observe that the conversion efficiency is oscillating with the propagation distance even at the SHG maxima. This results in the back power conversion from the second-harmonic wave to the fundamental wave.

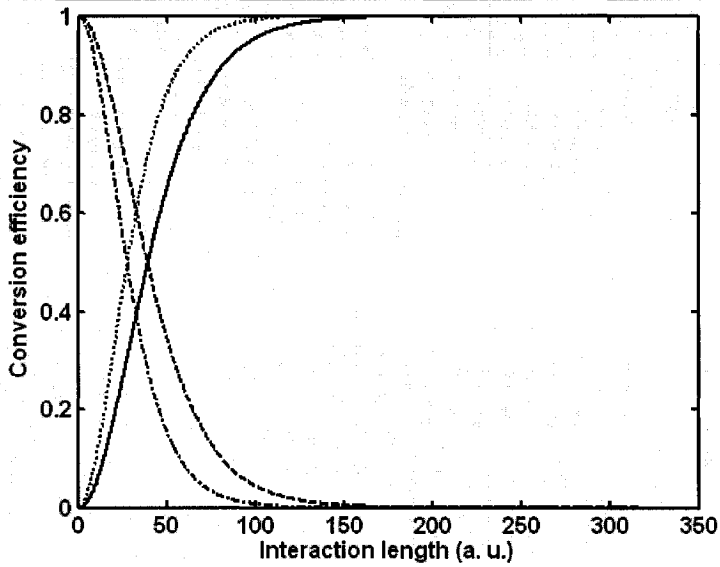

Figure 5.5. Conversion efficiency including pump depletion versus the interaction length. We use the conditions that $\Delta k = 0$, $\kappa_{2\omega} = 0$ and $\kappa_{\omega} \neq 0$. In this figure, the solid line represents the total conversion efficiency for SHG (the sum of the conversion efficiency in the two waveguides) and the dashed line represents the total conversion efficiency of the fundamental wave. The dotted and dash-dotted lines represent those for the perfect-matching case under equivalent conditions.

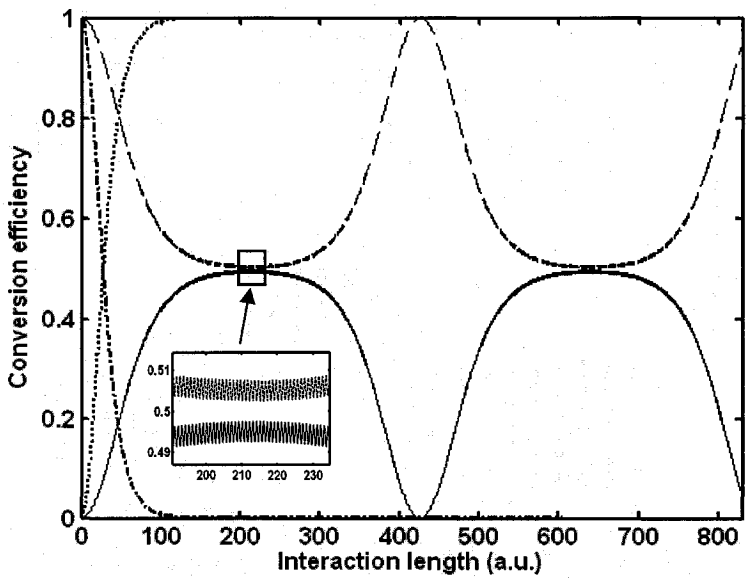

Figure 5.6. Same as fig. 5.5 but with the conditions that $\Delta k \neq 0$, $\kappa_{2\omega} = 0$ and $\kappa_{\omega} = \Delta k / 2$.

5.2.3 Case of $\kappa_\omega = 0$ and $\kappa_{2\omega} \neq 0$

We next consider the case in which $\kappa_\omega = 0$ but $\kappa_{2\omega} \neq 0$, namely the coupling between two waveguides for the second harmonic wave is nonzero but that for the fundamental wave is zero. This case is also feasible in reality, for instance, we can input a compound mode of the fundamental wave to the directional coupler. This mode will propagate in the directional coupler without transferring to other modes since it is an eigenmode of the compound structure. Therefore, the power of the fundamental wave will remain constant in each waveguide and thus there is no intensity modulation of the fundamental wave between the two waveguides. If only one of the two waveguides has nonlinear harmonic generation, the intensity of the second harmonic wave oscillates in the two waveguides, such that $\kappa_{2\omega} \neq 0$. Under the non-depletion assumption, the coupling equations for SHG become:

$$\begin{cases} \dfrac{dA_{2\omega}}{dz} = -i\kappa_{2\omega}B_{2\omega} - i\eta^{2\omega}A_0^2 \exp(i\Delta kz) \\ \dfrac{dB_{2\omega}}{dz} = -i\kappa_{2\omega}A_{2\omega} \end{cases} \tag{5.12}$$

It is to be noted that although Eqs. (5.12) are a set of first-order differential equations, the independent equation for $A_{2\omega}$ or $B_{2\omega}$ is actually a second-order differential equation. For example, from the above equation, we get the equation for $A_{2\omega}$ as

$$\frac{d^2A_{2\omega}}{dz^2} = -\kappa_{2\omega}^2 A_{2\omega} + \eta^{2\omega}A_0^2 \Delta k \exp(i\Delta kz) \tag{5.13}$$

By simple derivation, we can analytically solve the above equation. The final solutions are

$$\begin{cases} A_{2\omega} = \dfrac{\eta^{2\omega}A_0^2}{2(\Delta k - \kappa_{2\omega})}\exp(i\kappa_{2\omega}z) + \dfrac{\eta^{2\omega}A_0^2}{2(\Delta k + \kappa_{2\omega})}\exp(-i\kappa_{2\omega}z) + \dfrac{\eta^{2\omega}A_0^2\Delta k}{\kappa_{2\omega}^2 - \Delta k^2}\exp(i\Delta kz) \\ B_{2\omega} = \dfrac{-\eta^{2\omega}A_0^2}{2(\Delta k - \kappa_{2\omega})}\exp(i\kappa_{2\omega}z) + \dfrac{\eta^{2\omega}A_0^2}{2(\Delta k + \kappa_{2\omega})}\exp(-i\kappa_{2\omega}z) - \dfrac{\eta^{2\omega}A_0^2\kappa_{2\omega}}{\kappa_{2\omega}^2 - \Delta k^2}\exp(i\Delta kz) \end{cases} \quad \text{for } \Delta k \neq \pm\kappa_{2\omega}$$

(5.14)

and

$$\begin{cases} A_{2\omega} = -\dfrac{\eta^{2\omega}A_0^2}{4\kappa_{2\omega}}\exp(i\kappa_{2\omega}z) + \dfrac{\eta^{2\omega}A_0^2}{4\kappa_{2\omega}}\exp(-i\kappa_{2\omega}z) - \dfrac{i\eta^{2\omega}A_0^2}{2}\exp(i\Delta kz)z \\ B_{2\omega} = -\dfrac{\eta^{2\omega}A_0^2}{4\kappa_{2\omega}}\exp(i\kappa_{2\omega}z) + \dfrac{\eta^{2\omega}A_0^2}{4\kappa_{2\omega}}\exp(-i\kappa_{2\omega}z) + \dfrac{i\eta^{2\omega}A_0^2}{2}\exp(i\Delta kz)z \end{cases} \quad \text{for } \Delta k = \pm\kappa_{2\omega} \quad (5.15)$$

We see that there exists a condition $\Delta k = \pm\kappa_{2\omega}$ which results in a term in the solution proportional to the interaction length z. We compare the characteristics of the z-proportional terms in Eqs. (5.10) (5.11) and (5.15). The terms in Eq. (5.10) are $\dfrac{-i\eta^{2\omega}A_0^2 z}{2}$ for $A_{2\omega}$ and $\dfrac{i\eta^{2\omega}A_0^2 z}{2}$ for $B_{2\omega}$ with zero phase mismatch Δk. If $|A_{2\omega}|$ and $|B_{2\omega}|$ are added together, the sum has exactly the same magnitude as that in Eq. (5.6), which is the solution for SHG in a single waveguide with perfect phase-matching. This demonstrates that the condition for Eq. (5.10) is just a perfect-matching condition although the coupling between the two waveguides for the fundamental wave exists. The condition for Eq. (5.11) is an intensity-modulation induced QPM, and the terms proportional to z are $\dfrac{-i\eta^{2\omega}A_0^2 z}{4}$ for both $A_{2\omega}$ and $B_{2\omega}$. The magnitudes of these amplitudes for SHG are half of those in the perfect matching case, as discussed already. Nevertheless, the z-proportional terms in Eq. (5.15) show different characteristics from those in Eqs. (5.10-11). As can be seen, the z-proportional terms for $A_{2\omega}$ and $B_{2\omega}$ are $-\dfrac{i\eta^{2\omega}A_0^2}{2}\exp(i\Delta kz)z$ and $\dfrac{i\eta^{2\omega}A_0^2}{2}\exp(i\Delta kz)z$, respectively. They are not the same but have a π-phase difference. The sum of $|A_{2\omega}|$ and $|B_{2\omega}|$ has exactly the same magnitude as that in Eq. (5.6). Furthermore, an $\exp(i\Delta kz)$ term appears which is not present in those terms in Eqs. (5.10-11). In addition, for the quasi-phase matching condition, the SHG in each waveguide can be described by a first-order differential equation in the non-depletion region, such as Eqs. (5.7) for both $A_{2\omega}$ and $B_{2\omega}$. Nevertheless, since the amplitudes $A_{2\omega}$ and $B_{2\omega}$ are linked together by the coupling coefficient $\kappa_{2\omega}$, the decoupled generating equation for $A_{2\omega}$ or $B_{2\omega}$ is a second-order differential equation if $\kappa_{2\omega} \neq 0$, as shown in Eq. (5.13). This second-order differential equation is essentially the

same as that for a driven harmonic oscillator. We will come back to this point in next section. These differences confirm that the condition $\Delta k = \pm\kappa_{2\omega}$ cannot be regarded as a quasi-phase matching condition, but a resonance condition. Therefore, the phenomenon studied in this case is different from those to obtain efficient frequency conversion by using phase-matching methods. We must regard this phenomenon as a resonance effect rather than a QPM effect.

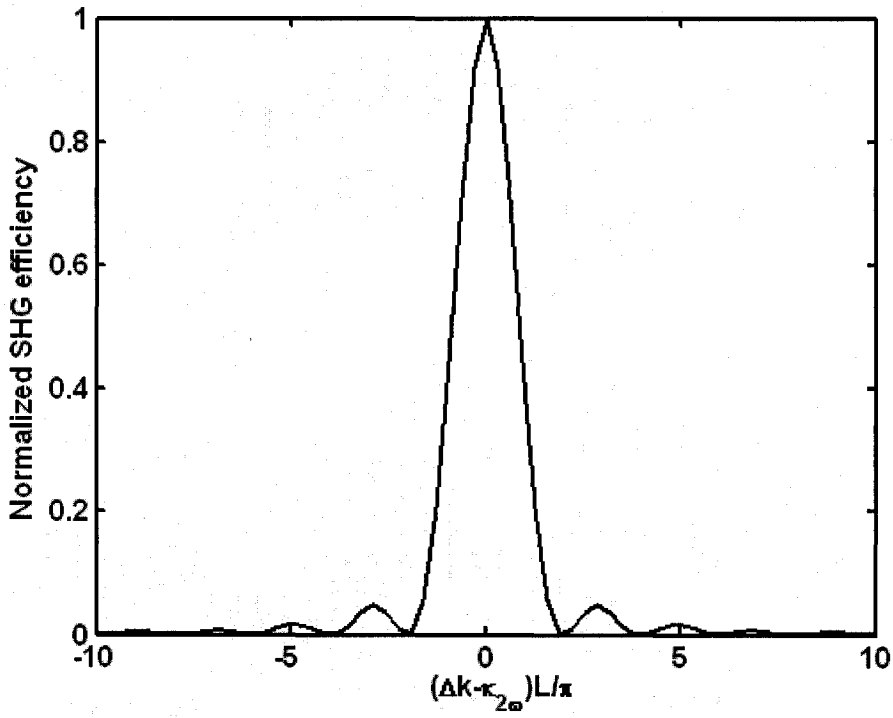

Figure 5.7. Normalized total SHG conversion efficiency versus the detuning of the phase mismatch Δk from the resonance condition that $\Delta k = \kappa_{2\omega}$.

Fig. 5.7 depicts the normalized total SHG conversion efficiency versus the detuning of Δk from the resonance condition that $\Delta k = \kappa_{2\omega}$ with the non-depletion assumption. This curve is similar to that for perfect-matching and QPM systems [1]-[4]. This occurs because the amplitude of SHG is sinusoidally dependent on $\Delta k - \kappa_{2\omega}$ when Δk is close to $\kappa_{2\omega}$, as can be observed by Eq. (5.15). We can also understand this phenomenon as described as follows.

With the definition that $\tilde{A}_{2\omega} = A_{2\omega}\exp(-i\kappa_{2\omega}z)$, Eq. (5.12) is transformed to

$$\frac{d^2\tilde{A}_{2\omega}}{dz^2} + 2i\kappa_{2\omega}\frac{d\tilde{A}_{2\omega}}{dz} = \eta^{2\omega}A_0^2\Delta k\exp(i(\Delta k - \kappa_{2\omega})z) \tag{5.16}$$

Under the condition that $|\Delta k - \kappa_{2\omega}| \to 0$, the term consisting of second-order differential will be much smaller compared with the first-order differential term, we thus obtain

$$\frac{d\tilde{A}_{2\omega}}{dz} = -\frac{i\eta^{2\omega}A_0^2\Delta k}{2\kappa_{2\omega}}\exp(i(\Delta k - \kappa_{2\omega})z) \tag{5.17}$$

The above equation is the same as that for SHG in a single waveguide, and it is readily found that $\kappa_{2\omega} = \Delta k$ results in phase matching. Therefore, in the non-depletion regions the behavior of SHG in directional couplers near the resonance is similar to that for perfect matching and QPM systems. However, neglecting the second-order differential term in Eq. (5.16) is only acceptable when $|\Delta k - \kappa_{2\omega}| \to 0$ and when the non-depletion assumption is used. For example, Eq. (5.17) cannot produce the resonance condition $\kappa_{2\omega} = -\Delta k$, which verifies that we must regard the phenomenon studied in this chapter as a resonance phenomenon, rather than a QPM phenomenon.

Fig. 5.8 shows numerical results with pump depletion for the normalized power of the fundamental wave and the second harmonic wave under the resonance condition $\Delta k = \pm\kappa_{2\omega}$. As the interaction length is sufficiently long, power depletion of the fundamental wave occurs and the conversion efficiency tends to 100%, as is also the case with perfect-matching and quasi-phase matching conditions. However, as the interaction distance increases further, conversion from the second harmonic wave to the fundamental wave occurs and all the power can be transferred back to the fundamental wave. The periodic exchange of power between the fundamental and the second harmonic waves may arise from the properties of the second-order differential equation for driven harmonic oscillator. Although the periodic power exchange between the fundamental and the second harmonic waves can also take place in the intensity-modulation induced QPM, as shown in Fig. 5.6, here, the power can be completely (almost 100% as in fig. 5.8) oscillating between the fundamental and the second harmonic waves. This effect never

happens in the phase-matching and quasi-phase matching when the input field is only the fundamental wave. This phenomenon also demonstrates that the resonance phenomenon studied in this chapter is different from QPM, although the behavior of SHG near the resonance condition is similar to that of QPM systems.

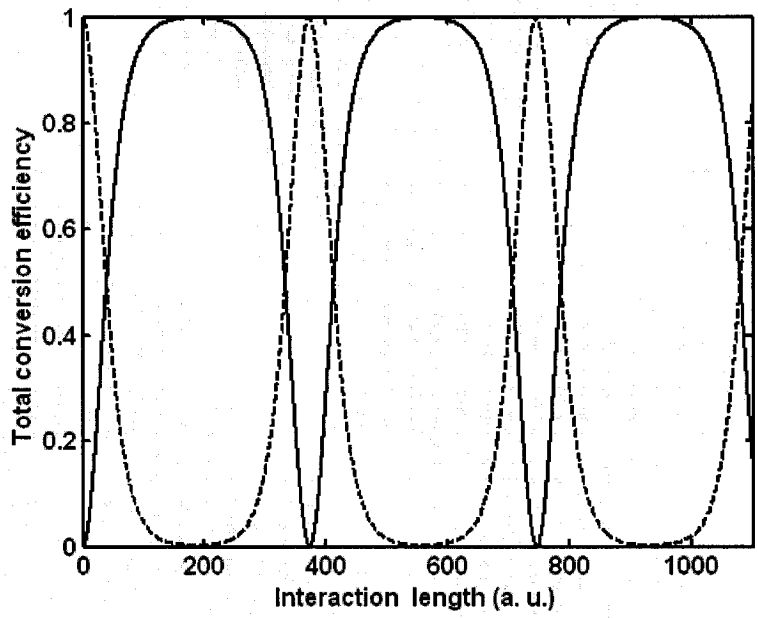

Figure 5.8. Same as Fig. 5.6 but with the conditions that $\Delta k \neq 0$, $\kappa_{2\omega} = \Delta k$ and $\kappa_{\omega} = 0$.

5.2.3 Case of $\kappa_{\omega} \neq 0$ and $\kappa_{2\omega} \neq 0$

We now consider the general case in which both κ_{ω} and $\kappa_{2\omega}$ are nonzero. Again, in the non-depletion region and with the same initial condition as those for the above cases, we have the coupled equations:

$$\begin{cases} \dfrac{dA_{2\omega}}{dz} = -i\kappa_{2\omega}B_{2\omega} - i\eta^{2\omega}A_0^2\cos^2(\kappa_{\omega}z)\exp(i\Delta kz) \\ \dfrac{dB_{2\omega}}{dz} = -i\kappa_{2\omega}A_{2\omega} + i\eta^{2\omega}A_0^2\sin^2(\kappa_{\omega}z)\exp(i\Delta kz) \end{cases} \tag{5.18}$$

The above equations have the following solutions under a non-resonance condition.

$$\begin{aligned}
A_{2\omega} &= C_{A1}\exp(i\kappa_{2\omega}z)+C_{A2}\exp(-i\kappa_{2\omega}z)\\
&\quad +C_{A3}\exp(i\Delta kz)+C_{A4}\exp(i(\Delta k+2\kappa_{\omega})z)+C_{A5}\exp(i(\Delta k-2\kappa_{\omega})z)\\
B_{2\omega} &= C_{B1}\exp(i\kappa_{2\omega}z)+C_{B2}\exp(-i\kappa_{2\omega}z)\\
&\quad +C_{B3}\exp(i\Delta kz)+C_{B4}\exp(i(\Delta k+2\kappa_{\omega})z)+C_{B5}\exp(i(\Delta k-2\kappa_{\omega})z)
\end{aligned} \tag{5.19}$$

where

$$\begin{aligned}
C_{A1} &= -C_{B1} = C\left(-\frac{1}{2}\kappa_{2\omega}^2-\kappa_{2\omega}\Delta k+2\kappa_{\omega}^2-\frac{1}{2}\Delta k^2\right)\\
C_{A2} &= C_{B2} = C\left(\frac{1}{2}\kappa_{2\omega}^2-\frac{1}{2}\Delta k^2\right)\\
C_{A3} &= -C_{B3} = C\left(\frac{1}{2}\kappa_{2\omega}^2+\kappa_{2\omega}\Delta k-2\kappa_{\omega}^2+\frac{1}{2}\Delta k^2\right)\\
C_{A4} &= C_{B4} = C\left(-\frac{1}{4}\kappa_{2\omega}^2+\frac{1}{2}\kappa_{2\omega}\kappa_{\omega}-\frac{1}{2}\kappa_{\omega}\Delta k+\frac{1}{4}\Delta k^2\right)\\
C_{A5} &= C_{B5} = C\left(-\frac{1}{4}\kappa_{2\omega}^2-\frac{1}{2}\kappa_{2\omega}\kappa_{\omega}+\frac{1}{2}\kappa_{\omega}\Delta k+\frac{1}{4}\Delta k^2\right)\\
C &= \frac{\eta^{2\omega}A_0^2}{\kappa_{2\omega}^2\Delta k+\kappa_{2\omega}^3+4\Delta k\kappa_{\omega}^2-\Delta k^2\kappa_{2\omega}-4\kappa_{2\omega}\kappa_{\omega}^2-\Delta k^3}
\end{aligned} \tag{5.20}$$

and under the resonance condition the solutions are:

$$\begin{aligned}
A_{2\omega} &= \frac{\eta^{2\omega}A_0^2\kappa_{2\omega}}{4\left(\kappa_{2\omega}^2-\kappa_{\omega}^2\right)}\exp(-i\kappa_{2\omega}z)-\frac{i\eta^{2\omega}A_0^2}{2}\exp(i\Delta kz)z\\
&\quad -\frac{\eta^{2\omega}A_0^2}{8\kappa_{\omega}+8\kappa_{2\omega}}\exp(i(\Delta k+2\kappa_{\omega})z)+\frac{\eta^{2\omega}A_0^2}{8\kappa_{\omega}-8\kappa_{2\omega}}\exp(i(\Delta k-2\kappa_{\omega})z)\\
B_{2\omega} &= \frac{\eta^{2\omega}A_0^2\kappa_{2\omega}}{4\left(\kappa_{2\omega}^2-\kappa_{\omega}^2\right)}\exp(-i\kappa_{2\omega}z)+\frac{i\eta^{2\omega}A_0^2}{2}\exp(i\Delta kz)z\\
&\quad -\frac{\eta^{2\omega}A_0^2}{8\kappa_{\omega}+8\kappa_{2\omega}}\exp(i(\Delta k+2\kappa_{\omega})z)+\frac{\eta^{2\omega}A_0^2}{8\kappa_{\omega}-8\kappa_{2\omega}}\exp(i(\Delta k-2\kappa_{\omega})z)
\end{aligned} \tag{5.21}$$

for

$$\Delta k = \kappa_{2\omega} \tag{5.22}$$

and

$$\begin{cases} A_{2\omega} = -\dfrac{\eta^{2\omega}A_0^2}{4(\kappa_{2\omega} \mp \kappa_\omega)}\exp(i\kappa_{2\omega}z) \pm \dfrac{\eta^{2\omega}A_0^2}{16\kappa_\omega}\exp(-i\kappa_{2\omega}z) - \dfrac{i\eta^{2\omega}A_0^2}{4}\exp(-i\kappa_{2\omega}z)z \\ + \dfrac{\eta^{2\omega}A_0^2}{4(\kappa_{2\omega} \mp \kappa_\omega)}\exp(i(-\kappa_{2\omega} \pm 2\kappa_\omega)z) \mp \dfrac{\eta^{2\omega}A_0^2}{16\kappa_\omega}\exp(i(-\kappa_{2\omega} \pm 4\kappa_\omega)z) \\ B_{2\omega} = \dfrac{\eta^{2\omega}A_0^2}{4(\kappa_{2\omega} \mp \kappa_\omega)}\exp(i\kappa_{2\omega}z) \pm \dfrac{\eta^{2\omega}A_0^2}{16\kappa_\omega}\exp(-i\kappa_{2\omega}z) - \dfrac{i\eta^{2\omega}A_0^2}{4}\exp(-i\kappa_{2\omega}z)z \\ - \dfrac{\eta^{2\omega}A_0^2}{4(\kappa_{2\omega} \mp \kappa_\omega)}\exp(i(-\kappa_{2\omega} \pm 2\kappa_\omega)z) \mp \dfrac{\eta^{2\omega}A_0^2}{16\kappa_\omega}\exp(i(-\kappa_{2\omega} \pm 4\kappa_\omega)z) \end{cases} \quad (5.23)$$

for

$$\Delta k = \pm 2\kappa_\omega - \kappa_{2\omega} \quad (5.24)$$

Under the non-resonance condition, the expressions in Eq. (5.19) all exhibit oscillatory terms, while under the resonance conditions, the solutions in Eqs. (5.21) and (5.23) contain terms proportional to the interaction distance z. Both the conditions $\Delta k = \kappa_{2\omega}$ and $\Delta k = \pm 2\kappa_\omega - \kappa_{2\omega}$ result in resonance phenomena, rather than QPM. In the following section, we present a model of driven harmonic oscillators to demonstrate the origin of resonance and to predict these resonance conditions.

5.3 Driven harmonic oscillator model

Because the power in each of the two waveguides for an optical wave can oscillate with the propagation length (rather than with time as in a mechanical oscillator), the directional coupler acts equivalently as a harmonic oscillator for the optical wave. As we know, the nonlinear polarization P at the frequency of the generated wave has the form

$$P \propto \exp(i\Delta kz) \quad (5.25)$$

where Δk is the phase mismatch and z is the propagation length. Obviously, the nonlinear polarization is analogous to an external harmonic force applied to the harmonic oscillator. As is well known, a harmonic oscillator driven by an external harmonic force at resonance obtains the largest magnitude of oscillation. A similar resonance phenomenon appears here, and under the resonance condition the power of the generated field can reach very large values. The nonlinear polarization P as expressed by the above equation the driving 'frequency' Δk . On the other hand, if we regard the directional

coupler as a harmonic oscillator for the SHG, the 'frequency' is $\pm\kappa_{2\omega}$. Therefore, the first type of the resonance occurs at

$$\Delta k = \pm\kappa_{2\omega} \tag{5.26}$$

The above resonance condition is exactly that for Eq. (5.15) which is obtained in the case that the intensity modulation for the fundamental wave does not exist. Furthermore, we have learned that the modulation of the fundamental wave results in the phase modification $0, \pm 2\kappa_{\omega} z$ for the nonlinear polarization (see Eq. (5.7)). The 0-phase modification results in the same resonance condition as in Eq. (5.26). On the other hand, the phase modification of $\pm 2\kappa_{\omega} z$ transforms the nonlinear polarization P into a new possible form $P \propto \exp(i(\Delta k \pm 2\kappa_{\omega})z)$. This gives rise to a second set of resonance conditions:

$$\Delta k \pm 2\kappa_{\omega} = \pm\kappa_{2\omega} \text{ or } \Delta k \pm 2\kappa_{\omega} = \mp\kappa_{2\omega} \tag{5.27}$$

The resonance conditions described by Eqs. (5.26-27) explain the origin of those in Eqs. (5.21-24). It is to be noted that the resonance conditions in Eqs. (5.22) and (5.24) are $\Delta k = \kappa_{2\omega}$ and $\Delta k = \pm 2\kappa_{\omega} - \kappa_{2\omega}$, which are a subset of the resonance conditions in Eqs (5.26-27). This may be due to the initial condition by which the input fundamental wave is incident in only the first waveguide. This initial condition cancels some resonance conditions because of some symmetric terms in Eqs. (5.2). A change of the initial condition may produce the complete resonance conditions described by Eqs. (5.26) and (5.27). In addition, we note that the condition $\Delta k = \pm 2\kappa_{\omega}$ for the intensity-modulated induced QPM is just a special solution of Eq. (5.27) with the condition that $\kappa_{2\omega} = 0$. This implies that the intensity-modulated induced QPM can be regarded as a resonance phenomenon for the directional coupler having a zero modulation frequency for the second harmonic wave.

In Fig. 5.9, we plot the maximum power of SHG versus the coupling coefficient $\kappa_{2\omega}$ from the direct numerical computation of Eqs. (5.2). The maximum power of SHG is sought by numerically solving the amplitudes $A_{2\omega}(z)$ and $B_{2\omega}(z)$ and then finding the maximum value of $|A_{2\omega}(z)|^2 + |B_{2\omega}(z)|^2$ at a particular position z. The appearance of the

resonance peaks are exactly those we obtained in the above analytical solutions. By this way, we have demonstrated how the resonance conditions can be obtained by numerical simulation directly from Eqs. (5.2).

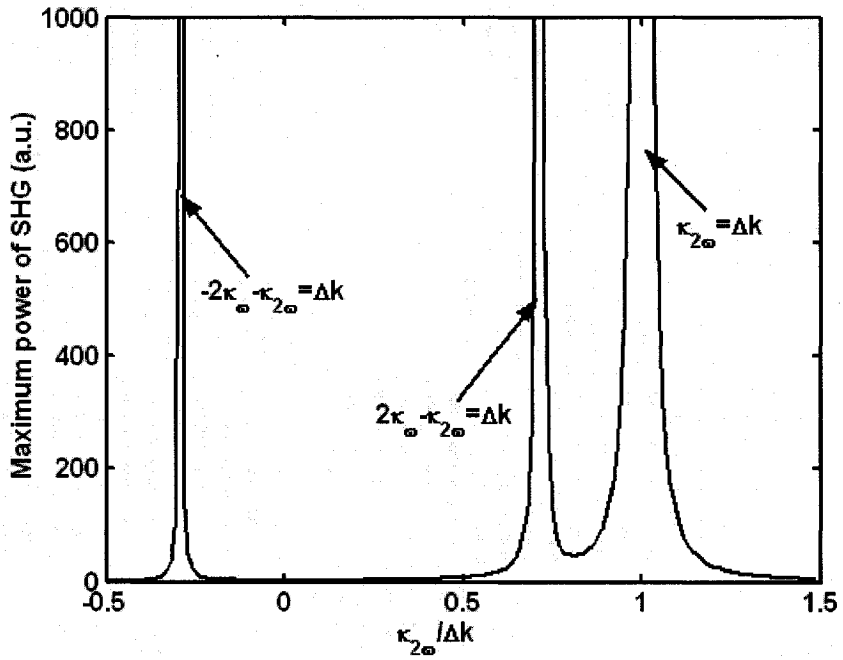

Figure 5.9. Maximum SHG power as a function of $\kappa_{2\omega}/\Delta k$. The maximum SHG power for a particular $\kappa_{2\omega}/\Delta k$ is obtained by computing the SHG power versus the interaction length and then seeking the maximum value of the SHG power. Here, the SHG power is the total power in the two waveguides. In this figure, we use the condition that $\kappa_{\omega} = 1.2\kappa_{2\omega}$.

5.4 Effects of waveguide loss

In a real system, however, there is always loss which must be included in the calculation. In Eqs. (5.2), we have incorporated the loss terms in the coupled equations. Nevertheless, the analytical solutions are difficult to obtain even in the non-depletion region. The numerical approach used to calculate the resonance conditions from Eqs. (5.2) as obtained in Fig. 5.9 can be extended to include loss. We have found that if the loss α is small compared with Δk, the resonance condition of Eqs (5.26-5.27) will be

not altered. This finding is also supported by considering the resonance of a damped driven mechanical harmonic oscillator. In practice, the waveguide loss is usually less than $10^{-2}cm^{-1}$ which is sufficiently small compared with the phase mismatch (in the order of $10^{1}cm^{-1}$). Therefore, the resonance conditions will be the same as those of lossless waveguides, as shown in Fig. 5.10. However, the maximum conversion efficiency is dramatically affected by the waveguide losses. From Fig. 5.10, we can see that with larger loss, the maximum power of SHG decreases. In Fig. 5.11, we plot the conversion efficiency as a function of the interaction length with the presence of the waveguide loss. As can be observed, there is an optimal interaction length which results in the maximum conversion efficiency. The optimal interaction length decreases with increasing loss. Therefore in a real system the interaction length must be carefully designed to obtain maximum power conversion.

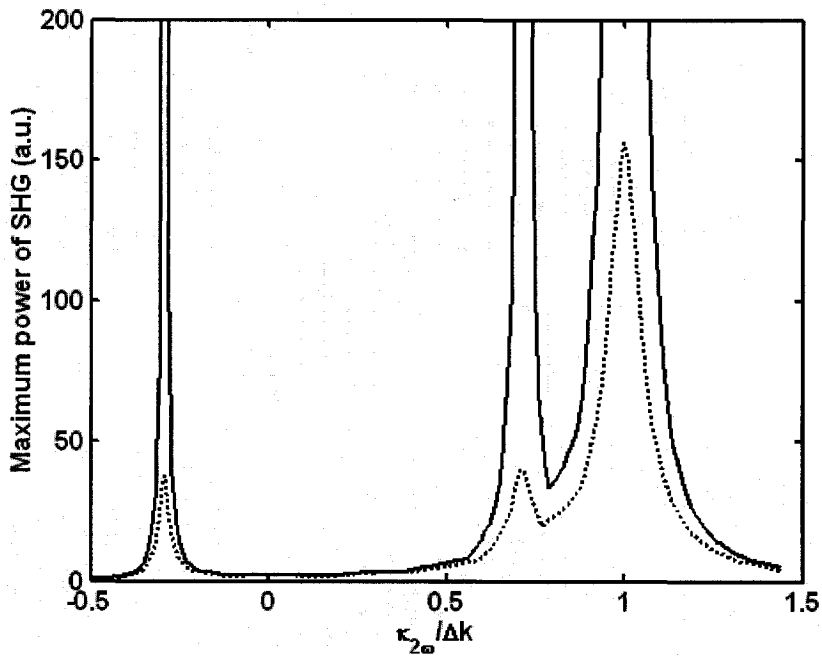

Figure 5.10. Same as Fig. 5.9 but we include the waveguide loss in this figure. The loss terms $\alpha_i^{\omega_j}$ (see Eqs. (5.2)) are $10^{-4}\Delta k$ for the solid line and $10^{-2}\Delta k$ for the dotted line.

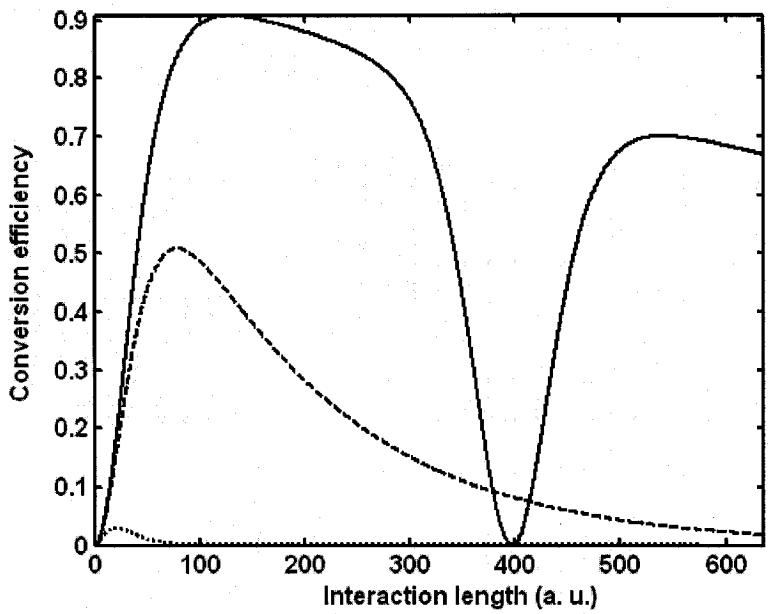

Figure 5.11. SHG conversion efficiency versus the interaction length in the presence of waveguide loss. The loss terms $\alpha_i^{\omega_j}$ (see Eqs. (5.2)) are $10^{-4}\Delta k$ for the solid line, $10^{-3}\Delta k$ for the dashed line, and $10^{-2}\Delta k$ for the dotted line.

5.5 Significance of the proposed theory and experimental consideration

The proposed theory not only has fundamental theoretical significance for nonlinear optics but also has both the application advantages of frequency conversion in waveguides and in QPM systems. The very small beam size which can be obtained in waveguide structures can result in low pumping power. In principle, a low attenuation can be achieved in waveguides, which results in long interaction distances. Similar to the technique of QPM, the resonance condition can be found in principle for any converted wavelength if the directional coupler structure is properly designed. Furthermore, the proposed method overcomes some of the main limitations for other phase-matching techniques. One can use fundamental modes for both the pumping wave and the generated wave and thus increase the spatial overlap between these two modes. Other techniques in a single waveguide structure, such as modal dispersion phase matching and

anomalous-dispersion phase matching, usually suffer from the small overlap between the modes of the pumping and the generated waves. At the same time, spatially periodic poling is not required, which eliminates many of the fabrication difficulties of the QPM systems.

Up to now, we have not considered the practicality of achieving resonance condition. The phase mismatch Δk is mainly determined by the waveguide structure, while the coupling coefficient κ can be controlled by the waveguide separation. The resonance effect can be designed in principle for any converted wavelength. If we take a typical value of wavelength at $\lambda \approx 1\mu m$ and the refractive index difference as $n_{2\omega} - n_{\omega} \approx 0.01$, we obtain $\Delta k \approx 10^{-1}\mu m^{-1}$. While the usual value of $\kappa_{2\omega}$ for a low contrast waveguide directional coupler may be about $10^{-3}\mu m^{-1}$ [12][13]. It is found that the phase mismatch and the coupling coefficient have about two-order magnitude difference. However, with a careful design of the directional coupler, the resonant condition is indeed possible in experiments. For instance, in asymmetric twin waveguides for optical integration, a coupling coefficient $0.2\mu m^{-1}$ can be designed with high-index-contrast waveguides [16]. Other promising directional couplers with enhanced coupling coefficients have been also proposed in photonic crystal waveguide structures [17]-[19], in intermediate-mode-assisted directional coupler structures [20], in directional couplers utilizing a left-handed material [21], and in transverse Bragg resonance waveguide structures [22]. In Ref. [17], Tokushima and Yamada reported a coupling length about 20μm in a photonic crystal waveguide directional coupler fabricated in a silicon-on-insulator wafer. A coupling length of 7μm was demonstrated in a directional coupler with a coupling-strength control defect based on a two-dimensional photonic-crystal slab waveguide [19]. A transfer length of less than 100μm has also been demonstrated in a directional coupler with an intermediate layer made by a left-handed material (a material with negative refractive index) [21]. In addition, the coupling coefficients can be enhanced by a factor of five in transverse Bragg resonance waveguide directional couplers [22]. The figures obtained for the coupling coefficients in the above references already have the same magnitude as the phase mismatch. Therefore, the design of a suitable directional coupler for our theory is indeed feasible.

While the proposed theory is based on nonlinear effects in a directional coupler, the experimental challenge is mainly in waveguide fabrication since the directional coupler consists of two close waveguides. There has been a wide range of activities in second harmonic generation in waveguide systems. The materials used in this area are mainly nonlinear optical crystals, polymers, and semiconductors. The nonlinear optical crystals, such as lithium niobate and KTP crystals, are the conventional and commercial nonlinear materials. However, they are hard to fabricate into waveguide structure, much harder to fabricate into a directional coupler. Nonlinear optical polymers have promising advantages of high nonlinearity, easy waveguide fabrication, and flexible waveguide design [5]-[7][23][24]. However, nonlinear polymer waveguides exhibit high optical loss because of the material absorption and imperfect waveguide fabrication. This will limit the effective waveguide length and consequently, the conversion efficiency will be low. Furthermore, III-V semiconductor and its alloy semiconductors may be promising materials for the possible experiments. They possess huge nonlinear coefficients which can be about one order of magnitude greater efficiency than the commonly used materials. Alloy semiconductors can easily be used to construct waveguide structures. We will pursue this further in Chapter 7.

5.6 Understanding resonance conditions as phase matching between supermodes

In the previous sections, we have shown that efficient second harmonic generation occurs under some resonance conditions in waveguide directional couplers when the coupled mode theory is applied. We also demonstrated that under the resonance conditions, the behavior of second harmonic generation is essentially the same as those under perfect matching and quasi-phase matching conditions in the non-depletion region. Furthermore, the oscillation of an optical wave in directional couplers can be also explained by the propagation of supermodes of directional couplers [12]. These indicate that the resonance conditions are possibly explained by phase matching between the supermodes of directional couplers.

5.6.1 Supermodes of directional couplers

Since directional couplers are z-invariant, we can regard them as compound waveguide structures or double-core waveguide structures. Rather than applying the coupled mode theory to directional couplers, we are able to obtain the propagating eigenmodes of the compound structures, which are normally called supermodes of directional couplers. Similar to multi-mode waveguides, there exist an even and an odd mode for the compound structure. If we assume the two individual waveguides in a directional coupler are identical, the mode patterns for even and odd modes are similar to those shown in Fig. 5.12. As the two individual waveguides are separated enough, most of the energy of the even or odd mode is confined in the two core regions, as shown in Fig. 5.12. The sum and difference of the even and odd modes of the compound structure results in the mode in the individual waveguides, as shown in Fig. 5.13. At the input end, say at $z = 0$, the light is incident into one waveguide, which implies that the directional coupler is excited with a field distribution that can be expressed as the sum or difference of the even and odd modes of the compound structure. Suppose the initial field is the sum of the even and odd modes, the field propagates in the directional coupler following the equation

$$\vec{E}(\vec{r}) = \vec{E}_{even}(x,y)e^{-i\beta_{even}z} + \vec{E}_{odd}(x,y)e^{-i\beta_{odd}z} \tag{5.28}$$

It can be easily found that

$$\begin{aligned} &\vec{E}(z=0) = \vec{E}_{even}(x,y) + \vec{E}_{odd}(x,y) \\ &\vec{E}\left(z \equiv L = \frac{\pi}{\beta_{even} - \beta_{odd}}\right) = C\left(\vec{E}_{even}(x,y) - \vec{E}_{odd}(x,y)\right) \end{aligned} \tag{5.29}$$

Instead of adding to each other at $z = 0$, the even and odd modes form the difference field at $L = \dfrac{\pi}{\beta_{even} - \beta_{odd}}$ because of the slight difference of phase velocities of these two modes. While the sum of the two modes represents the field in the first waveguide, the difference represents the field in the second waveguide. Therefore, the light has been transferred to the second waveguide at $L = \dfrac{\pi}{\beta_{even} - \beta_{odd}}$ which is called the transfer length of the directional coupler. From the relationship $L = \dfrac{\pi}{2\kappa}$ [13], one can find the

relationship between the coupling coefficient κ and the propagation constants β_{even} and β_{odd}

$$\kappa = \frac{\beta_{even} - \beta_{odd}}{2} \tag{5.30}$$

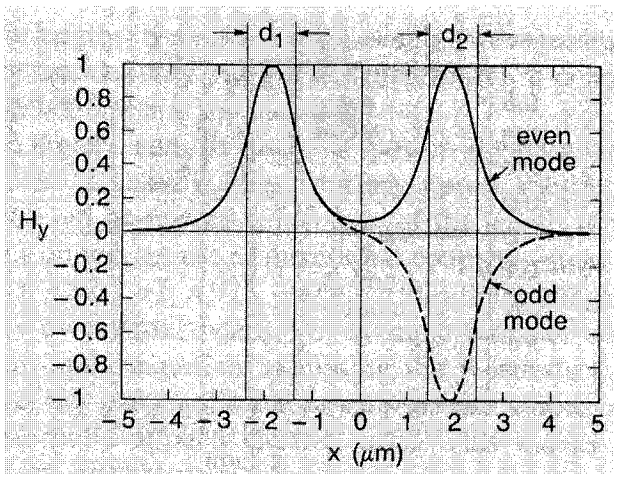

Figure 5.12. Field distribution of the even TM mode and the odd TM mode of a slab directional coupler (Figure from Ref. [25]). d_i is the core thickness of individual waveguides.

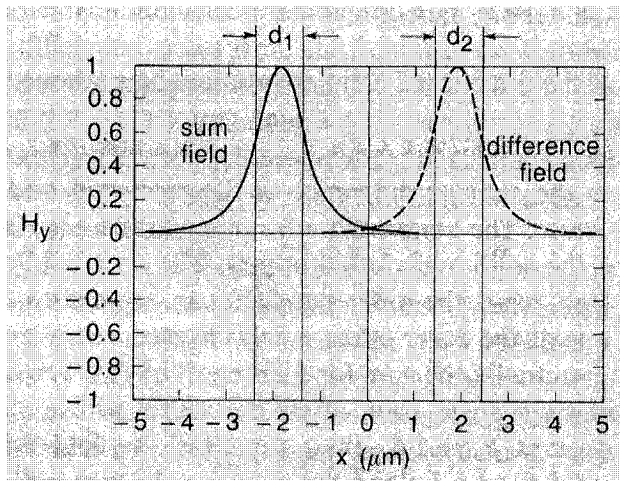

Figure 5.13. Sum (solid line) and difference (dotted line) fields of the even and odd directional coupler modes shown in Fig. 5.12 (Figure from Ref. [25]). It is clear that the sum represents the modal field in the first waveguide, and the different represents that in the second waveguide.

The next step is to determine how the propagation constants β_{even} and β_{odd} of the compound structure are related to those of the individual waveguides. The solution for the case of identical individual waveguides is

$$\beta = \frac{\beta_{even} + \beta_{odd}}{2} \tag{5.31}$$

where β is the propagation constant in the individual waveguides [12].

5.6.2 Phase matching between Supermodes

From Eqs. (5.30) and (5.31), we obtain

$$\begin{aligned} \Delta k = \beta_{2\omega} - 2\beta_{\omega} &= \frac{\beta_{even}^{2\omega} + \beta_{odd}^{2\omega}}{2} - 2 \times \frac{\beta_{even}^{\omega} + \beta_{odd}^{\omega}}{2} \\ \kappa_{2\omega} &= \frac{\beta_{even}^{2\omega} - \beta_{odd}^{2\omega}}{2} \\ \kappa_{\omega} &= \frac{\beta_{even}^{\omega} - \beta_{odd}^{\omega}}{2} \end{aligned} \tag{5.32}$$

where $\beta_{even}^{2\omega}$ and $\beta_{odd}^{2\omega}$ are the propagation constants of the even mode and the odd mode of the directional coupler at the frequency of second harmonic generation, respectively, and β_{even}^{ω} and β_{odd}^{ω} are for those at the frequency of pump wave. Substitution of Eq. (5.32) into the resonance condition Eq. (5.22) leads to

$$\beta_{odd}^{2\omega} - \beta_{even}^{\omega} - \beta_{odd}^{\omega} = 0 \tag{5.33}$$

It is clear that the resonance condition Eq. (5.22) can be interpreted by the phase-matching between the odd mode of the directional coupler for SHG and the even and odd modes of the fundamental wave. Similarly, the resonance conditions expressed by Eq. (5.24) can be described by

$$\beta_{even}^{2\omega} - 2\beta_{even}^{\omega} = 0 \tag{5.34}$$

$$\beta_{even}^{2\omega} - 2\beta_{odd}^{\omega} = 0 \tag{5.35}$$

Once again, we see that the resonance conditions can be expressed by the phase matching between the supermodes of the compound structure.

With these understanding, we can also explain the phenomena in the depletion region. As we have discussed, under the resonance condition Eq. (5.22), the total conversion

efficiency tends to 100%, while under the resonance condition Eq. (5.24), the total conversion efficiency tends to 50%. This is due to the fact that we input the fundamental wave into the first waveguide, which implies that half of the total pump energy is carried by the even mode and half is carried by the odd mode. From Eq. (5.33), the resonance condition Eq. (5.22) represents the case that the SHG energy comes from those of both the even and the odd mode. Hence, the final conversion efficiency can tend to 100% in the depletion region. Instead, the resonance condition Eq. (5.24) which is equivalent to the phase-matching conditions Eq. (5.34) and Eq. (5.35) are corresponding to the cases that only the even or odd modes plays the role in the frequency conversion. Therefore, only 50% can be obtained in the depletion region.

Another phenomenon in the depletion region we have seen is that even under the resonance condition Eq. (5.22), the energy of SHG can convert back to that of the fundamental wave after the total conversion efficiency gets close to 100%. This phenomenon does not occur in the cases of quasi-phase matching and perfect phase matching studied before. This is due to the fact that the coupled equation in Eq. (5.2) includes all possible conversion between the supermodes of the compound structure. For example, under the resonance condition Eq. (5.22), the conversion from the even (odd) mode of the fundamental wave to the even mode of SHG can take place under non-matching condition. Such conversion will trigger the back conversion from SHG to the fundamental wave after the total conversion obtains its maximal value.

Nevertheless, the understanding that the resonance conditions can be explained by the phase matching between supermodes does not diminish the application advantages of the proposed theory. For example it is possible to realize Eq. (5.33) where the first TE mode (β_{even}^{ω}) and the second TE mode (β_{odd}^{ω}) are converted to the second TM mode ($\beta_{odd}^{2\omega}$). In this case, since the power of both SHG and the fundamental wave are confined in two core regions, the field overlap between SHG and the fundamental wave can be very large, which will increase the conversion efficiency. Another advantage is the generation of multiple wavelengths by using Eqs. (5.33)-(5.35) at the same time. Since there is only a slight difference between the effective indices of the even and odd modes, the resonance wavelengths for Eqs. (5.33)-(5.35) are very close. We will come back to this point in

Chapter 7. Furthermore, we have to stress that by using the phase matching among supermodes, one normally considers only one possible conversion process and ignores other different conversion processes (which result from the conversion among different supermodes). This may be not accurate enough in some cases. Therefore, using coupled equations (5.2) and the concept of resonance phenomenon may have more advantages, especially in the depletion-region.

5.7 Conclusions

In this chapter, we theoretically investigate second harmonic generation in waveguide directional couplers. We demonstrate that a resonance phenomenon occurs due to the resonance between the intensity modulation of the generated wave by the directional coupler and the harmonic nonlinear polarization. We also study in some detail an intensity-modulation induced QPM which occurs due to the intensity modulation of the pump wave in the directional coupler. The resonance phenomenon has some similar characteristics to both perfect phase-matching and to QPM: (1) it can be used to generate high-efficiency nonlinear frequency conversion; and (2) in the non-depletion region, the dominant term of the amplitude for the second harmonic wave is proportional to the interaction length. Nevertheless, some interesting phenomena are observed in the pump depletion region: (1) in some situations, the maximal conversion efficiency is 50%, rather than 100% as studied previously in QPM systems, (2) under the resonance conditions, a periodic power exchange between the second harmonic and the fundamental waves take places even when the input field is only the fundamental wave. We also point out that the intensity-modulation induced QPM also exhibit the periodic power exchange when the maximal conversion efficiency is 50%.

If we regard the directional coupler as a harmonic oscillator for the generated wave, the nonlinear polarization becomes a harmonic force applied on this oscillator. Because the natural frequency of the harmonic oscillator is the coupling coefficient κ and that of the nonlinear polarization is the phase mismatch Δk, one readily sees that the resonance conditions are $\kappa = \pm\Delta k$. Since the directional coupler is also periodically modulating the pump waves, phase compensations appear for the nonlinear polarization (which is the direct reason for the intensity-modulation induced QPM). This brings out some new

resonance conditions which usually include the addition and subtraction of the coupling coefficients for all waves and the phase mismatch. This view of our proposed new phenomenon helps to analytically obtain the resonance conditions without complicated theoretical derivations.

The proposed technique is an alternative means to those of the perfect phase-matching and QPM. Efficient nonlinear frequency conversion was originally observed in bulk crystals, then in single waveguides and now appears to be possible in coupled waveguides. Second harmonic generation was firstly realized in nonlinear crystals, and the birefringence of the crystals was used to realize the perfect phase-matching. When a waveguide structure is used, more phase-matching techniques can be realized due to the mode properties of the waveguide. QPM can be implemented in both bulk materials and waveguide structures, and it can be realized for any converted wavelength and by isotropic nonlinear materials. Our theory in this chapter shows that the directional coupler can provide us with the same advantages of QPM systems, but has simpler structure.

In summary, we have presented a detailed theory for SHG in a waveguide directional coupler. We have discussed the origin of the resonance phenomenon using a driven harmonic oscillator model. Pump depletion and waveguide loss are included in the coupled equations and their effects are shown by the numerical calculation. The proposed technique has not only fundamental theoretical significance but also many application advantages. The possible experimental realization of this theory is also discussed. We also point out that the proposed theory can be understood by phase matching between the supermodes of compound structures.

References

[1] R. W. Boyd, *Nonlinear optics*, (Academic Press Inc., 2003).

[2] J. A. Armstrong, N. Bloembergen, J. Ducuing, and P. S. Pershan, "Interactions between light waves in a nonlinear dielectric," *Phys. Rev.*, vol. 127, pp. 1918-1939, 1962.

[3] V. Berger, "Nonlinear photonic crystals," *Phys. Rev. Lett.*, vol. 81, pp. 4136-4139, Nov. 1998.

[4] M. M. Fejer, G. A. Magel, D. H. Jundt, and R. L. Byer, "Quasi-phase-matched second harmonic generation – tuning and tolerance," *IEEE J. Quantum Electron.*, vol. 28, pp. 2631-2654, Nov. 1992.

[5] G. L. J. A. Rikken, C. J. E. Seppen, E. G. J. Staring, and A. H. J. Venhuizen, "Efficient modal dispersion phase-matched frequency-doubling in poled polymer waveguides," *Appl. Phys. Lett.*, vol. 62, pp. 2483-2485, May 1993.

[6] M. Jager, G. I. Stegeman, G. R. Mohlmann, M. C. Flipse, and M. B. J. Diemeer, "Second harmonic generation in polymeric channel waveguides using modal dispersion," *Electron. Lett.*, vol. 32, pp. 2009-2010, Oct. 1996.

[7] T. C. Kowalczyk, K. D. Singer, and P. A. Cahill, "Anomalous-dispersion phase-matched 2nd-harmonic generation in a polymer waveguide," *Opt. Lett.*, vol. 20, pp. 2273-2275, Nov. 1995.

[8] P. K. Tien, R. Ulrich, and R. J. Martin, "Optical second harmonic generation in form of coherent Cerenkov radiation from a thin-film waveguide," *Appl. Phys. Lett.*, vol. 17, pp. 447-449, 1970.

[9] D. Fluck, T. Pliska, P. Gunter, L. Beckers, and C. Buchal, "Cerenkov-type second-harmonic generation in KNbO3 channel waveguides," *IEEE J. Quantum Electron.*, vol. 32, pp. 905-916, Jun. 1996.

[10] G. Assanto, G. Stegeman, M. Sheik-Bahae, and E. V. Stryland, "All-optical switching devices based on large nonlinear phase shifts from second harmonic generation," *Appl. Phys. Lett.*, vol. 62, pp. 1323-1325, Mar. 1993.

[11] A. Yariv, "Coupled-mode theory for guided-wave optics," *IEEE J. Quantum Electron.*, vol. 9, pp. 919-933, 1973.

[12] A. Yariv, *Optical Electronics in Modern Communications*, (Oxford University Press, 1997).

[13] K. Okamoto, *Fundamentals of Optical Waveguide*, (Academic Press, 2000).

[14] X. G. Huang and M. R. Wang, "A novel quasi-phase-matching frequency doubling technique," *Opt. Commun.*, vol. 150, pp. 235-238, May 1998.

[15] K. C. Rustagi, S. C. Mehendale, and S. Meenakshi, "Optical frequency conversion in quasi-phase-matched stacks of nonlinear crystal," *IEEE J. Quantum Electron.*, vol. 18, pp. 1029-1041, Jun. 1982.

[16] F. Xia, V. M. Menon, and S. R. Forrest, "Photonic integration using asymmetric twin-waveguide (ATG) technology: part I---concepts and theory," *IEEE J. Selected Topics Quantum Electron*, vol. 11, pp. 17-29, 2005.

[17] M. Tokushima and H. Yamada, "Photonic crystal line defect waveguide directional coupler," *Electron. Lett.*, vol. 37, pp. 1454-1455, Nov. 2001.

[18] A. Martinez, F. Cuesta, and J. Marti, "Ultrashort 2-D photonic crystal directional couplers," *IEEE Photon. Tech. Lett.*, vol. 15, pp. 694-696, May 2003.

[19] Y. Sugimoto, Y. Tanaka, N. Ikeda, T. Yang, H. Nakamura, K. Asakawa, K. Inoue, T. Maruyama, K. Miyashita, K. Ishida, and Y. Watanabe, "Design, fabrication, and characterization of coupling-strength-controlled directional coupler based on two-dimensional photonic-crystal slab waveguides," *Appl. Phys. Lett.*, vol. 83, pp. 3236-3238, Oct. 2003.

[20] Vorobeichik, E. Narevicius, G. Rosenblum G, M. Orenstein, and N. Moiseyev, "Electromagnetic realization of orders-of-magnitude tunneling enhancement in a double well system," *Phys. Rev. Lett.*, vol. 90, pp. 176806, May 2003.

[21] S. H. Xiao, L. F. Shen, and S. L. He, "A novel directional coupler utilizing a left-handed material," *IEEE Photon. Tech. Lett.*, vol. 15, pp. 694-696, Jan. 2003.

[22] W. Liang, Y. Xu, J. M. Choi, A. Yariv, and W. Ng, "Transverse Bragg-resonant enhancement of modulation and switching," *IEEE Photon. Tech. Lett.*, vol. 16, pp. 2236-2238, Oct. 2004.

[23] G. I. Stegeman *et al.*, Guided-wave Optoelectronics: Device Characterization, Analysis, and Design, *Proceedings of the 4th WRI International Conference on Guided Wave Optoelectronics*, edited by T. Tamir, H. Bertoni, and G. Griffel, pp. 371-391, Plenum, New York (1995).

[24] W. Wirges, S. Yilmaz, W. Brinker, S. Bauer-Gogonea, S. Bauer, M. Jager, G. I. Stegeman, M. Ahlheim, M. Stahelin, B. Zysset, F. Lehr, M. Diemeer, and M. C. Flipse, "Polymer waveguides with optimized overlap integral for modal dispersion phase-matching," *Appl. Phys. Lett.*, vol. 70, pp. 3347-3349, Jun. 1997.

[25] D. Marcuse, *Theory of dielectric optical waveguides*, (Academic Press, 1991).

CHAPTER 6 OTHER NONLINEAR FREQUENCY CONVERSION EFFECTS IN DIRECTIONAL COUPLERS

In the previous chapter, we investigated SHG both analytically (in the non-depletion region) and numerically in waveguide directional couplers. In this chapter, we consider other possible nonlinear effects, including third-harmonic generation, sum-frequency generation and difference-frequency generation. The theoretical method to deal with these effects is essentially the same as that for SHG in the previous chapter. Therefore, we shall not present detailed theory for every nonlinear effect; instead, we focus on the coupled equations and resonance conditions.

As discussed in the previous chapter, the model of a driven harmonic oscillator can explain the origin of the resonance and readily give the resonance conditions. If the intensity modulation for all waves but the generated wave does not exist, the resonance condition is $\Delta k = \pm\kappa$ (κ is the coupling coefficient for the generated wave) because the nonlinear polarization P has the form $P \propto \exp(i\Delta kz)$. In general, the modulation of both the pump and the generated wave occurs and the resonance conditions should be carefully calculated after the consideration of the possible phase compensation by the modulation of other waves rather than the generated wave. In the following, we will discuss the resonance condition for other nonlinear frequency conversion effects. Again, we are using the non-depletion assumption and assume that all the pump wave(s) are incident in the first waveguide but not the second waveguide. Furthermore, we assume that the two waveguides are identical.

6.1 Third-harmonic generation

Following a similar procedure for second-order harmonic, we obtain the coupled equations:

$$\begin{cases} \dfrac{dA_{3\omega}}{dz} = -i\kappa_{3\omega}B_{3\omega} - i\eta^{3\omega}A_{\omega}^{3}\exp(i\Delta kz) \\ \dfrac{dB_{3\omega}}{dz} = -i\kappa_{3\omega}A_{3\omega} - i\eta^{3\omega}B_{\omega}^{3}\exp(i\Delta kz) \end{cases} \tag{6.1}$$

With the same notation, $\kappa_{3\omega}$ is the mode-coupling coefficient of the directional coupler for the third harmonic wave [1]-[3]. Furthermore,

$$\Delta k = k_{3\omega} - 3k_{\omega} \tag{6.2}$$

With the non-depletion assumption for the fundamental wave, we have

$$\begin{cases} \dfrac{dA_{3\omega}}{dz} = -i\kappa_{3\omega}B_{3\omega} - i\dfrac{1}{8}\eta^{3\omega}A_0^3\left[e^{iz(3\kappa_{\omega}+\Delta k)} + 3e^{iz(\kappa_{\omega}+\Delta k)} + 3e^{iz(-\kappa_{\omega}+\Delta k)} + e^{iz(-3\kappa_{\omega}+\Delta k)}\right] \\ \dfrac{dB_{3\omega}}{dz} = -i\kappa_{3\omega}A_{3\omega} + i\dfrac{1}{8}\eta^{3\omega}A_0^3\left[e^{iz(3\kappa_{\omega}+\Delta k)} - 3e^{iz(\kappa_{\omega}+\Delta k)} + 3e^{iz(-\kappa_{\omega}+\Delta k)} - e^{iz(-3\kappa_{\omega}+\Delta k)}\right] \end{cases} \tag{6.3}$$

We observe that in the bracket in the right-hand sides of the above equations, the driving 'frequencies' for the exponential terms are: $\pm\kappa_{\omega} + \Delta k$ and $\pm 3\kappa_{\omega} + \Delta k$. We can thus obtain the following possible resonance conditions from the above equations:

$$\pm\kappa_{\omega} + \Delta k = \pm\kappa_{3\omega} \text{ or } \pm\kappa_{\omega} + \Delta k = \mp\kappa_{3\omega} \tag{6.4}$$

and

$$\pm 3\kappa_{\omega} + \Delta k = \pm\kappa_{3\omega} \text{ or } \pm 3\kappa_{\omega} + \Delta k = \mp\kappa_{3\omega} \tag{6.5}$$

Among the above resonant conditions, $-3\kappa_{\omega} + \Delta k = \kappa_{3\omega}$ is the easiest condition to be realized in experiment since usually $\Delta k > \kappa_{\omega}, \kappa_{3\omega} > 0$.

6.2 Sum-frequency generation

The process of sum-frequency generation involves two input monochromatic beams at frequency ω_1 and ω_2 and the generated wave at frequency $\omega_3 = \omega_1 + \omega_2$. We treat a simpler case where the two applied fields are strong and un-depleted [1]. Therefore, the presence of the new generated wave will not affect the applied fields at frequency ω_1 and ω_2. The coupled-amplitude equations reduce to a simpler set for two identical waveguides:

$$\begin{cases} \dfrac{dA_{\omega_3}}{dz} = -i\kappa_{\omega_3}B_{\omega_3} - i\eta^{\omega_3}A_{\omega_1}A_{\omega_2}\exp(i\Delta kz) \\ \dfrac{dB_{\omega_3}}{dz} = -i\kappa_{\omega_3}A_{\omega_3} - i\eta^{\omega_3}B_{\omega_1}B_{\omega_2}\exp(i\Delta kz) \end{cases} \tag{6.6}$$

with the notation

$$\Delta k = k_{\omega_3} - k_{\omega_1} - k_{\omega_2} \tag{6.7}$$

Once again, with the non-depletion assumption for the both pumps, we get

$$\begin{cases} \dfrac{dA_{\omega_3}}{dz} = -i\kappa_{\omega_3} B_{\omega_3} - i\dfrac{1}{4}\eta^{\omega_3} A_0^{\omega_1} A_0^{\omega_2} \left(e^{i(\kappa_{\omega_1}+\kappa_{\omega_2}+\Delta k)z} + e^{i(-\kappa_{\omega_1}+\kappa_{\omega_2}+\Delta k)z} + e^{i(\kappa_{\omega_1}-\kappa_{\omega_2}+\Delta k)z} + e^{i(-\kappa_{\omega_1}-\kappa_{\omega_2}+\Delta k)z} \right) \\ \dfrac{dB_{\omega_3}}{dz} = -i\kappa_{\omega_3} A_{\omega_3} - i\dfrac{1}{4}\eta^{\omega_3} A_0^{\omega_1} A_0^{\omega_2} \left(e^{i(\kappa_{\omega_1}+\kappa_{\omega_2}+\Delta k)z} - e^{i(-\kappa_{\omega_1}+\kappa_{\omega_2}+\Delta k)z} - e^{i(\kappa_{\omega_1}-\kappa_{\omega_2}+\Delta k)z} + e^{i(-\kappa_{\omega_1}-\kappa_{\omega_2}+\Delta k)z} \right) \end{cases} \tag{6.8}$$

Directly, we obtain the following possible resonant conditions from the above equations:

$$\begin{aligned} &\pm\kappa_{\omega_1} \pm \kappa_{\omega_2} + \Delta k = \pm\kappa_{\omega_3} \text{ or } \pm\kappa_{\omega_1} \pm \kappa_{\omega_2} + \Delta k = \mp\kappa_{\omega_3} \\ &\text{or } \pm\kappa_{\omega_1} \mp \kappa_{\omega_2} + \Delta k = \pm\kappa_{\omega_3} \text{ or } \pm\kappa_{\omega_1} \mp \kappa_{\omega_2} + \Delta k = \mp\kappa_{\omega_3} \end{aligned} \tag{6.9}$$

6.3 Difference-frequency generation

Let us consider the situation in which optical waves at frequencies ω_1 and ω_2 interact in a lossless nonlinear optical medium to generate an output field at the difference frequency $\omega_3 = \omega_1 - \omega_2$ [1]. The coupled-amplitude equations in this case are:

$$\begin{cases} \dfrac{dA_{\omega_3}}{dz} = -i\kappa_{\omega_3} B_{\omega_3} - i\eta^{\omega_3} A_{\omega_1} A_{\omega_2}^* \exp(i\Delta kz) \\ \dfrac{dB_{\omega_3}}{dz} = -i\kappa_{\omega_3} A_{\omega_3} - i\eta^{\omega_3} B_{\omega_1} B_{\omega_2}^* \exp(i\Delta kz) \end{cases} \tag{6.10}$$

with the notation

$$\Delta k = k_{\omega_3} - k_{\omega_1} + k_{\omega_2} \tag{6.11}$$

We assume that both the ω_1 and ω_2 waves are strong and the ω_1 wave is not depleted by the generation of the difference-frequency signal. We find that the equations are:

$$\begin{cases} \dfrac{dA_{\omega_3}}{dz} = -i\kappa_{\omega_3} B_{\omega_3} - i\dfrac{1}{4}\eta^{\omega_3} A_0^{\omega_1} \left(A_0^{\omega_2}\right)^* \left(e^{i(\kappa_{\omega_1}+\kappa_{\omega_2}+\Delta k)z} + e^{i(-\kappa_{\omega_1}+\kappa_{\omega_2}+\Delta k)z} + e^{i(\kappa_{\omega_1}-\kappa_{\omega_2}+\Delta k)z} + e^{i(-\kappa_{\omega_1}-\kappa_{\omega_2}+\Delta k)z} \right) \\ \dfrac{dB_{\omega_3}}{dz} = -i\kappa_{\omega_3} A_{\omega_3} + i\dfrac{1}{4}\eta^{\omega_3} A_0^{\omega_1} \left(A_0^{\omega_2}\right)^* \left(e^{i(\kappa_{\omega_1}+\kappa_{\omega_2}+\Delta k)z} - e^{i(-\kappa_{\omega_1}+\kappa_{\omega_2}+\Delta k)z} - e^{i(\kappa_{\omega_1}-\kappa_{\omega_2}+\Delta k)z} + e^{i(-\kappa_{\omega_1}-\kappa_{\omega_2}+\Delta k)z} \right) \end{cases} \tag{6.12}$$

We obtain the following possible resonance conditions from the above equations:

$$\pm\kappa_{\omega_1} \pm \kappa_{\omega_2} + \Delta k = \pm\kappa_{\omega_3} \text{ or } \pm\kappa_{\omega_1} \pm \kappa_{\omega_2} + \Delta k = \mp\kappa_{\omega_3}$$
$$\text{or } \pm\kappa_{\omega_1} \mp \kappa_{\omega_2} + \Delta k = \pm\kappa_{\omega_3} \text{ or } \pm\kappa_{\omega_1} \mp \kappa_{\omega_2} + \Delta k = \mp\kappa_{\omega_3} \quad (6.13)$$

The above three examples have illustrated how the resonance conditions can be obtained analytically. It is to be noted that all the above resonance conditions are derived for lossless waveguides. In practice, a lossless waveguide certainly does not exist. However, similar to SHG, so long as the loss coefficient is small compared with the phase mismatch the resonance conditions will not be greatly affected, but the optimal interaction length must be carefully designed.

6.4 Conclusions

In this chapter, we present the coupled equations and resonance conditions for other frequency conversion effects, including third-harmonic generation, sum-frequency and difference-frequency generation. The coupled equations can be easily obtained in the non-depletion regions. The resonance conditions can be obtained by the driven harmonic oscillator model. Basically, the resonance conditions usually include the addition and subtraction of the coupling coefficients for all waves and the phase mismatch.

References

[1] R. W. Boyd, *Nonlinear optics*, (Academic Press Inc., 2003).

[2] A. Yariv, *Optical Electronics in Modern Communications*, (Oxford University Press, 1997).

[3] D. Marcuse, *Theory of dielectric optical waveguides*, (Academic Press, 1991).

CHAPTER 7 OBSERVATION OF CONTINUOUS-WAVE SECOND-HARMONIC GENERATION IN SEMICONDUCTOR WAVEGUIDE DIRECTIONAL COUPLERS

In this chapter, we report the first experimental observation of continuous-wave second-harmonic generation in waveguide directional couplers. We employ a GaAs/AlGaAs system and observe four resonance peaks in a ~15nm spectral range, with a maximal conversion efficiency of $1.6\%W^{-1}cm^{-2}$. This observation verifies the theory proposed in Chapter 5 and Chapter 6. This new configuration has the potential to open a new range of applications for nonlinear frequency conversion.

7.1 Introduction

The theory of second harmonic generation and other frequency conversion effects in waveguide directional couplers has been investigated in Chapter 5 and 6. In this chapter, we experimentally demonstrate this phenomenon in a GaAs/AlGaAs material system. The GaAs/AlGaAs has attracted much attention as a nonlinear material in recent years due to its large nonlinear constants, mature epitaxial fabrication process, and ease of incorporation into diode lasers. The demonstrated structure opens the way to realize semiconductor laser sources by incorporating the directional couplers with diode lasers. Such devices can find applications in spectroscopic systems, telecommunication networks, and quantum computation.

The nonlinear susceptibility of GaAs is about 180pm/V which is about three times higher than that in $LiNbO_3$ [1][2]. However, the III-V semiconductors have a cubic structure and there is no intrinsic birefringence that can be used for phase-matching. Several methods have been used to cancel the effects of material dispersion, which include artificial birefringence technique [3][4], quasi-phase matching technique [5]-[9], and modal matching technique [10][11] in waveguides. The artificial birefringence of multilayer composites of GaAs and oxidized AlAs can be achieved through the selective

oxidation of AlAs in GaAs/AlAs multilayers [3][4]. Quasi-phase matched stacks of discrete plates at the Brewster angle have been used to generate a second-harmonic wave [5], which, however, suffers from high scattering loss at the interfaces between air and semiconductors. Diffusion bonded stacked GaAs for quasi-phase-matched second-harmonic generation has been demonstrated in Ref. [6]. Furthermore, quasi-phase-matched AlGaAs waveguides with periodic crystal domain inversion can be achieved by use of wafer bonding through atomic rearrangement and organometallic chemical vapor deposition growth [7][8]. Modal-phase-matched GaAs/AlGaAs waveguides for second-harmonic generation have also been reported in Refs. [10][11]. The interest in this class of materials comes from potential applications in various functional devices, especially integrated devices for second-harmonic generation, difference frequency generation, and all-semiconductor optical parametric oscillators. Since compact and efficient laser sources are sparse in the mid-IR, these materials are much attractive with a broad range of mid-IR transparency and the possibility of integration with semiconductor laser sources in a monolithic ensemble. These devices can be used as widely as in optical communication, all-optical signal processing, and quantum communication. However, the quasi-phase matched GaAs/AlGaAs devices still suffer from complicated fabrication processes and the modal-phase matched waveguides do not generate efficient frequency conversion due to the small field overlap between pump modes and second-harmonic modes.

On the other side, $Al_xGa_{1-x}As$ alloys give rise to refractive index differences as large as 0.5 in the near-IR depending on the Al concentration. Furthermore, the thickness of $Al_xGa_{1-x}As$ can be controlled precisely by epitaxial growth technique, for example, less than 50nm with a 5% variation layer is possible. Hence, it is feasible to design a vertical directional coupler by using GaAs/AlGaAs systems. Furthermore, mature epitaxial growth techniques result in very small waveguide losses by reducing the scattering loss at the interfaces between different layers. Other distinct advantages of GaAs over existing materials include room-temperature operation, mature growth and fabrication technology and the potential for mass production and low cost. With all these advantages, we thus expect that GaAs materials are the best candidate for the proposed theory.

7.2 Wafer design and simulation

In order to experimentally verify the theory in chapter 5 and 6 we implemented a directional coupler as an epitaxially grown dual-core ridge waveguide on <1, 0, 0> GaAs substrates. The designed epitaxial structure is 1500nm $Al_{0.9}Ga_{0.1}As$ / 140nm $Al_{0.3}Ga_{0.7}As$ / 300nm $Al_{0.5}Ga_{0.5}As$ / 140nm $Al_{0.3}Ga_{0.7}As$ / 500nm $Al_{0.9}Ga_{0.1}As$ / 140nm $Al_{0.3}Ga_{0.7}As$ / 300nm $Al_{0.5}Ga_{0.5}As$ / 140nm $Al_{0.3}Ga_{0.7}As$ / 1500nm $Al_{0.9}Ga_{0.1}As$. The $Al_{0.9}Ga_{0.1}As$ layers serve as cladding and as the separating layer between the two waveguides. The $Al_{0.3}Ga_{0.7}As/Al_{0.5}Ga_{0.5}As/Al_{0.3}Ga_{0.7}As$ combination acts as the guiding layer and this is a type of "M" waveguide designed for optimizing the field overlap between TE_2 mode at the second-harmonic frequency and TE_0 and TM_0 modes at the fundamental frequencies [12][13]. Typical refractive index distributions and intensities for these modes are plotted in Fig. 7.1.

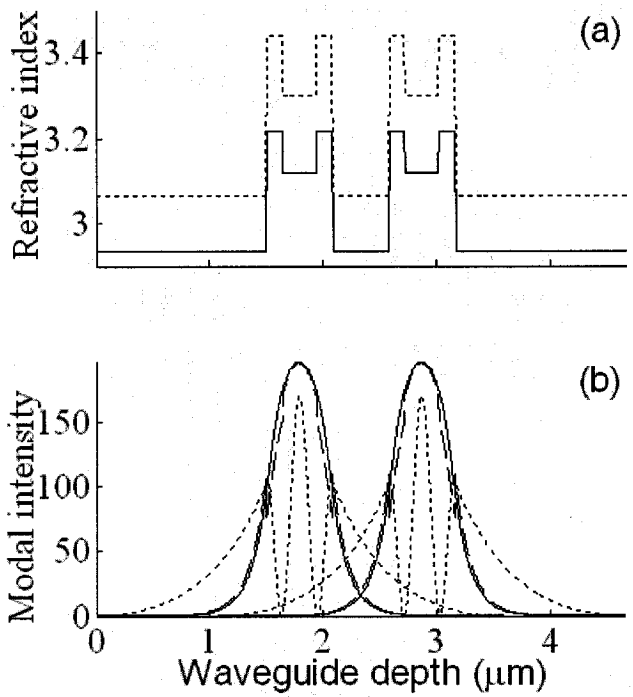

Figure 7.1. (a) Refractive index distribution at 1.55μm (solid line) and 0.775μm (dotted line). (b) Intensity distribution $|E|^2$ of modes TE_0 (solid line) and TM_0 (dashed line) at 1.55μm, and TE_2 at 0.775μm (dotted line).

Using $A_{\omega_j}(z)$ and $B_{\omega_j}(z)$ to present the slowly varying amplitudes in waveguides 1 and 2, respectively, similar to the coupled wave equations Eq. (6.6), we obtain

$$\frac{dA_{2\omega}^{TE_2}}{dz} = -i\kappa_{2\omega}^{TE_2} B_{2\omega}^{TE_2} - i\eta A_{\omega}^{TE_0} A_{\omega}^{TM_0} \exp(i\Delta kz)$$
$$\frac{dB_{2\omega}^{TE_2}}{dz} = -i\kappa_{2\omega}^{TE_2} A_{2\omega}^{TE_2} - i\eta B_{\omega}^{TE_0} B_{\omega}^{TM_0} \exp(i\Delta kz) \quad (7.1)$$

Here, $\kappa_{2\omega}^{TE_2}$ is the mode-coupling coefficient of the directional coupler for the second harmonic, η includes the product of the nonlinear optical coefficient and the overlap integral of the fundamental and the second harmonic waves, and $\Delta k = k_{2\omega}^{TE_2} - k_{\omega}^{TE_0} - k_{2\omega}^{TM_0}$ is the phase mismatch (k is the wave number). The mode-coupling coefficients indicate how rapidly the power in the first waveguide is transferred to the second waveguide. The first terms in the right-hand sides of the above equations describe the coupling effect of the directional coupler and the second terms in the right-hand sides result from the nonlinear effects. Under the non-depletion assumption which implies that the presence of the second harmonic does not influence the motion of the fundamental wave, the amplitudes for the fundamental wave oscillate between the two waveguides:

$$\begin{aligned} A_{\omega}^{TE_0} &= c_1 \exp\left(i\kappa_{\omega}^{TE_0}\right) + c_2 \exp\left(i\kappa_{\omega}^{TE_0}\right) \\ B_{\omega}^{TE_0} &= -c_1 \exp\left(i\kappa_{\omega}^{TE_0}\right) + c_2 \exp\left(i\kappa_{\omega}^{TE_0}\right) \\ A_{\omega}^{TM_0} &= c_1 \exp\left(i\kappa_{\omega}^{TM_0}\right) + c_2 \exp\left(i\kappa_{\omega}^{TM_0}\right) \\ B_{\omega}^{TM_0} &= -c_1 \exp\left(i\kappa_{\omega}^{TM_0}\right) + c_2 \exp\left(i\kappa_{\omega}^{TM_0}\right) \end{aligned} \quad (7.2)$$

where $\kappa_{\omega}^{TE_0}$ and $\kappa_{\omega}^{TM_0}$ are the coupling coefficients of TE_0 and TM_0 modes at the fundamental frequency, c_1 and c_2 are two constants depending on how much power is coupled into the individual waveguides from free space. In our experiment, we align the input polarization of the fundamental wave 45 degree in respect to the waveguide y-direction, by which the input power is divided equally in TE mode and TM mode. Because the modal fields for TE_0 and TM_0 do not differ very much, it is reasonable to assume that the ratio of TE_0 and TM_0 power coupled into each waveguide is the same. This results in identical constants c_1 and c_2 for TE_0 and TM_0 modes.

Substituting Eq. (7.2) into Eq. (7.1) results in four resonance conditions at which efficient SHG should be observed

$$\pm\left(\kappa_{\omega}^{TE_0}+\kappa_{\omega}^{TM_0}\right)+\Delta k=-\kappa_{2\omega}^{TE_2}$$
$$\pm\left(\kappa_{\omega}^{TE_0}-\kappa_{\omega}^{TM_0}\right)+\Delta k=\kappa_{2\omega}^{TE_2} \quad (7.3)$$

To calculate the resonance wavelengths satisfying the above equations, we used CAMFR software package to simulate the slab waveguide structure. The refractive index of GaAs and $Al_xGa_{1-x}As$ are obtained from Refs. [14]-[16]. As seen from Eq. (7.3), we need to compute the phase mismatch and the coupling coefficients for both the fundamental and SHG waves. The effective index distributions of TE_2 mode at the second-harmonic frequency and TE_0 and TM_0 modes at the fundamental frequencies are shown in Fig. 7.2. It is to be noted that for TE_2 mode, the effective indices in Fig. 7.2 are corresponding to the wavelength half of those indicated by the labels for x-axis. It is seen clearly that there is no phase matching between these three modes in the spectral range from 1.48 to 1.58 μm. In Fig. 7.3, we plot the coupling coefficients for these three modes as a function of fundamental wavelength. The value of the coupling coefficients are appropriately 0.03 μm^{-1} which is sufficient to compensate the phase mismatch. From these data, we found the resonance wavelengths following Eq. (7.3) appear between 1.54 to 1.55 μm.

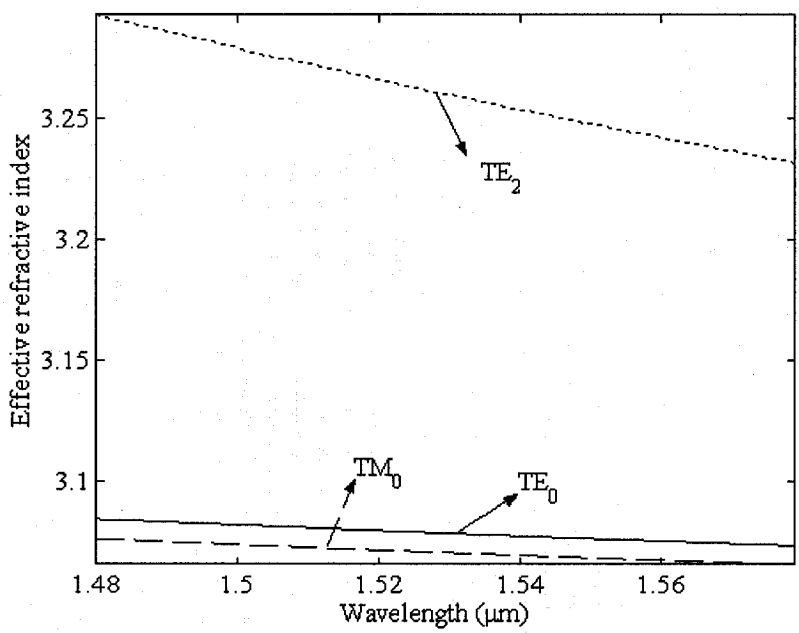

Figure 7.2. The effective indices of TE_0 and TM_0 modes of fundamental wave and TE_2 mode of SHG as a function of wavelength.

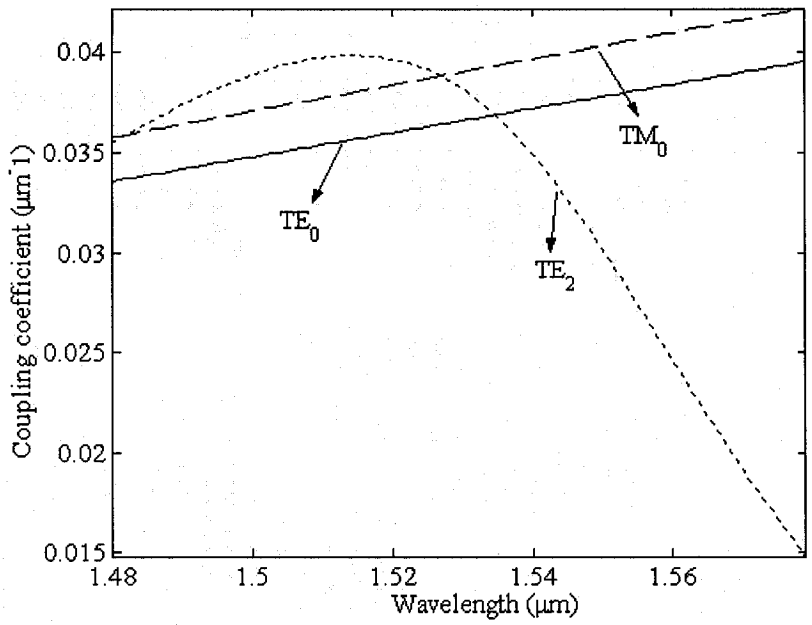

Figure 7.3. The coupling coefficients of TE_0 and TM_0 modes of fundamental wave and TE_2 mode of SHG as a function of wavelength.

7.3 Waveguide fabrication

The wafer has designed to be a vertical directional coupler, however, channel structures must be fabricated to provide the confinement of the light in the horizontal direction. To do so, standard photo-lithography and plasma etching techniques were employed. The main procedures are drawn in Fig. 7.4. The wafer is first coated with a liquid photoresist and is then spun at a typical speed of between 1 and 5 krpm. A post-spin soft bake is used to improve resist uniformity and adhesion (100 degree, several minutes). The wafer with resist film is then put into a mask-aligner. A mask which defines the pattern to be transferred to the wafer is also placed in the mask-aligner. After correct alignment, the wafer is exposed to 436nm (G-line) light. We used a positive resist so that the light passes through the transparent regions of the mask and the illuminated photoresist is removed during the following development stage. The wafer is exposed to a developing solution and after development, the pattern on the mask is transferred to the photoresist layer. The developed wafer proceeds to be hard baked at 120 degree for about half minute in order to further drive off resist solvents and strengthen the resist adhesion.

The next step is dry etch of the wafer which is done in an inductively coupled plasma (ICP) etcher. The ICP allows the user to create high-density plasma by an inductive coin, resulting in increased etch rates and anisotropy. The etch depth is expected to be 5 μm and the etch rate is about 1.5 μm per minute. Since the resist layer works as a mask layer for the etching, one needs to carefully consider etch selectivity between GaAs/AlGaAs and resist, which is about 3:1. The resist thickness therefore is at least 2 μm. By properly controlling the etch time, the expected etch depth can be obtained. After etching, the residual resist is removed by wet etch in aceton solution. The channel waveguides have been fabricated after the above procedures. As we have discussed, high-concentration of $Al_{0.9}Ga_{0.1}As$ is used as the cladding layers, and it has high oxidation rate after exposure in the air. This oxidation may induce stress beneath the directional coupler and the channel structures may separate from the substrate. Therefore, a cap layer must be deposited after etching to protect the waveguide from the air. In our experiment, a 200nm silicon oxide layer is deposited by chemical vapor deposition technique after dry etching. The SEM pictures before and after the etching are presented in Figs. 7.5 and 7.6, respectively. The white-grey areas represent core regions and the dark-grey areas represent cladding regions. It is clear that two core layers are present and the thickness of these layers corresponds to what we designed.

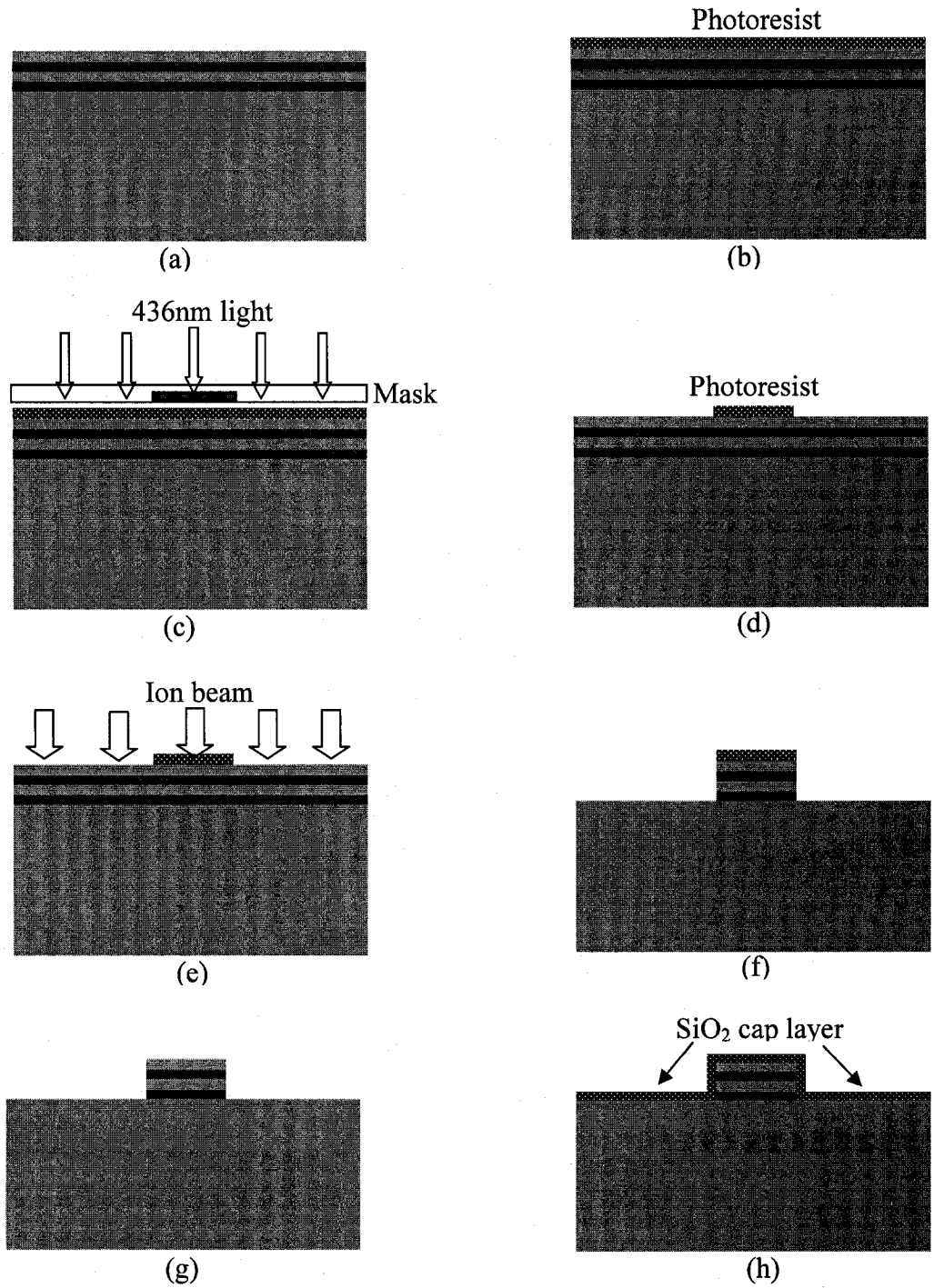

Figure 7.4. (a) The GaAs/AlGaAs wafer. (b) Photoresist is coated on the wafer. (c) The resist is exposed to blue light through a mask. (d) After development, the pattern on the mask is transferred to the resist. (d) ICP etch of the wafer. (f) The pattern is transferred to GaAs/AlGaAs layers. (g) Removal of residual resist. (h) Deposition of SiO_2 cap layer by PECVD.

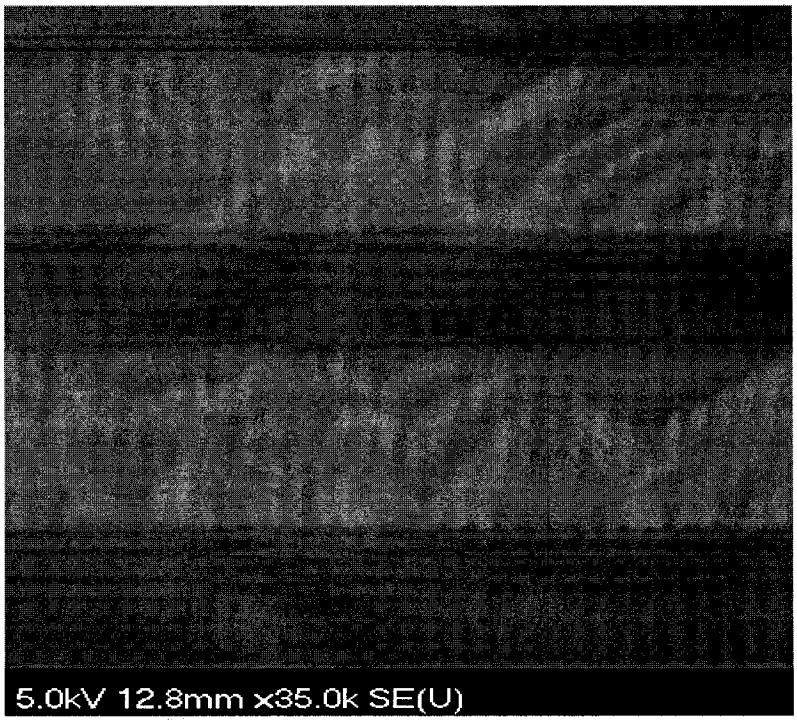

Figure 7.5. SEM picture of the cross-section of epitiaxial wafer used in our experiment.

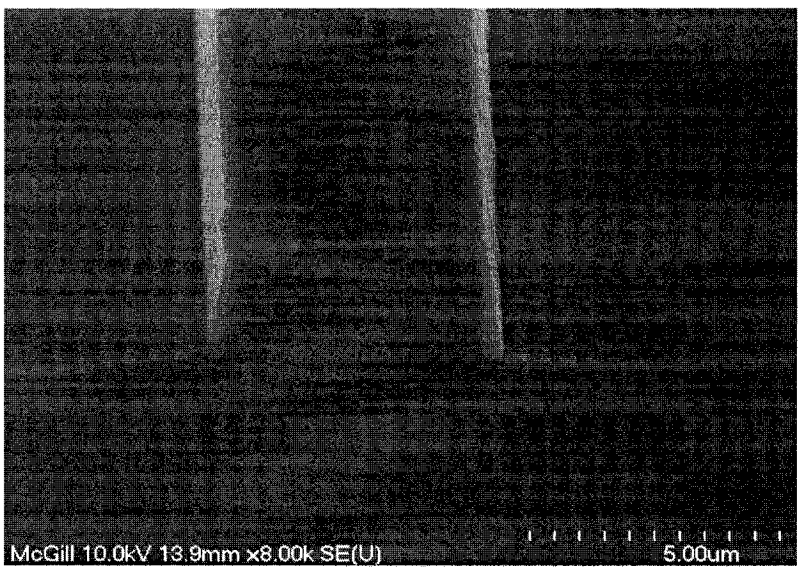

Figure 7.6. SEM picture of the fabricated channel waveguide directional coupler.

7.4 Optical setup

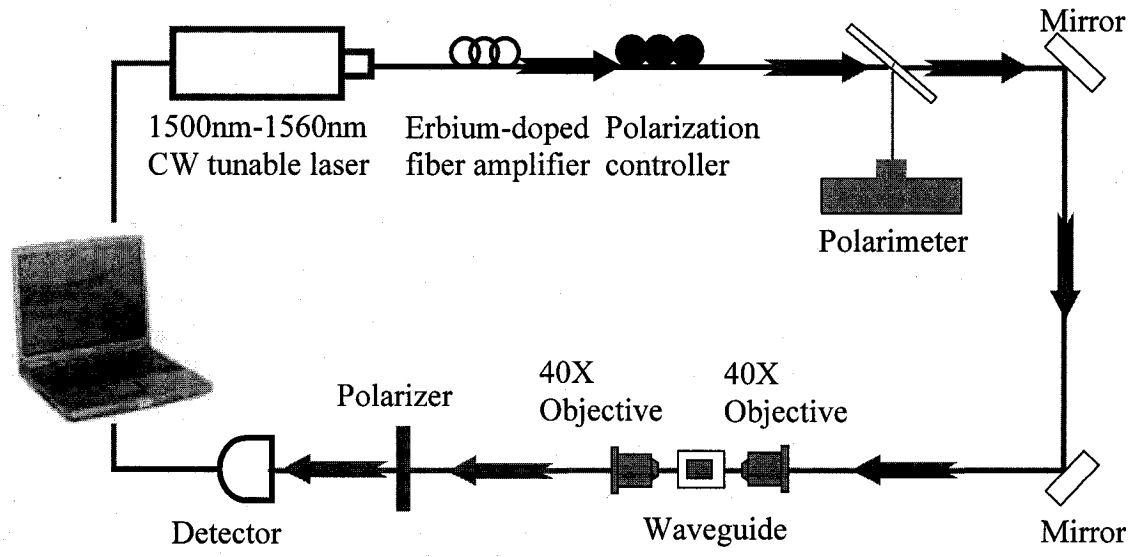

Figure 7.7. Diagram of optical setup to test waveguide loss and SHG.

The above diagram shows the optical setup used in our experiment. A continuous-wave tunable semiconductor laser amplified by an erbium-doped fiber amplifier (EDFA), is coupled into the waveguide via a 40X objective lens. A second 40X objective was used to collect the transmitted fundamental wave and the SHG signal. The polarization controller is used to control the polarization direction of the fundamental wave and the polarimeter inspects the polarization status. The polarizer after the collective objective is used to detect the polarization of the SHG signal. Two different detectors are used: a silicon detector for measuring the SHG signal and a GaAs/InGaAs detector for detecting the transmitted fundamental wave. The wavelength and the power of the input laser are remotely controlled by a Labview computer program and the detected power value is also collected by the Labview program.

7.5 Measurement of waveguide propagation loss

In the experimental implementation, ridge structures, oriented along the <0, 1, 1> direction and of width 5 μm, were dry etched in order to provide two-dimensional confinement. The tested directional coupler has a length of 4 mm. Since the optical power

oscillates in between two guiding layers and it is difficult to precisely measure the waveguide loss. However, with the Fabry-Perot technique described below [17], we approximately obtained the loss figure as ~1.24cm^{-1} for TE input and ~2.71 cm^{-1} for TM input, both at a 1550nm wavelength. We were unable to measure the waveguide loss of the TE_2 mode at the second-harmonic frequency.

7.5.1 Fabry-Perot technique to measure waveguide propagation loss

The propagation loss of waveguide structures is due to material properties and fabrication imperfection. It is an intrinsic property of the waveguides. There are three main experimental techniques to measure waveguide loss: (1) the cut-back method; (2) the scattered light measurement; and (3) the Fabry-Perot resonance methods [17]. The cut-back method measures the output power from a waveguide for different waveguide lengths. As the output power exponentially depends on the waveguide length, one can deduce the propagation loss with the measurement. The scattered light method measures the scattered light from the surface of a waveguide as a function of waveguide length. Since the amount of the light scattered from a waveguide is proportional to the light in the waveguide, the rate of decay of scattered light will give the rate of decay of the light in the waveguide. The propagation loss can then be calculated in a similar way to the cut-back method. In this section we will focus on the Fabry-Perot resonance method since we have used this method to measure the loss in our waveguide directional couplers.

If a waveguide has two polished facets, it becomes a cavity structure similar to the cavity of a laser since reflection occurs at both facets. For semiconductor waveguide structures, the reflection between air (n=1) and semiconductor core ($n \approx 3$) is about 25%, and therefore a strong cavity can be formed. This is the so called Fabry-Perot cavity. Consider a standard FP cavity with two surfaces as shown in Fig. 7.8, an incident electrical field E_i is transmitted to the cavity region with a value $t_1 E_i$ and propagates to the second surface with a value $t_1 E_i e^{-ik'L}$. At surface 2, part of the electrical field will be transmitted to free space and part will be reflected back to surface 1. Therefore, multiple reflections occur as the light passes along the waveguide and back.

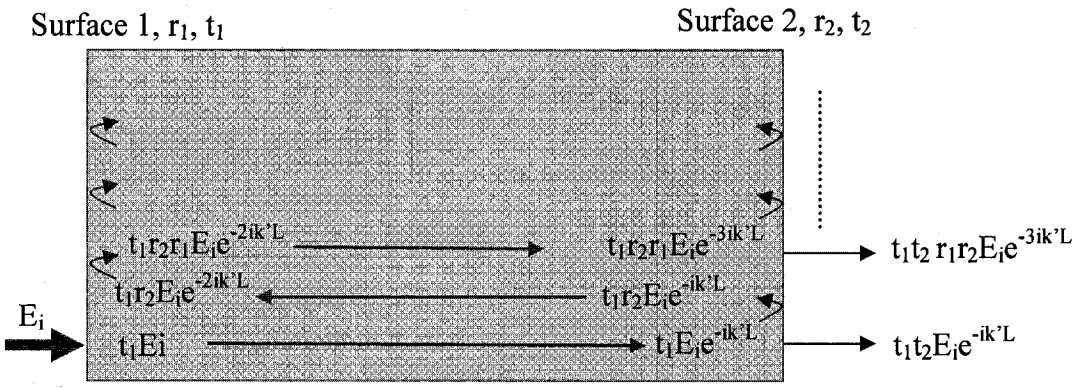

Figure 7.8. Transmission through Fabry-Perot cavity. Here, k'=k-iα/2, with k is the wave number in the waveguide, and α is the power loss. r_i and t_i are the reflection and transmission coefficient at the ith surface, respectively.

The total transmission is therefore

$$\begin{aligned} E_t &= t_1t_2E_ie^{-ik'L} + t_1t_2E_ie^{-ik'L}r_1r_2e^{-2ik'L} + t_1t_2E_ie^{-ik'L}(r_1r_2e^{-2ik'L})^2 + \cdots \\ &= t_1t_2E_ie^{-ik'L}(1 + r_1r_2e^{-2ik'L} + (r_1r_2e^{-2ik'L})^2 + \cdots) = \frac{t_1t_2E_ie^{-ik'L}}{1 - r_1r_2e^{-2ik'L}} \end{aligned} \tag{7.4}$$

The total transmitted power is

$$I_t / I_0 = \frac{(1-R)^2 e^{-\alpha L}}{\left(1 - Re^{-\alpha L}\right)^2 + 4Re^{-\alpha L}\sin^2(kL)} \tag{7.5}$$

By measuring the maximal transmitted power ($\sin^2(kL) = 0$ in the above equation) and the minimal transmitted power ($\sin^2(kL) = 1$ in the above equation), the waveguide loss can be calculated by

$$\alpha = -\frac{1}{L}\ln\left(\frac{1}{R}\frac{\sqrt{\zeta}-1}{\sqrt{\zeta}+1}\right) \tag{7.6}$$

where R is the facet reflectivity and ζ is the ratio of the maximum intensity to minimum intensity [17]. The modulation of the total transmission power can be realized by tuning the wavelength or the temperature.

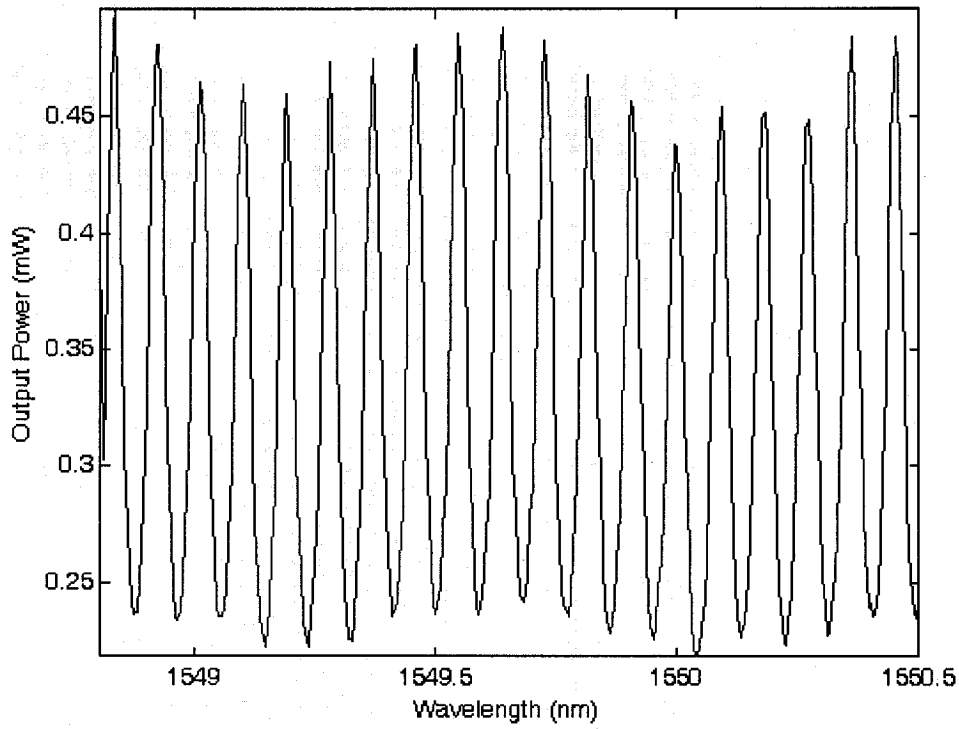

(a)

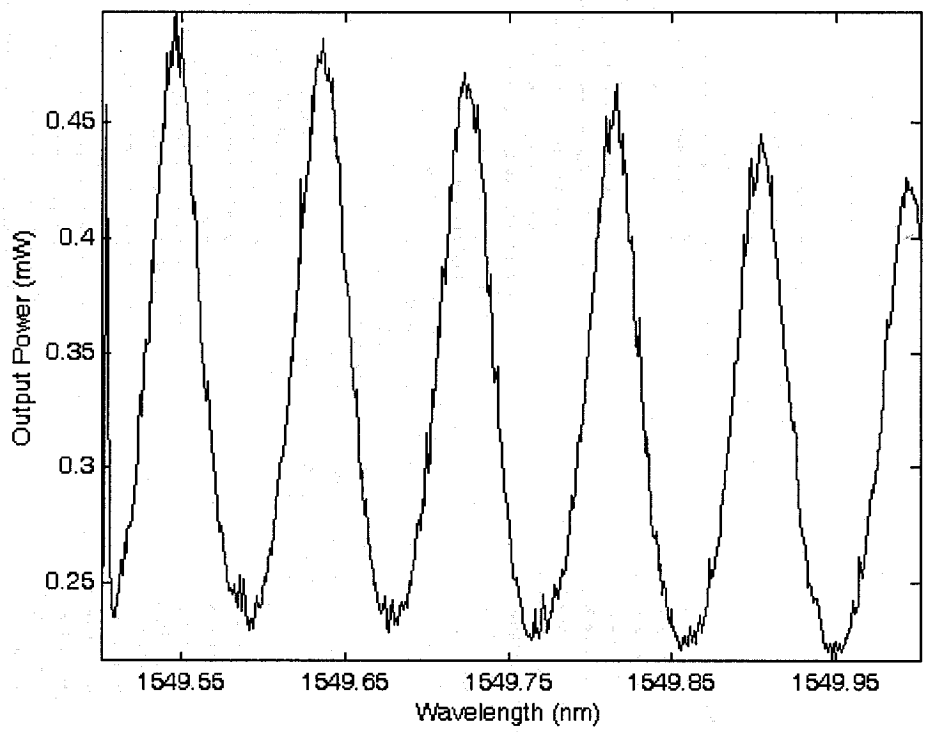

(b)

Figure 7.9. Fabry-Perot scan of the fabricated directional coupler for TE input.

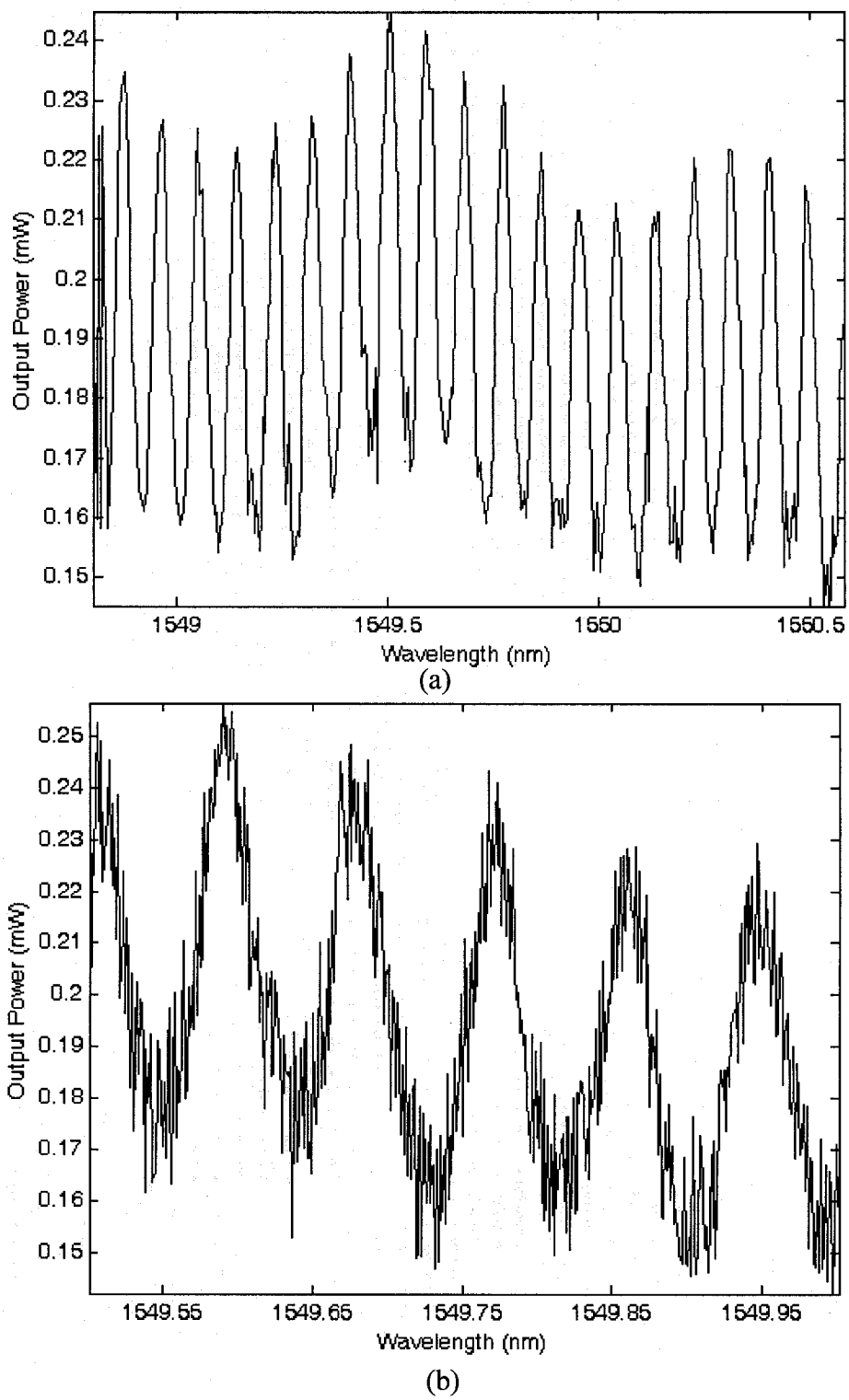

Figure 7.10. Fabry-Perot scan of the fabricated directional coupler for TM input.

7.5.2 Measurement of waveguide propagation loss in GaAs/AlGaAs directional coupler

Since the optical power oscillates in between two guiding layers and it is difficult to precisely measure the waveguide loss. However, with the Fabry-Perot technique, we measured the total transmission power as a function of wavelength and the Fabry-Perot resonance were found for both TE and TM input, as shown in Fig. 7.9 and Fig. 7.10. In this experiment, we used a distributed Bragg laser (GN Nettest, DFB 1550.12) without EDFA. The spectral FWHM of this laser is expected to be less than 0.001nm. The power meter used in this experiment is Newport 1830 with an InGaAs detector. The wavelength scanning step for these figures is 0.005nm. From these data, ζ which is the ratio of the maximum intensity to minimum intensity is calculated to be ~1.95 and ~1.40 for TE and TM input, respectively. The reflectivity at the both faucets is ~0.25. By using Eq. (7.6), we approximately obtained the loss figure as ~1.24cm^{-1} for TE input and ~2.71 cm^{-1} for TM input, both at a 1550nm wavelength. We were unable to measure the waveguide loss of the TE_2 mode at the second-harmonic frequency since it is difficult to excite high-order mode.

7.6 Measurement of second harmonic generation

For the harmonic generation measurement, a continuous-wave laser, tunable from 1.5 to 1.6 μm and then amplified by an erbium-doped fiber amplifier, was coupled into the waveguide via a 40X objective lens. The input has a spectral FWHM of ~0.1nm, measured by a spectrum analyzer. A typical set of spectra is shown in Fig. 7.11, which explicitly demonstrates four SHG peaks in the spectral range from 1.565 to 1.580 μm. The resonance take place at, 1.5668, 1.5686, 1.5730 and 1.5790 μm, and the FWHM spectral widths are ~0.4, ~0.45, ~1.1, and ~1.1nm, respectively. The SHG polarization was measured by a standard polarizer. The dependence of SHG power on the input polarizations was carefully inspected and we concluded that all the four resonance correspond to TE + TM input and TE output. The appearance of four resonance peaks uniquely verifies the theory proposed in chapter 5. The spectral widths of the signal are consistent with those reported in similar structures, but for single waveguides [10][11]. However, it is difficult to precisely predict, from simulation, the exact peak locations

because of the lack of the knowledge of the exact refractive index distribution and feature sizes. For example, using a two-dimensional simulation of the directional coupler, the expected resonance peaks should appear between 1.54 to 1.55 μm, which are about 20 nm away from the experimental results (this deviation between experiment and design exists in similar GaAs/AlGaAs structures [10] and other waveguide systems [18]). Nevertheless, we expect that the first to the fourth peaks may correspond to resonance conditions $-\left(\kappa_{\omega}^{TE_0}+\kappa_{\omega}^{TM_0}\right)+\Delta k=-\kappa_{2\omega}^{TE_2}$, $\left(\kappa_{\omega}^{TE_0}-\kappa_{\omega}^{TM_0}\right)+\Delta k=\kappa_{2\omega}^{TE_2}$, $-\left(\kappa_{\omega}^{TE_0}-\kappa_{\omega}^{TM_0}\right)+\Delta k=\kappa_{2\omega}^{TE_2}$, and $\left(\kappa_{\omega}^{TE_0}+\kappa_{\omega}^{TM_0}\right)+\Delta k=-\kappa_{2\omega}^{TE_2}$, respectively. At the first resonance, for example, the coupling coefficients are calculated as ~0.04 μm^{-1} for TE_0 and TM_0 pump and ~0.02 μm^{-1} for TE_2 SHG, which imply that the power of the fundamental wave exchanges between the two waveguides about one hundred times. The relative peak values of the four resonances can be changed by modifying the position of input beam, as shown in Fig. 7.11, where the three curves were obtained with different locations of input beam. This is because that varying the input position actually modifies the value of c_1 and c_2 in Eq. (7.2). By optimizing the 1573nm resonance, we achieved a maximum measured SHG power of 50nW with a 90mW input power. The SHG power as a function of input power was then measured and plotted in Fig. 7.12. The fitting to the slope results in a value of 2.0 on a log-log plot. This confirms the quadratic dependence of the SHG power on the pumping power. By measuring the transmitted power of the fundamental wave, we estimated that the average internal pumping power for the TE and TM is $P_{TE} \approx 5mW$ and $P_{TM} \approx 5mW$. After taking into account the numerical aperture of the collecting lens (0.65) and the facet reflectivity for the second harmonic (0.6), we estimate that only 20% of the generated SHG was collected [11][19] . The normalized conversion efficiency is calculated to be $\eta = P_{SHG}/\left(4P_{TE}P_{TM}L^2\right)=\sim 1.6\%\ W^{-1}\ cm^{-2}$. This number is quite low compared with that in similar GaAs/AlGaAs waveguides [11] where $\eta=\sim 30\%W^{-1}cm^{-2}$ has been obtained. Several factors may explain the low SHG power obtained. The coupling efficiency to the directional coupler is only ~10% because of the loss from the input objective, the input facet reflectivity and the mode-matching factor. Furthermore, the loss of the TE_2 mode at the second harmonic frequency is expected to be very high, which limits the effective conversion length. Another reason is that the pump

power is distributed into the two waveguides, which actually reduce the effective power in each individual waveguide. Further optimization, therefore, can include improving the coupling efficiency, reducing the leaky loss of SHG mode, optimizing the modal overlap between the fundamental wave and SHG, and choosing an appropriate interaction length. Nevertheless, there is no fundamental limit for the total conversion efficiency as studied in Chapter 5 if the waveguides are lossless.

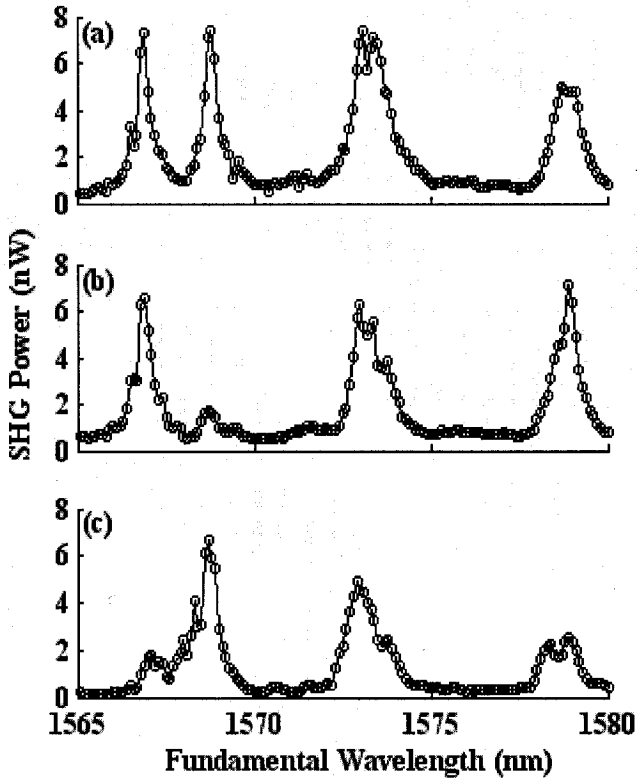

Figure 7.11. Typical SHG power as a function of the fundamental wavelength. Three curves were obtained by varying the position of input beam. It is evident that four resonance peaks are found, and the relative peak ratio at resonance can be alternated by the change of input location.

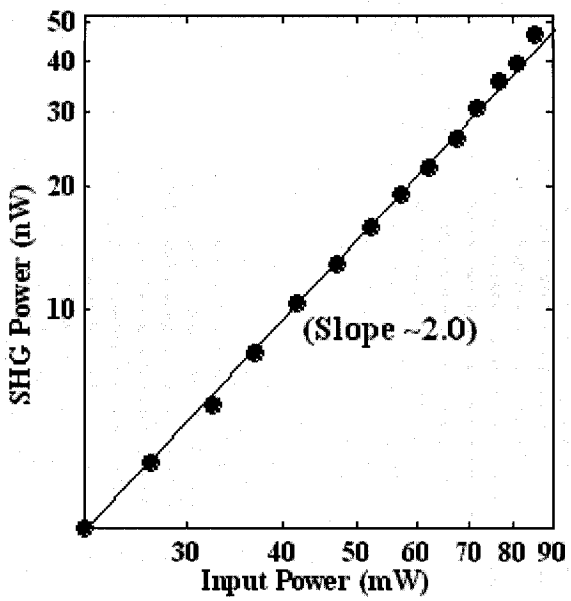

Figure 7.12. Log-log plot of the second-harmonic output power as a function of the input fundamental power. The best fit gives a slope ~2.0 which verifies the quadratic dependence of the SHG on the pumping power.

The GaAs/AlGaAs directional coupler that we have demonstrated here has application not only for the SHG process, but also for difference-frequency generation. By incorporating directional couplers in/out of the cavity of quantum-well lasers, tunable compact sources which emit the light at around 750nm can be produced. These mid-infrared compact sources are desirable for pollutant detect in the molecular fingerprint region or for process monitoring. Based on the unique properties of multi-resonance within a small spectral range, multiple wavelength outputs can be generated by a pulsed pump, which may be useful in optical metrology. Furthermore, the directional coupler is intrinsically a two-port device which may be suited to construct two-photon optical parametric down-conversion. Such devices can generate entangled pairs of photons which can find applications in quantum optics experiments, from quantum cryptography and teleportation to the Bell experiment [20][21]. However, the proposed configuration has potential for application in any suitable material system and is not restricted to

GaAs/AlGaAs. Directional couplers have very modest fabrication requirements when compared to quasi-phase matching techniques and potentially open the way to a much broader application of nonlinear optical processes across a much wider range of wavelengths.

7.7 Conclusions

In summary, we have experimentally demonstrated continuous-wave SHG in Ga/AlGaAs directional couplers. To our knowledge, this is the first proof of the proposed theory in Chapter 5 and 6 which employs directional couplers to generate frequency conversion. We show that four resonance peaks appear in a 15nm spectral range and η=~1.6%$W^{-1}cm^{-2}$ is obtained experimentally. This phenomenon has not been shown in bulk materials or single waveguides. Compared with the efficiency obtained in similar GaAs/AlGaAs waveguides (η=~30%$W^{-1}cm^{-2}$), the efficiency we obtained in directional couplers are still very low. However, as we mentioned in the previous section, we can improve this efficiency by reducing waveguide losses, especially for the second-harmonic mode, and increasing the overlap between the modes of fundamental wave and second-harmonic wave.

References

[1] B. F. Levine and C. G. Bethea, "Nonlinear susceptibility of gap-relative measurement and use of measured values to determine a better absolute value," *Appl. Phy. Lett.*, vol. 20, pp. 272-275, 1972.

[2] S. Adachi, "GaAs, AlAs, and $Al_xGa_{1-x}As$: Material parameters for use in research and device applications," J. Appl. Phys., vol. 58, pp. R1-R29, 1985.

[3] A. Fiore, V. Berger, E. Rosencher, P. Bravetti, and J. Nagle, "Phase matching using an isotropic nonlinear optical material," *Nature*, vol. 391, pp. 463-465, 1998.

[4] K. Moutzouris, S. Venugopal Rao, M. Ebrahimzadeh, A. De Rossi, V. Berger, M. Calligaro, and V. Ortiz, "Efficient second-harmonic generation in birefringently phase-matched GaAs/Al_2O_3 waveguides," *Opt. Lett.*, vol. 26, pp. 1785-1787, (2001).

[5] D. E. Thompson, J. D. McMullen, and D. B. Anderson, "2nd-harmonic generation in GaAs stack of plates using high-power CO_2-laser radiation," *Appl. Phys. Lett.*, vol. 29, pp. 113-115, 1976.

[6] J. Gordon, G. L. Woods, R. C. Echardt, R. R. Route, R. S. Feigelson, M. M. Fejer and R. L. Byer, "Diffusion-bonded stacked GaAs for quasi-phase-matched second-harmonic generation of a carbon dioxide laser," *Electron. Lett.*, vol. 29, pp. 1942-1944, 1993.

[7] S. J. B. Yoo, R. Bhat. C. Caneau. and M. A. Koza, "Quasi-phase-matched second-harmonic generation in AlGaAs waveguides with periodic domain inversion achieved by wafer-bonding," *Appl. Phys. Lett.*, vol. 66, pp. 3410-3412, 1995.

[8] S. J. B. Yoo, *et al.* "Wavelength conversion by difference frequency generation in AlGaAs waveguides with periodic domain inversion achieved by wafer bonding," *Appl. Phys. Lett.*, vol. 68, pp. 2609-2611, 1996.

[9] T. Skauli, "Measurement of the nonlinear coefficient of orientation-patterned GaAs and demonstration of highly efficient second-harmonic generation," *Opt. Lett.*, vol. 27, pp. 628-630, 2002.

[10] S. Ducci, *et al.* "Second-harmonic generation through optimized modal phase matching in semiconductor waveguides," *Appl. Phys. Lett.*, vol. 83, pp. 620-622, 2003.

[11] S. Ducci, *et al.* "Continuous-wave second harmonic generation in modal phase matched semiconductor waveguides," *Appl. Phys. Lett.*, vol. 84, pp. 2974-2976, 2004.

[12] A. Chowdhury, and L. McCaughan, "Continuously phase-matched M-waveguides for second-order nonlinear upconversion," *IEEE Photonics Technol. Lett.*, vol. 12, pp. 486-488, 2000.

[13] B. Oster and H. Fouchhardt, "Variations of optical M-waveguides for direct phase matching in AlGaAs," *IEEE Photonics Technol. Lett.*, vol. 13, pp. 672-674, 2001.

[14] D. E. Aspnes, S. M. Kelso, R. A. Logan, and R. Bhat, "Optical properties of $Al_xGa_{1-x}As$," *J. Appl. Phys.*, vol. 60, pp. 754-767, 1986.

[15] O. J. Glembocki and K. Takarabe, "Aluminum Gallium Arsenide ($Al_xGa_{1-x}As$)," in *Handbook of optical constants of solids II*, pp. 513-557, 1991.

[16] S. Gehrsitz, F. K. Reinhart and C. Gourgon, N. Herres, A. Vonlanthen and H. Sigg, "The refractive index of Al_{x}Ga_{1-x}As below the band gap: Accurate determination

and empirical modeling," *Journal of Applied Physics*, vol. 87, no. 11, pp. 7825-7837, 2000.

[17] G. T. Reed, and A. P. Knights, *Silicon photonics*, (John Wiley & Sons Inc., 2004).

[18] G. L. J. A. Rikken, C. J. E. Seppen, E. G. J. Staring, and A. H. J. Venhuizen, "Efficient modal dispersion phase-matched frequency doubling in poled polymer waveguides," *Appl. Phys. Lett.*, vol. 62, pp. 2483-2486, 1993.

[19] C. M. Herzinger, C. C. Lu, T. A. DeTemple, and W. C. Chew, 'The semiconductor waveguide facet reflectivity problem," *IEEE J. Quantum Electron.*, vol. 29, pp. 2273-227, 1993.

[20] A. K. Ekert, J. G. Rarity, P. R. Tapster, and G. M. Palma, "Practical quantum cryptography based on 2-photon interferometry," *Phys. Rev. Lett.*, vol. 69, pp. 1293-1296, 1992.

[21] D. Bouwmeester, *et al.* "Experimental quantum teleportation," *Nature*, vol. 390, pp. 575-579, 1997.

CHAPTER 8 CONCLUSIONS

8.1 Summary of this thesis

In principle, there are several ways to couple two waveguides together, including directional couplers, grating-assisted directional couplers, double-grating couplers, and tapered waveguide couplers. The applications of such coupled waveguides can be found in many areas such as optical communication, planar-waveguide or integrated optics and nonlinear optics. Directional couplers have been intensively investigated in integrated optics and there are various active and passive photonic components based on them. Nevertheless, the separation between the two waveguides in a directional coupler must be close enough to realize field overlap between the guided modes of these two waveguides. For some applications such as optical integration this is a dramatic limitation. One question arises immediately: is it possible to couple two parallel waveguides far away from each other so that there is no field overlap between the guided modes of these waveguides. The answer is apparently yes, as illustrated by the double-grating coupler investigated in this thesis. This double-grating coupler is analogous to the transmitter and receiver antennas in microwave or RF communications, whereas one grating acts as an out-coupler similar to a transmitter antenna and the other acts as an in-coupler similar to a receiver antenna. One important advantage is found: since the light is transported through radiation modes, there is no requirement of field overlap between guided modes and therefore the separation between two waveguides can be large. One big disadvantage is also quickly found: since the light propagates somewhere in the form of radiation modes, the coupling efficiency is low due to the radiation loss and diffractive loss. The advantage is quite useful to construct multi-layer vertically integrated photonic circuits, where the double-grating couplers can serve as the same roles as the vias in the ultra-large electrical multi-layer circuits. It is thus expected that such double-grating couplers can find important applications in optical integration. In the first part of this thesis, we investigate a double-grating coupler using deep grating structures between two SOI waveguides. The use of deep and strong grating structures makes the coupler very compact, suited for dense integration of optical circuits. This is another very important advantage which

solves one of the main challenges in high-density photonic integrated circuits. Nevertheless, the maximal coupling efficiency is less than 30% by using binary gratings. This low efficiency is understandable since (1) radiation modes cannot be converted into guided modes with 100% efficiency, and (2) large diffractive spreading loss occurs due to deep grating structures. We employ binary gratings since these gratings can be fabricated by standard etching processes. If more complex fabrication is ready on hand, one can increase the coupling efficiency by using blazed gratings. The efficiency can be as high as 40% by a simple design. By incorporating Bragg reflectors under or along the waveguide cores, the efficiency can be further increased. However, these certainly increase the design complexity and fabrication complexity. In my personal view, the best method must be also the simplest method. Vertical directional couplers and taper structures appear simpler structures than grating structures. Since adiabatic conversion between guided modes is realized by these two methods, the coupling efficiency can be much higher. However, these two methods are not robust to realize real multi-layer integrated circuits. Therefore, none of the above methods including the double-grating coupler seems perfect for future optical integration purpose. One may have to choose different methods depend on, such as, efficiency, alignment and bandwidth requirements. Based on the study in Chapter 4, the following conclusions can be drawn:

- Double-grating couplers can be used in the future multi-layer photonic integrated circuits. Since the space between the two coupled waveguides does not need to be very short, this kind of coupler may realize robust planar and multi-layer photonic circuits.
- Deep and strong gratings are suited to realize very compact vertical waveguide couplers. Compactness is very important for high-dense integration of photonic components.
- The eigenmode expansion method is suited to design and optimize binary double-grating couplers. This method is a strict electromagnetic method and therefore is able to include the complex interaction between two gratings. Separating two gratings into independent our-coupler and in-coupler is not accurate enough and will lose

some insights, such as Fabry-Perot resonance found in Chapter 4. Meanwhile, the computation time is shorter than the finite-difference time-domain method.

- We can obtain a 29% coupling efficiency between two SOI waveguides by using simple binary grating structures. This efficiency can be further improved by using blazed gratings and Bragg reflectors.

Directional couplers are very important photonic components in many optical waveguide devices. They are very simple structures consisting of two close and parallel waveguides. The light can be coupled back and forward between these two waveguides. In the second part of this thesis, we investigate a new possible application of directional couplers in nonlinear frequency conversion. The coupled mode theory is applied to describe nonlinear frequency conversion in directional couplers. Since the optical power oscillates between two parallel waveguides as a function of distance, by considering the amplitude of the second-harmonic signal in the coupled waveguides as an oscillator and the nonlinear polarization as an external harmonic force, a resonance condition can be found which results in efficient power transfer from pump to signal. Furthermore, the resonance effect can also be understood by phase-matching between the supermodes of directional couplers. Some conclusions are drawn from the study of this subject in this thesis:

- Directional couplers can act as a useful platform to generate nonlinear frequency conversion.
- If the coupled mode theory is applied to such phenomenon, a resonance effect can be found due to the resonance between the phase mismatch and the coupling coefficients of directional couplers.
- If we regard directional couplers as multi-mode compound waveguide structures, the resonance phenomenon can be explained by phase matching between the supermodes of directional couplers.
- Besides the theoretical significance, the most important advantages of using directional couplers over single waveguides are twofold: (1) the possibility to increase the field overlap between the pump wave(s) and the generated wave which results in

higher conversion efficiency; (2) the possibility to generate multi-wavelength by a single pump wave.

- GaAs/AlGaAs materials are suited to construct nonlinear directional couplers to generate frequency conversion due to their large nonlinear constants and mature fabrication processes.
- Due to mature epitaxial techniques, vertical directional couplers using GaAs/AlGaAs are easier to fabricate than horizontal directional couplers, since the distance between two waveguides are controlled by epitaxial technique rather than following micro-fabrication processes. The fabrication of channel directional couplers can be done by standard photo-lithography and dry etching techniques. Since the width for such channel directional couplers are about several microns, the fabrication tolerance is relaxed very much.
- Second harmonic generation can be obtained by using continuous-wave pump in GaAs/AlGaAs directional couplers. Both the wavelengths of the second harmonic and pump must be located in the transparency window of GaAs/AlGaAs materials. The demonstrated conversion efficiency in our experiment is η=~1.6%$W^{-1}cm^{-2}$. Higher efficiency can be obtained by optimizing the length of directional couplers, increasing the field overlap between pump and second-harmonic waves, and reducing the waveguide losses.
- Four resonance peaks have been found in a ~15nm spectral range in GaAs/AlGaAs directional couplers. If we use a pump laser with the spectral width larger than 15nm, four wavelength output of second harmonic can be simultaneously obtained.

8.2 Future research directions

Following the theoretical study of double-grating couplers in this thesis, there are some important issues needed to be addressed. One of the most important issues is how to efficiently improve the coupling efficiency. At least 50% coupling efficiency is desired for the applications in real devices. Certainly, the trade-off between efficiency and design and fabrication complexity must be considered. In this thesis, the coupling between two SOI waveguides is investigated due to the importance of SOI waveguides and the

possibility of experimental demonstration of the designed double-grating coupler. However, applying such couplers to other types of waveguides, such as GaAs/InGaAs waveguides, silica waveguides, and polymer waveguides, are particularly important to exploit the potential of such vertical couplers. As an application example, the coupling from single-mode fibers to rectangular waveguides in semiconductor lasers has been the subject of investigation for many years [1]-[3]. This can be done by using an intermediate waveguide (for example, silica or polymer waveguides) whose dimensions and refractive indices closely match the single-mode fibers [1]. The task then is to efficiently couple the light between the intermediate waveguides with semiconductor laser waveguides. The double-grating couplers have the potential to fulfill this purpose, but careful theoretical study must be done for such coupling between two very dissimilar waveguides. Furthermore, the coupling between an SOI small-size waveguide and a fiber-matched silica or polymer waveguide is another important subject [4]-[7]. Since SOI waveguides and III-V waveguides in semiconductor lasers have close indices, $n \approx 3.5$, the above two coupling problems are very similar. Applying double-grating couplers to such applications rather than future multi-layer photonic integrated circuits will be a more direct demonstration of their potential.

In this thesis, only the theoretical study of the double-grating couplers is presented, and more attention should be paid to the experimental investigation. While the standard lithography and plasma etching techniques can be used to fabricate binary gratings, wafer bonding techniques must be used to bond two waveguides with gratings together. An accurate alignment with the alignment tolerance within a few microns between two stacked grating couplers has to be achieved to maximize the coupling. Since SOI wafers are not transparent at visible light, it is hard to do so by using a traditional alignment instrument with visible-light microscopy. However, the alignment may be done by making some marks on the edge of the alignment area at the bottom substrates. Secondly, it is hard to practically control the accuracy of the thickness of the separation layer which is very demanding on the design, as shown in Chapter 4. The separation layer can be formed by filling the bonding epoxy into the gap between two SOI wafers which is defined by micro spacer. However, it may be difficult to inject the epoxy into the grating grooves which are only a few hundred nanometers wide. It is also possible to form

separation layer by depositing photo resist and using direct bonding technique. The thickness of spun photo resist can be controlled to the accuracy of a hundred nanometers. Furthermore, this kind of coupler is not restricted to SOI waveguides, but can be used to other high-index-contract waveguides, for example, SiN waveguides. The applications in other type of waveguides may dramatically reduce the difficulties involving in the bonding process. Even so, the theoretical study shows that the applications on passive components may be limited by the strict alignment tolerance and the accuracy of the thickness of the separation layer. However, important active photonic components based on such double-grating couplers may be very attractive, for example, if the separation layer is controlled externally, an on-off switch can be made in a straight way. In summary, more experimental work should be done to explore the full potential of such double-grating couplers.

A complete coupled-mode theory of second-harmonic generation and other nonlinear frequency conversion effects in directional couplers have been investigated in Chapter 5 and 6. We also experimentally demonstrated second-harmonic generation in GaAs/AlGaAs directional coupler structures in Chapter 7. Nevertheless, the obtained conversion efficiency is still very low for practical applications. More investigation should be done to demonstrate that more efficient frequency conversion may be possible to be generated in directional couplers than in single waveguides, by increasing the field overlap between second-harmonic modes and pump modes. Further experiments should be done for other frequency conversion effects, such as third-harmonic generation, sum and difference-frequency generation and four-wave mixing. The effects of fabrication variation and tolerance on the frequency generation should be also characterized. Other materials such as nonlinear polymers and $LiNbO_3$ can be also utilized to realize frequency conversion in directional couplers. In addition, possible applications in optical metrology and optical signal processing by frequency conversion in directional couplers should also be investigated. In a summary, we have only presented a basic theory and a primary experiment of proof of concept for nonlinear frequency conversion in directional couplers, more investigation can be carried out following this direction to fully understand the advantages and limitations of frequency conversion in directional couplers.

References

[1] J. M. Hammer, R. A. Bartolini, A. Miller, and C. C. Neil, "Optical grating coupling between low-index film and waveguides," *Appl. Phys. Lett.*, vol. 28, pp. 192-194, Feb. 1976.

[2] N. H. Sun, J. K. Butler, J. P. Sih, G. A. Evans, and L. Pang, in *Proc. Conf. lasers Electro-Opt.* Anaheim, CA, June 2-7, 1996, pp. 217-218.

[3] B. H. V. Borges, and P. R. Herczfeld, "Coupled-mode analysis of highly asymmetric directional couplers with periodic perturbation," *IEEE Tran. Microwave Theo. and Tech.*, vol. 46, pp. 215-226, Mar. 1998.

[4] R. M. Emmons, and D. G. Hall, "Buried-oxide silicon-on-insulator structures: waveguide grating couplers", *IEEE J. Quantum Electron.*, vol. 28, pp. 164-175, Jan. 1992.

[5] D. Taillaert, W. Bogaerts, P. Bienstman, T. F. Krauss, P. V. Daele, I. Moerman, S. V.erstuyft, K. D. Mesel and R. Baets, "An out-of-plane grating coupler for efficient butt-coupling between compact planar waveguides and single-mode fibers," *IEEE J. Quantum Electron.*, vol. 38, pp. 949-955, July 2002.

[6] D. Taillaert, W. Bogaerts, and R. Baets, "Efficient coupling between submicron SOI-waveguides and single-mode fibers", in *Proc. Symp. IEEE/LEOS*, Benelux Chapter, 2003, pp. 289-292.

[7] G. Z. Masanovic, V. M. N. Passaro, G. T. Reed, "Dual grating-assisted directional coupling between fibers and thin semiconductor waveguides", *IEEE Photon. Technol. Lett.*, vol. 15, pp. 1395-1397, Oct. 2003.

Appendix A

In this appendix, we present the detailed derivation for the coupled equations in Eqs. (5.2) from the wave equation. The method followed is the same as that reported in Ref. [1]. Here, we consider only a 2-D directional coupler, however, the extension to a 3-D directional coupler can be made without any difficulties. This is true because once we obtain the coupled equations for the 2-D directional coupler, they can be applicable to the 3-D directional coupler, except that the coupling coefficients and the field overlap parameters must be recalculated for the 3-D structure. Assuming that the nonlinear effect and the coupling between two waveguides do not affect significantly the waveguide modes, and all the interacting modes are TE modes, the mode fields can be expressed by $\vec{E}_i^{\omega_j} = \vec{e}_y F_i^{\omega_j}(x)\exp(-i\beta_i^{\omega_j} z + i\omega_j t)$, where $\beta_i^{\omega_j}$ is the corresponding propagation constant and the subscript i=1, 2 represents the ith waveguide and j=1, 2 denotes the fundamental wave and the harmonic generation respectively. The transverse mode-field profile $F_i^{\omega_j}(x)$ satisfies:

$$\left(\frac{\partial^2}{\partial x^2} - \beta_i^{\omega_j}\right) F_i^{\omega_j} + \omega_j^2 \mu \varepsilon_i^j(x) F_i^{\omega_j} = 0 \tag{A1}$$

where $\varepsilon_i^j(x) = \varepsilon_0 \left(n_i^j(x)\right)^2$ is the dielectric distribution for the ith waveguide.

The total electric field of the coupled waveguides can be expressed as the sum of the eigenmodes in each waveguide:

$$\vec{E} = \frac{1}{2}\left(A_\omega(z)\vec{E}_1^{\omega} + A_{2\omega}(z)\vec{E}_1^{2\omega} + B_\omega(z)\vec{E}_2^{\omega} + B_{2\omega}(z)\vec{E}_2^{2\omega}\right) + c.c \tag{A2}$$

where $A_{\omega_j}(z)$ and $B_{\omega_j}(z)$ are the slowly varying amplitudes in waveguide 1 and waveguide 2, respectively. Here, we have ignored the possibility of coupling to the continuum of radiation modes. The wave equation obeyed by the electric field is [2]:

$$\nabla^2 \vec{E} = \mu\varepsilon \frac{\partial^2 \vec{E}}{\partial t^2} + \mu \frac{\partial^2}{\partial t^2}\left[\vec{P}_{NL}\right] \tag{A3}$$

Here $\vec{P}_{NL}$ is the nonlinear polarization resulting from nonlinear optical susceptibilities.

Substitution of Eq. (A2) into (A3) leads to:

$$e^{i\omega t}\left[\frac{A_\omega}{2}\left(-\left(\beta_1^\omega\right)^2 F_1^\omega+\frac{\partial^2 F_1^\omega}{\partial x^2}+\omega^2\mu\varepsilon_1^\omega(x)F_1^\omega\right)e^{-i\beta_1^\omega z}+\frac{1}{2}\left(-2i\beta_1^\omega\frac{dA_\omega}{dz}+\frac{d^2A_\omega}{dz^2}\right)F_1^\omega e^{-i\beta_1^\omega z}\right]$$
$$+e^{i\omega t}\left[\frac{B_\omega}{2}\left(-\left(\beta_2^\omega\right)^2 F_2^\omega+\frac{\partial^2 F_2^\omega}{\partial x^2}+\omega^2\mu\varepsilon_2^\omega(x)F_2^\omega\right)e^{-i\beta_2^\omega z}+\frac{1}{2}\left(-2i\beta_2^\omega\frac{dB_\omega}{dz}+\frac{d^2B_\omega}{dz^2}\right)F_2^\omega e^{-i\beta_2^\omega z}\right]$$
$$+\text{c.c.}=\mu\frac{\partial^2}{\partial t^2}\left[\vec{P}_{\text{pert}}^{\,\omega}+\vec{P}_{\text{NL}}^{\,\omega}\right]_y \tag{A4}$$

for the fundamental wave and

$$e^{i2\omega t}\left[\frac{A_{2\omega}}{2}\left(-\left(\beta_1^{2\omega}\right)^2 F_1^{2\omega}+\frac{\partial^2 F_1^{2\omega}}{\partial x^2}+(2\omega)^2\mu\varepsilon_1^{2\omega}(x)F_1^{2\omega}\right)e^{-i\beta_1^{2\omega}z}\right.$$
$$\left.+\frac{1}{2}\left(-2i\beta_1^{2\omega}\frac{dA_{2\omega}}{dz}+\frac{d^2A_{2\omega}}{dz^2}\right)F_1^{2\omega}e^{-i\beta_1^{2\omega}z}\right]$$
$$+e^{i2\omega t}\left[\frac{B_{2\omega}}{2}\left(-\left(\beta_2^{2\omega}\right)^2 F_2^{2\omega}+\frac{\partial^2 F_2^{2\omega}}{\partial x^2}+(2\omega)^2\mu\varepsilon_2^{2\omega}(x)F_2^{2\omega}\right)e^{-i\beta_2^{2\omega}z}\right. \tag{A5}$$
$$\left.+\frac{1}{2}\left(-2i\beta_2^{2\omega}\frac{dB_{2\omega}}{dz}+\frac{d^2B_{2\omega}}{dz^2}\right)F_2^{2\omega}e^{-i\beta_2^{2\omega}z}\right]$$
$$+\text{c.c.}=\mu\frac{\partial^2}{\partial t^2}\left[\vec{P}_{\text{pert}}^{\,2\omega}+\vec{P}_{\text{NL}}^{\,2\omega}\right]_y$$

for the harmonic wave. Here $\vec{P}_{\text{pert}}^{\,\omega_j}$ accounts for the deviation of the medium polarization from that which accompanies the unperturbed modes. $\vec{P}_{\text{pert}}^{\,\omega_j}$ results from the fact that in the left-hand sides of Eqs. (A4) and (A5), $\varepsilon^{\omega_j}(x)$ has been replaced by $\varepsilon_1^{\omega_j}(x)$ or $\varepsilon_2^{\omega_j}(x)$. We note that from Eq. (A1), the sums of the first three terms in the left-hand sides of Eqs. (A4) and (A5) are zero. Furthermore, we have the following slowly-varying-amplitude approximation [3]:

$$\left|\frac{d^2A_{\omega_j}}{dz^2}\right|<<\beta_1^{\omega_j}\left|\frac{dA_{\omega_j}}{dz}\right|,\quad\left|\frac{d^2B_{\omega_j}}{dz^2}\right|<<\beta_2^{\omega_j}\left|\frac{dB_{\omega_j}}{dz}\right| \tag{A6}$$

and from Eq. (A4) and (A5), we obtain

$$\left[\left(-i\beta_1^{\omega_j}\frac{dA_{\omega_j}}{dz}\right)F_1^{\omega_j}e^{i\omega_j t-i\beta_1^{\omega_j}z}+\left(-i\beta_2^{\omega_j}\frac{dB_{\omega_j}}{dz}\right)F_2^{\omega_j}e^{i\omega_j t-i\beta_2^{\omega_j}z}\right]+c.c.$$
$$=\mu\frac{\partial^2}{\partial t^2}\left[\vec{P}_{pert}^{\omega_j}+\vec{P}_{NL}^{\omega_j}\right]_y \tag{A7}$$

The perturbation polarization responsible for the coupling between the two waveguides is calculated by

$$\left[\vec{P}_{pert}\right]_y^{\omega}=$$
$$e^{i\omega t}\left[\varepsilon_0\frac{1}{2}\left[F_1^{\omega}A_{\omega}\left(\left(n^{\omega}\right)^2-\left(n_1^{\omega}\right)^2\right)e^{-i\beta_1^{\omega}z}\right]+\varepsilon_0\frac{1}{2}\left[F_2^{\omega}B_{\omega}\left(\left(n^{\omega}\right)^2-\left(n_2^{\omega}\right)^2\right)e^{-i\beta_2^{\omega}z}\right]\right]+c.c. \tag{A8}$$

and

$$\left[\vec{P}_{pert}\right]_y^{2\omega}=$$
$$e^{i2\omega t}\left[\varepsilon_0\frac{1}{2}\left[F_1^{2\omega}A_{2\omega}\left(\left(n^{2\omega}\right)^2-\left(n_1^{2\omega}\right)^2\right)e^{-i\beta_1^{2\omega}z}\right]+\varepsilon_0\frac{1}{2}\left[F_2^{2\omega}B_{2\omega}\left(\left(n^{2\omega}\right)^2-\left(n_2^{2\omega}\right)^2\right)e^{-i\beta_2^{2\omega}z}\right]\right]+c.c. \tag{A9}$$

The nonlinear polarization takes the form

$$\left[\vec{P}_{NL}\right]_y^{\omega}=$$
$$\left[d(x)A_{2\omega}A_{\omega}^{*}F_1^{2\omega}\left(F_1^{\omega}\right)^{*}e^{i\omega t-i\left(\beta_1^{2\omega}-\beta_1^{\omega}\right)z}+d(x)B_{2\omega}B_{\omega}^{*}F_2^{2\omega}\left(F_2^{\omega}\right)^{*}e^{i\omega t-i\left(\beta_2^{2\omega}-\beta_2^{\omega}\right)z}\right]+c.c. \tag{A10}$$

and

$$\left[\vec{P}_{NL}\right]_y^{2\omega}=\left[\frac{1}{2}d(x)A_{\omega}A_{\omega}F_1^{\omega}F_1^{\omega}e^{i2\omega t-i2\beta_1^{\omega}z}+\frac{1}{2}d(x)B_{\omega}B_{\omega}F_2^{\omega}F_2^{\omega}e^{i2\omega t-i2\beta_2^{\omega}z}\right]+c.c. \tag{A11}$$

Here, $d(x)$ is the element of the nonlinear optical tensor which is corresponding to the case that both the input and SHG output are TE modes. Since different materials are used in the waveguide cladding and core layers, the nonlinear coefficient is a function of x. It is to be noted that in (A10) and (A11), we ignore the cross terms such as $A_{2\omega}B_{\omega}^{*}$ for the nonlinear polarization. These terms could be negligible because the overlap of the modes in different waveguides for different wavelengths is small.

Substitution of Eqs. (A8-A11) into Eq. (A7) results in two equations:

$$\left(-i\beta_1^{\omega}\frac{dA_{\omega}}{dz}\right)F_1^{\omega}e^{-i\beta_1^{\omega}z}+\left(-i\beta_2^{\omega}\frac{dB_{\omega}}{dz}\right)F_2^{\omega}e^{-i\beta_2^{\omega}z}$$
$$=-\omega^2\varepsilon_0\mu\frac{1}{2}\left[F_1^{\omega}A_{\omega}\left(\left(n^{\omega}\right)^2-\left(n_1^{\omega}\right)^2\right)e^{-i\beta_1^{\omega}z}\right]-\omega^2\varepsilon_0\mu\frac{1}{2}\left[F_2^{\omega}B_{\omega}\left(\left(n^{\omega}\right)^2-\left(n_2^{\omega}\right)^2\right)e^{-i\beta_2^{\omega}z}\right]$$
$$-\omega^2\mu d(x)A_{2\omega}A_{\omega}^{*}F_1^{2\omega}\left(F_1^{\omega}\right)^{*}e^{-i\left(\beta_1^{2\omega}-\beta_1^{\omega}\right)z}-\omega^2\mu d(x)B_{2\omega}B_{\omega}^{*}F_2^{2\omega}\left(F_2^{\omega}\right)^{*}e^{-i\left(\beta_2^{2\omega}-\beta_2^{\omega}\right)z} \tag{A12}$$

and

$$\left(-i\beta_1^{2\omega}\frac{dA_{2\omega}}{dz}\right)F_1^{2\omega}e^{-i\beta_1^{2\omega}z}+\left(-i\beta_2^{2\omega}\frac{dB_{2\omega}}{dz}\right)F_2^{2\omega}e^{-i\beta_2^{2\omega}z}$$
$$=-4\omega^2\varepsilon_0\mu\frac{1}{2}\left[F_1^{2\omega}A_{2\omega}\left(\left(n^{2\omega}\right)^2-\left(n_1^{2\omega}\right)^2\right)e^{-i\beta_1^{2\omega}z}\right]$$
$$-4\omega^2\varepsilon_0\mu\frac{1}{2}\left[F_2^{2\omega}B_{2\omega}\left(\left(n^{2\omega}\right)^2-\left(n_2^{2\omega}\right)^2\right)e^{-i\beta_2^{2\omega}z}\right] \tag{A13}$$
$$-2\omega^2\mu d(x)A_{\omega}A_{\omega}F_1^{\omega}F_1^{\omega}e^{-i2\beta_1^{\omega}z}-2\omega^2\mu d(x)B_{\omega}B_{\omega}F_2^{\omega}F_2^{\omega}e^{-i2\beta_2^{\omega}z}$$

Now, we take the product of Eq. (A12) with $\left(F_1^{\omega}\right)^{*}$ and integrate from $-\infty$ to $+\infty$ [1]. The result is

$$\left(-i\beta_1^{\omega}\frac{dA_{\omega}}{dz}\right)e^{-i\beta_1^{\omega}z}\int_{-\infty}^{\infty}F_1^{\omega}\left(F_1^{\omega}\right)^{*}dx+\left(-i\beta_2^{\omega}\frac{dB_{\omega}}{dz}\right)e^{-i\beta_2^{\omega}z}\int_{-\infty}^{\infty}F_2^{\omega}\left(F_1^{\omega}\right)^{*}dx$$
$$=-\omega^2\varepsilon_0\mu\frac{1}{2}\left[A_{\omega}e^{-i\beta_1^{\omega}z}\int_{-\infty}^{\infty}\left(\left(n^{\omega}\right)^2-\left(n_1^{\omega}\right)^2\right)F_1^{\omega}\left(F_1^{\omega}\right)^{*}dx\right]$$
$$-\omega^2\varepsilon_0\mu\frac{1}{2}\left[B_{\omega}e^{-i\beta_2^{\omega}z}\int_{-\infty}^{\infty}\left(\left(n^{\omega}\right)^2-\left(n_2^{\omega}\right)^2\right)F_2^{\omega}\left(F_1^{\omega}\right)^{*}dx\right] \tag{A14}$$
$$-\omega^2\mu A_{2\omega}A_{\omega}^{*}e^{-i\left(\beta_1^{2\omega}-\beta_1^{\omega}\right)z}\int_{-\infty}^{\infty}d(x)F_1^{2\omega}\left(F_1^{\omega}\right)^{*}\left(F_1^{\omega}\right)^{*}dx$$
$$-\omega^2\mu B_{2\omega}B_{\omega}^{*}e^{-i\left(\beta_2^{2\omega}-\beta_2^{\omega}\right)z}\int_{-\infty}^{\infty}d(x)F_2^{2\omega}\left(F_2^{\omega}\right)^{*}\left(F_1^{\omega}\right)^{*}dx$$

In the above equation, the term $\int_{-\infty}^{\infty}F_2^{\omega}\left(F_1^{\omega}\right)^{*}dx$ describes the butt coupling coefficient between the two waveguides and the term $\int_{-\infty}^{\infty}\left(\left(n^{\omega}\right)^2-\left(n_1^{\omega}\right)^2\right)F_1^{\omega}\left(F_1^{\omega}\right)^{*}dx$ represents a small correction to the propagation constants β_1^{ω} [2]. Both these two terms are neglected

in most of the conventional analysis of directional couplers [3]. Meanwhile, the contribution of the term $\int_{-\infty}^{\infty} d(x) F_2^{2\omega} \left(F_2^{\omega}\right)^* \left(F_1^{\omega}\right)^* dx$ is much smaller than that of the term $\int_{-\infty}^{\infty} d(x) F_1^{2\omega} \left(F_1^{\omega}\right)^* \left(F_1^{\omega}\right)^* dx$ since the former describes the field overlap between three modes at different frequencies in different waveguides. Therefore, this term can also be neglected. Finally, we reach the following equation for A_ω:

$$\frac{dA_\omega}{dz} = -i\kappa_\omega B_\omega \exp(-i\Delta\beta_\omega z) - i\eta_1^\omega A_{2\omega} A_\omega^* \exp(-i\Delta k_1 z) \tag{A15}$$

Here, we have defined the coefficients of κ_ω and η_1^ω as

$$\kappa_\omega = \frac{\omega^2 \mu \varepsilon_0 \left[\int_{-\infty}^{\infty} \left(\left(n^\omega\right)^2 - \left(n_2^\omega\right)^2\right) F_2^\omega \left(F_1^\omega\right)^* dx\right]}{2\beta_1^\omega \int_{-\infty}^{\infty} F_1^\omega \left(F_1^\omega\right)^* dx} \tag{A16}$$

$$\eta_1^\omega = \frac{\omega^2 \mu \int_{-\infty}^{\infty} d(x) F_1^{2\omega} \left(F_1^\omega\right)^* \left(F_1^\omega\right)^* dx}{\beta_1^\omega \int_{-\infty}^{\infty} F_1^\omega \left(F_1^\omega\right)^* dx} \tag{A17}$$

Similarly, by taking the product of Eq. (A12) with $\left(F_2^\omega\right)^*$ and integrating from $-\infty$ to $+\infty$, we can reach another equation for B_ω. Finally, the coupled-amplitude equations governing the motions of the slowly varying amplitudes are found under the slowly-varying-amplitude approximation:

$$\begin{cases} \dfrac{dA_\omega}{dz} = -i\kappa_\omega B_\omega \exp(-i\Delta\beta_\omega z) - i\eta_1^\omega A_{2\omega} A_\omega^* \exp(-i\Delta k_1 z) \\ \dfrac{dB_\omega}{dz} = -i\kappa_\omega A_\omega \exp(i\Delta\beta_\omega z) - i\eta_2^\omega B_{2\omega} B_\omega^* \exp(-i\Delta k_2 z) \\ \dfrac{dA_{2\omega}}{dz} = -i\kappa_{2\omega} B_{2\omega} \exp(-i\Delta\beta_{2\omega} z) - i\eta_1^{2\omega} A_\omega^2 \exp(i\Delta k_1 z) \\ \dfrac{dB_{2\omega}}{dz} = -i\kappa_{2\omega} A_{2\omega} \exp(i\Delta\beta_{2\omega} z) - i\eta_2^{2\omega} B_\omega^2 \exp(i\Delta k_2 z) \end{cases} \tag{A18}$$

Here, κ_ω and $\kappa_{2\omega}$ are the mode-coupling coefficients of the directional coupler for the fundamental and the second harmonic waves, respectively. $\Delta\beta_i$ and Δk_i are the wave phase mismatch defined by the following relationship:

$$\begin{cases} \Delta\beta_{\omega_j} = \beta_2^{\omega_j} - \beta_1^{\omega_j} \\ \Delta k_i = \beta_i^{2\omega} - 2\beta_i^{\omega} \end{cases} \tag{A19}$$

It is clear that $\Delta\beta_{\omega_j}$ denotes the phase mismatch between two guided modes in different waveguides at the same frequency, while Δk_i denotes the phase mismatch between the fundamental and the second harmonic waves in the same waveguide. In Eqs. (A18), $\eta_i^{\omega_j}$ is the overlap integral of the fundamental and the second harmonic waves, which is measured by

$$\begin{cases} \eta_i^{2\omega} = \dfrac{2\omega^2\mu \int_{-\infty}^{\infty} d(x)\left(F_1^{2\omega}\right)^*\left(F_i^{\omega}\right)^2 dx}{\left(\beta_i^{2\omega}\right)\int_{-\infty}^{\infty} F_i^{2\omega}\left(F_i^{2\omega}\right)^* dx} \\ \eta_i^{\omega} = \dfrac{\omega^2\mu \int_{-\infty}^{\infty} d(x) F_i^{2\omega}\left(F_i^{\omega}\right)^*\left(F_i^{\omega}\right)^* dx}{\left(\beta_i^{\omega}\right)\int_{-\infty}^{\infty} F_i^{\omega}\left(F_i^{\omega}\right)^* dx} \end{cases} \tag{A20}$$

The coupling coefficients are:

$$\begin{cases} \kappa_\omega = \dfrac{\omega^2\mu\varepsilon_0\left[\int_{-\infty}^{\infty}\left(\left(n^{\omega}\right)^2 - \left(n_2^{\omega}\right)^2\right)F_2^{\omega}\left(F_1^{\omega}\right)^* dx\right]}{2\left(\beta_1^{\omega}\right)\int_{-\infty}^{\infty} F_1^{\omega}\left(F_1^{\omega}\right)^* dx} \\ \kappa_{2\omega} = \dfrac{(2\omega)^2\mu\varepsilon_0\left[\int_{-\infty}^{\infty}\left(\left(n^{2\omega}\right)^2 - \left(n_2^{2\omega}\right)^2\right)F_2^{2\omega}\left(F_1^{2\omega}\right)^* dx\right]}{2\left(\beta_1^{2\omega}\right)\int_{-\infty}^{\infty} F_1^{2\omega}\left(F_1^{2\omega}\right)^* dx} \end{cases} \tag{A21}$$

Eqs. (A18) holds when the propagation constants of the two waveguides at the same frequency are equal or the two waveguides are sufficiently separated [3]. Furthermore, we have assumed that κ_{ω_j} is real.

References

[1] A. Yariv, "Coupled-mode theory for guided-wave optics," *IEEE J. Quantum Electron.*, vol. 9, pp. 919-933, 1973.

[2] Yariv, *Optical Electronics in Modern Communications*, (Oxford University Press, 1997).

[3] K. Okamoto, *Fundamentals of Optical Waveguide*, (Academic Press, 2000).